DOCTORAL THESIS

UNIVERSITAT POLITÈCNICA DE VALÈNCIA

CFD MODELING OF COMBUSTION AND SOOT PRODUCTION IN DIESEL SPRAYS

PRESENTED BY:
Leonardo Manuel Pachano Prieto

SUPERVISED BY:
José María García Oliver

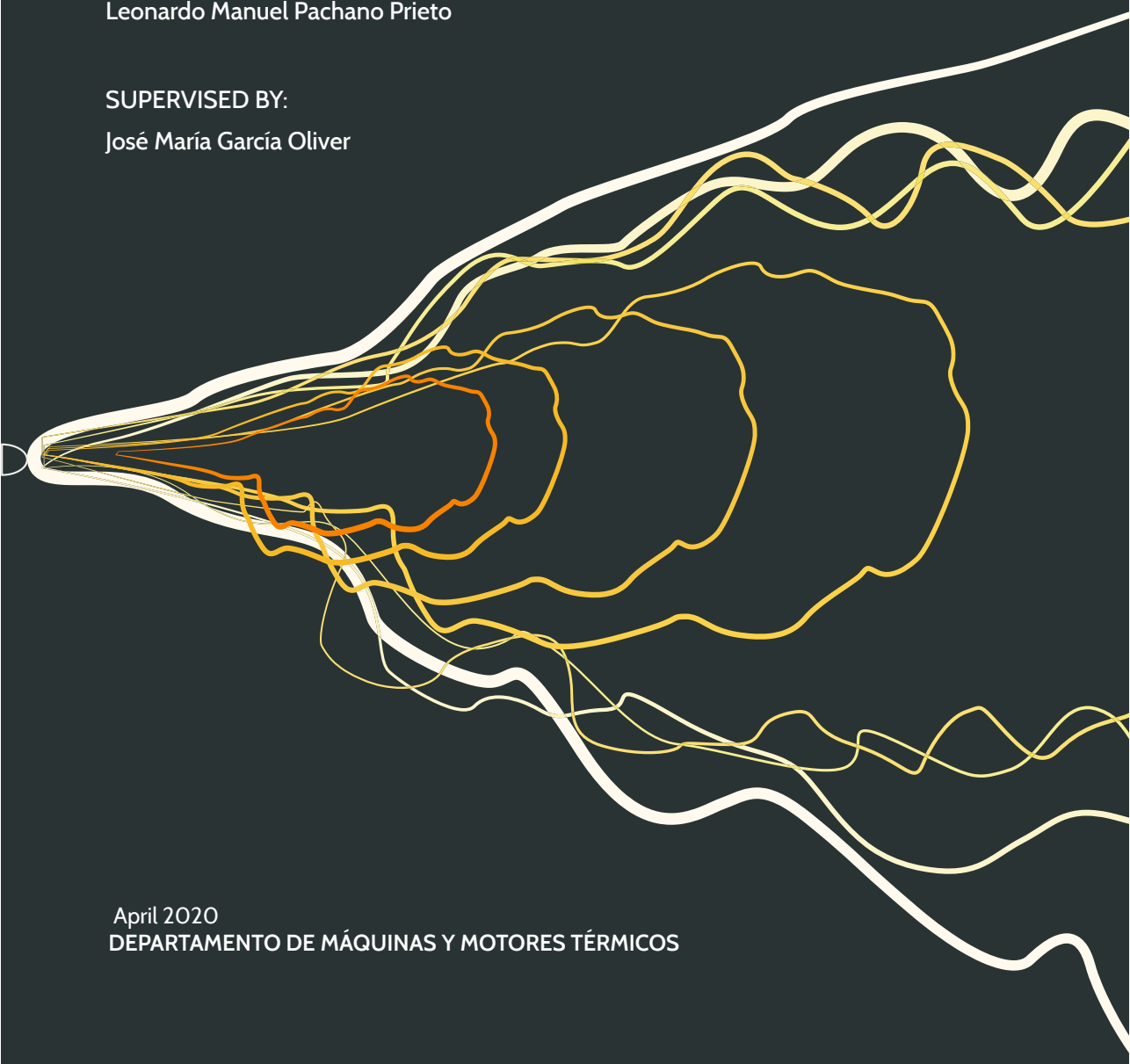

April 2020
DEPARTAMENTO DE MÁQUINAS Y MOTORES TÉRMICOS

UNIVERSITAT POLITÈCNICA DE VALÈNCIA
DEPARTAMENTO DE MÁQUINAS Y MOTORES TÉRMICOS

DOCTORAL THESIS

CFD MODELING OF COMBUSTION AND SOOT PRODUCTION IN DIESEL SPRAYS

PRESENTED BY

D. Leonardo Manuel Pachano Prieto

SUPERVISED BY

Dr. D. José María García Oliver

FOR THE DEGREE OF

Doctor of Philosophy

APRIL 2020

DOCTORAL THESIS

"*CFD modeling of combustion and soot production in Diesel sprays*"

Presented by: D. Leonardo Manuel Pachano Prieto
Supervised by: Dr. D. José María García Oliver

THESIS EXAMINERS

Dr. D. Jacobo Porteiro Fresco
Dr. D. Peter Kelly Senecal
Dr. D. Lambertus Marinus Theodorus Somers

DEFENSE COMMITTEE

Chairman: Dr. D. Raúl Payri Marín
Secretary: Dr. D. Bertrand Naud
Member: Dr. D. Peter Kelly Senecal

Valencia, April 2020

To all who have supported me on this endeavor

Abstract

Over the past few years, soot emissions from internal combustion engines have gained attention due to its impact on the environment and human health. In response, ever-stricter legislation has been enforced driving the research community toward more fuel-efficient and cleaner engines. Within this context, soot modeling has been the subject of many efforts seeking to contribute to the understanding of the highly complex phenomena that composes the soot production process. This thesis main objective aims at simulating soot production in Diesel sprays under engine-like conditions using computational fluid dynamics (CFD).

The fulfillment of the thesis main objective entails a preliminary assessment of the inert spray computational setup for validation purposes. Then, a detailed study on the sub-grid flame structure and handling of turbulence-chemistry interaction is reported focusing on well-mixed and flamelet assumptions. Lastly, the study of reactivity and mixing boundary condition variations on combustion and soot production are assessed with a two-equation soot model.

In summary, throughout this document the reader will find a comprehensive study of combustion and soot modeling in single-hole nozzle sprays in quiescent environments from which the Spray A and Spray D target conditions from the Engine Combustion Network are the main reference cases.

Resum

En els últims anys, les emissions de sutge provinents dels motors de combustió interna han rebut més atenció a causa de l'impacte negatiu que aquestes tenen no sols en l'ambient, sinó també en la salut de l'ésser humà. Com a resposta, lleis cada vegada més estrictes han sigut aplicades impulsant així a la comunitat científica al desenvolupament de motors més eficients en l'ús del combustible i per descomptat més nets en termes d'emissions contaminants. En aquest context, el modelatge computacional ha sigut l'eina utilitzada en nombrosos esforços que busquen contribuir a millorar l'enteniment que es té sobre els altament complexos fenòmens que componen el procés de producció de sutge. El principal objectiu d'aquesta tesi és simular la producció de sutge en rolls dièsel en condicions d'operació típiques d'un motor de combustió interna utilitzant CFD.

La consecució de l'objectiu de la tesi comprèn una avaluació preliminar de la configuració dels diferents models per al cas de rolls inerts. En segon lloc, l'estudi detallat de la hipòtesi utilitzada per a caracteritzar l'estructura de la flama a nivell *sub-grid* (prenent com a base els conceptes *well-mixed* o *flamelet*) i de l'enfocament per a tindre en compte la interacció entre turbulència i química. Finalment, es presenten resultats del modelatge de la combustió i producció de sutge per a diferents condicions de contorn de reactivitat i mescla del doll utilitzant un model de sutge de dues equacions.

En resum, el lector trobarà al llarg d'aquest document un estudi exhaustiu sobre la combustió i producció de sutge en dolls injectats amb toveres monoorifici en ambients immòbils. D'aquesta mena de dolls, l'*Spray A* i *Spray D* de la *Engine Combustion Network* són utilitzats com a casos de referència.

Resumen

En los últimos años, las emisiones de hollín provenientes de los motores de combustión interna han recibido más atención debido al impacto negativo que éstas tienen no solo en el ambiente, sino también en la salud del ser humano. Como respuesta, leyes cada vez más estrictas han sido aplicadas impulsando así a la comunidad científica al desarrollo de motores más eficientes en el uso del combustible y por supuesto más limpios en términos de emisiones contaminantes. En este contexto, el modelado computacional ha sido la herramienta utilizada en numerosos esfuerzos que buscan contribuir a mejorar el entendimiento que se tiene sobre los altamente complejos fenómenos que componen el proceso de producción de hollín. El principal objetivo de esta tesis es simular la producción de hollín en chorros Diesel en condiciones de operación típicas de un motor de combustión interna utilizando CFD.

La consecución del objetivo de la tesis comprende una evaluación preliminar de la configuración de los distintos modelos para el caso de chorros inertes. En segundo lugar, el estudio detallado de la hipótesis utilizada para caracterizar la estructura de la llama a nivel *sub-grid* (tomando como base los conceptos *well-mixed* o *flamelet*) y del enfoque para tener en cuenta la interacción entre turbulencia y química. Por último, se presentan resultados del modelado de la combustión y producción de hollín para diferentes condiciones de contorno de reactividad y mezcla del chorro utilizando un modelo de hollín de dos ecuaciones.

En resumen, el lector encontrará a lo largo de este documento un estudio exhaustivo sobre la combustión y producción de hollín en chorros inyectados con toberas mono-orificio en ambientes quiescentes. De este tipo de chorros, el *Spray A* y *Spray D* de la *Engine Combustion Network* son utilizados como casos de referencia.

Funding and acknowledgments

The respondent wishes to acknowledge the financial support received through *Programa de Ayudas de Investigación y Desarrollo* (PAID-01-16) and *Ayudas para movilidad dentro del Programa para la Formación de Personal investigador 2017* of Universitat Politècnica de València and the Government of Spain through the CHEST Project (TRA2017-89139-C2-1-R).

The respondent also wants to express his gratitude to Convergent Science for their kind support in the use of CONVERGE software for performing the CFD simulations.

Parts of the work presented in this thesis have been supported in a collaborative framework with research partners at Argonne National Laboratory and their support is greatly acknowledged.

Acknowledgements

I would like to thank Dr. Francisco Payri and Dr. José María Desantes for giving me the opportunity to develop the research work that lead to the completion of this thesis at Instituto Universitario de Investigación CMT-Motores Térmicos. I would like to extend my gratitude to faculty, students, technicians and administrative staff who have helped me along the way.

I want to express my most sincere gratitude to my supervisor Dr. José María García. Xemary, in some of the most difficult and challenging times in the completion of this thesis I gained confidence and motivation by looking at your passion for research and your selfless way to teach, both of which I profoundly admire. The early coffee and discussions were always a great way to start the day.

I want to thank Dr. Antonio García and Dr. José Vicente Pastor. Antonio, thank you for your friendship, your guidance and advice beyond the academic field. Xevi, thank you for your trust and support all this time and for reminding me that the ability of abstraction is of much relevance.

For their much valuable suggestions and their willingness to always help me, I owe a especial thanks to Dr. Ricardo Novella and Dr. José Manuel Pastor. Your support was fundamental for my research work.

I greatly appreciate all the support of Dr. Tiemin Xuan and Dr. Noud Maes in the exchange of experimental data for validation.

Back in 2018, I was a visiting student at Argonne National Laboratory. I would like to thank Dr. Sibendu Som for his trust and for giving me the opportunity to work with his team. I profoundly appreciate all the support from Dr. Prithwish Kundu and Dr. Chao Xu. Thank you very much for your time and for the great work.

Four years ago when I moved to Valencia my officemates and friends' support was crucial. I felt more than welcome and it helped me overcome the fear of everything that was new to me at that time. Tiemin Xuan, Mattia Pinotti, Carles Oltra, Carlos Chacón, Vishnu Samala, Varun Nareddy and Wenjun Zhong, thank you.

To my colleagues Felipe De Vargas, Daiana De León and Francisco Tejada I owe a huge thanks for not only contributing academically but for making this journey a fun one.

I am also grateful for the many opportunities at which my next door officemates supported me. Thank you Dr. Eduardo Pérez and Dr. Josep Gómez.

I want to thank my Family. This journey would have not possibly started without them.

Alba García, my fellow student and dear friend since 2009 when we met at the first day of university as undergraduate students. Thank you for accompanying me at each step of the way.

Dr. Mary Vergara, without your confidence in me this journey had not been possible. My interest in research comes from my admiration toward your dedication. Beyond that, I want to express my gratitude for your friendship.

Javier Oviedo, your caring, patience and love are the basis upon which I have stood at countless times along this journey. Unquestionably, it would have not been the same without you by my side to support me, to hear me, to advice me and especially to make my days, day after day, brighter.

"Start now. Start where you are. Start with fear. Start with pain. Start with doubt. Start with hands shaking. Start with voice trembling but start. Start and don't stop. Start where you are, with what you have. Just... start."

Ijeoma Umebinyuo, *Nigeria*

Contents

List of Figures

List of Tables

List of Symbols

Latin

a	Strain rate
A_s	Soot surface area
c	Normalized progress variable
C_χ	Proportionality constant for the mean scalar dissipation rate model
$C_{\varepsilon 1}$, C_μ	Constants in the standard $k-\varepsilon$ turbulence model
C_{min}	Number of carbon atoms in incipient soot nuclei
$c_{p,k}$	Molar constant pressure specific heat for species k
D	Diffusivity coefficient in mixture fraction space
d_p	Soot mean particle diameter
D_s	Soot particle nominal diameter
D_t	Mass turbulent diffusivity coefficient
d_0	Nozzle effective diameter
d_{eq}	Nozzle equivalent diameter
d_{nuclei}	Diameter of incipient soot nuclei
Da	Damköler number
E	Activation energy
h_k	Molar specific enthalpy for species k
J	Ratio between mean scalar dissipation rate and mixture fraction
k	Depending on the context, Boltzmann's constant or turbulent kinetic energy
K_A, K_B, K_Z	Nagle and Strickland-Constable model rate constants
l	Coordinate along a mixing trajectory
$\dot{M}$	Momentum flux
m	Depending on the context, number of C atoms or mass
M_r	r^{th} moment of the particle size distribution function
M_s	Soot molecular weight
M_{nuclei}	Mass of incipient soot nuclei
n	Number of H atoms
N_a	Avogadro's number

N_i	Number density of soot particles of size class i
N_s	Soot number density
P	Pressure
P_χ	Probability density function for scalar dissipation rate
P_Z	Probability density function for mixture fraction
q_i	Rate of progress variable for reaction i
R	Depending on the context, ideal gas constant or spray radius
r	Spray radial coordinate
S	Depending on the context, spray tip penetration or segregation factor for mixture fraction variance
S_c	Turbulent Schmidt number
T	Temperature
t	Time
t^*	Residence time
u	Spray axial velocity
v	Spray radial velocity
V_s	Thermophoretic velocity
W_i	Species i molecular weight
x	Spray axial coordinate
X_i	Species i molar fraction
x_v	Nagle and Strickland-Constable model A site proportion
Y_c	Progress variable
Y_i	Species i mass fraction
Z	Mixture fraction
Z''^2	Mixture fraction variance
Z_i	Element mass fraction namely, C, H and O

Greek

χ	Scalar dissipation rate
γ_i	Species i collision efficiency
μ	Dynamic viscosity
ν	Stoichiometric oxygen-to-fuel mass ratio
ν'_{O_2}	Oxygen stoichiometric coefficient
ν'_{ki}, ν''_{ki}	Reactants and products stoichiometric coefficients for species k and reaction i
$\dot{\omega}_k$	Net production rate of species k
$\dot{\omega}_k$	Reaction rate for k soot subprocess
ϕ	Equivalence ratio
ψ	Reactive scalar
ρ	Density
σ	Parameter for the scalar dissipation rate variance in the log-normal function

θ	Spray cone angle
ε	Turbulent kinetic energy dissipation rate

Sub- and superscripts

a	Referred to air
A	Referred to more reactive sites in the Nagle and Strickland-Constable model
agg	Referred to soot agglomeration
baseline	Referred to baseline case
B	Referred to less reactive sites in the Nagle and Strickland-Constable model
CC	Referred to chain carriers
cell	Referred to cell values
chemical	Referred to chemical time scales
coolflames	Referred to cool flames
dif	Referred to diffusion in mixture fraction space
fuel	Referred to fuel
F	Referred to fuel stream
f	Referred to soot formation
gas	Referred to gas phase
g	Referred to soot surface growth
highT	Referred to high temperature
inert	Referred to inert state
max	Referred to maximum value
MR	Referred to most reactive condition
n	Referred to soot nucleation
O	Referred to soot oxidation through *O*
OH	Referred to soot oxidation through *OH*
O_2	Referred to soot oxidation through O_2
oxidizer	Referred to oxidizer
ox	Referred to soot oxidation
physical	Referred to physical time scales
ref	Referred to a reference condition
rms	Referred to root mean square
steady	Referred to steady state
st	Referred to stoichiometry
s	Referred to soot
tab	Referred to tabulated values in the flamelet manifold
threshold	Referred to threshold value
virt	Referred to the virtual O_2 dummy species
*	Referred to normalized value

Acronyms

0D	Zero-dimensional
AMR	Adaptive mesh refinement
BEV	Battery electrical vehicle
CC	Chain carriers
CFD	Computational fluid dynamics
CI	Compression ignition
CPU	Central processing unit
CR	Combustion ratio
DNS	Direct numerical simulation
ECN	Engine combustion network
EGR	Exhaust gas recirculation
FOV	Field of view
HACA	H-abstraction-C_2H_2-addition mechanism
HCCI	Homogeneous charge compression ignition
HRR	Heat release rate
ICE	Internal combustion engine
ID	Spray ignition delay time
IEA	International energy agency
KH	Kelvin-Helmholtz mechanism
KL	Optical thickness
LCF	Laminar co-flow flame
LCT	Laminar counterflow flame
LES	Large eddy simulation
LOL	Spray lift-off length
LP	Laminar premixed flame
LTC	Low-temperature Combustion
NO_x	Nitrous oxides (NO and NO_2)
NSC	Nagle and Strickland-Constable soot oxidation model
NTC	Negative temperature coefficient
PAH	Polycyclic aromatic hydrocarbon
PCCI	Partially premixed compression ignition
PDF	Probability density function
PISO	Pressure implicit with splitting of operators method
PIV	Particle image velocimetry
PLIF	Planar laser-induced fluorescence
PPC	Partially premixed combustion
PSDF	Particle size distribution function
RANS	Reynolds averaged Navier-Stokes
RCCI	Reactivity controlled compression ignition
RT	Rayleigh-Taylor mechanism
SDM	Sauter mean diameter
SVF	Soot volume fraction
TCI	Turbulence and chemistry interaction
TEM	Transmission electron microscopy

TS	Turbulent spray
TSI	Threshold sooting index
UFPV	Unsteady flamelet progress variable
UFPV-0	Unsteady flamelet progress variable with no presumed probability density function integration
WM	Well-mixed

CHAPTER 1

Introduction

Combustion is at the core of mankind progress and its importance in today's society is undeniable. According to data published by the International Energy Agency (IEA) [1] at this moment, more than 58% of the world's installed power generation capacity relies on combustion. Furthermore, there's a clear trend (see Fig. 1.1) on how the world generates power and combustion is, and will continue to be, a crucial technology in the next three decades. From an application point of view, combustion can be found virtually at any level from electric power generation, and many industrial applications, to propulsion. Many of these applications rely on liquid fuel combustion systems of which nearly 59% worldwide were used in the transportation sector in 2018 and are expected to remain a major player in this sector at least until 2050 according to projections in the international energy outlook from the United States Energy Information Administration [2]. In particular, the internal combustion engine (ICE) dominates the car's market with a 97% share in 2018 and 74% in 2040 [1]. Data shows that battery electric vehicles (BEV) are still relegated to a limited portion of the market. Despite political efforts to ban the use of the ICE, solid arguments have been made to point out that diversity is key in the transportation sector and that further development of the ICE is still much needed [3, 4].

The ICE is the most suitable technology for many applications that demand a wide range of regimes and loads such as heavy-duty applications in which the ICE is the primary choice. The high-energy density of fuels used in an ICE is the essence of its suitability in contrast to battery-based systems. For instance, a lithium-ion battery energy density is approximately two orders of magnitude lower than that of gasoline [5]. Even newer battery systems based on lithium-metal anodes, with higher theoretical energy density compared to lithium-ion batteries, are still far from applicability due to the need of

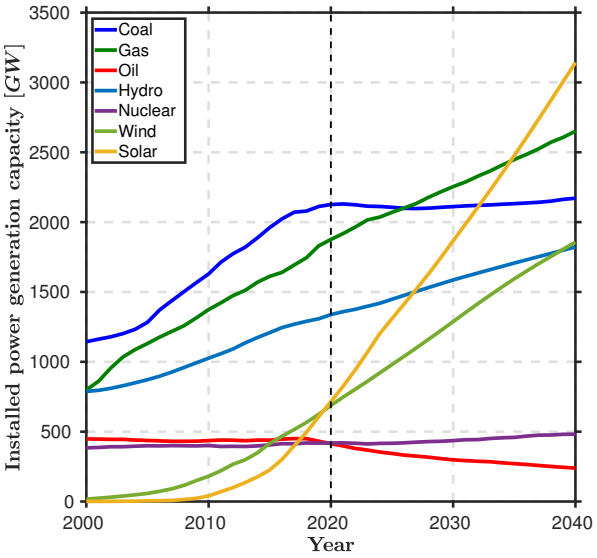

Figure 1.1: *Worldwide installed power generation capacity. Vertical dashed line marks starting year for projections [1].*

improved discharging capacity and the development of novel materials [6]. This last point is crucial as the manufacturing of batteries depends on the use of scarce and expensive rare metals [7].

Unquestionably, the highly suitable ICE has its own share of challenges to be addressed. Flexibility and fuel efficiency, particularly for compression ignition (CI) engines, come at the expense of the NO_x and soot emissions trade-off. From these emissions, soot has gained increased attention in the past years as it poses a thread on the environment as well as on human health. On one hand, soot has been reported to contribute to the change in global surface air temperature either as part of carbonaceous aerosols in the atmosphere [8–10] or by deposition on snow [11, 12]. On the other hand, the implications of inhaling soot particles have been extensively studied [13–16] pointing out to its link with cardiopulmonary diseases. In response to its hazardous nature, stricter legislation on particle matter emissions has been introduced. In Europe, allowed particle emissions for Diesel passenger cars went from 0.14 g/km in the early 90's to 0.0045 g/km and $6 \times 10^{11} particles/km$ with the current legislation [17].

To comply with particle matter emission regulations, much efforts have been placed on the advancement of Diesel particle filters (DPF). This aftertreatment approach on soot reduction has proven effective up to 90% efficiency [18]. Nonetheless, in order to reach those levels of efficiency the DPF

has to be regenerated to mitigate soot loading. Often, DPF regeneration requires higher exhaust temperature which implies more fuel injection and a consequent penalty on fuel consumption efficiency [19]. Another approach to soot reduction is focused on cleaner combustion modes. The concept of cleaner combustion comprises a wide range of technologies from low-temperature combustion (LTC), including homogeneous charge compression ignition (HCCI), premixed charge compression ignition (PCCI), partially premixed combustion (PPC) and reactivity controlled compression ignition (RCCI) [20], to precisely controlled multiple injection strategies [21, 22], the use of biofuels [23, 24] or possibly CO_2 derived fuels [25]. Cleaner combustion modes aim, among other targets, at reducing soot production at its source.

In light of the current scenario, the ICE is expected to remain a key player on the transportation sector. As there's still room for improvement, the study of in-cylinder processes is not only relevant but necessary to continue improving our understanding on soot production and how to mitigate it.

1.1. Context

Combustion in a CI engine is naturally a highly complex process. Thus, the study of isolated, yet highly complex, processes is an alternative that enables a better understanding of fundamental phenomena. Single-hole nozzle spray experiments have made possible the study of many relevant phenomena specially with the development of optically accessible high-temperature, high-pressure vessels [26, 27]. In this type of application, and under CI engine relevant operating conditions, fuel is injected in liquid phase at around 600 m/s into a high-density, high-temperature quiescent air environment. Liquid fuel breaks-up into droplets which consequently vaporize. Fuel vapor mixes with air, a process enhanced by turbulence, and then autoignites. The first phase of combustion is partially-premixed as a consequence of the delay time from the start of injection until the start of combustion. Finally, a mixing-controlled combustion phase is established where NO_x and soot are present at the inner and outer region of the spray, respectively.

Single-hole nozzle sprays have been the subject of different studies carried out around the globe. Many of these studies are framed within the Engine Combustion Network (ECN) [28], an international collaborative effort to establish well-defined test cases that enable the validation of numerical studies through the comparison with reliable and reproducible experimental

data. This thesis is developed within the ECN framework with particular attention to reference test cases known as Spray A and Spray D which are relevant to light-duty and heavy-duty applications, respectively.

1.2. Objective

The research work in this thesis is framed within the study of particulate matter emissions in CI engines. In this context, the main objective is to simulate soot production in Diesel sprays under engine-like conditions using computational fluid dynamics (CFD). Consequently, this thesis covers the assessment of combustion and soot modeling under an approach widely extended in the industry due to affordable computational cost. Within a Reynolds averaged Navier-Stokes (RANS) framework for the treatment of turbulence, a well-mixed and a flamelet based combustion model coupled to a two-equation soot model are the basis of the thesis modeling approach. With soot being at the end of a series of linked events taking place over a wide range of spatial and temporal scales, and despite not being the main objective of this work, spray local and global characteristics are thoroughly analyzed. This extended analysis is primarily focused on spray mixing and combustion phenomena.

Fulfillment of the main objective of this thesis is achieved through the completion of the following tasks:

- Validation of the computational setup under inert conditions.
- Assessment of sub-grid flame structure and turbulence-chemistry-interaction (TCI) influence on combustion.
- Study of the effect of mixing and reactivity boundary condition variations on combustion and soot production.

1.3. Outline of the work

This thesis is structured in six chapters. After the introductory remarks in Chapter 1, a comprehensive review of fundamental concepts is presented in Chapter 2. This chapter is intended to present the reader a global picture of the complexity of soot production. It starts with a full description of the combustion process in a Diesel spray from atomization to the establishment of the characteristic diffusion flame. Then, the current understanding of soot production is outlined before addressing soot models.

Next, Chapter 3 introduces the modeling approach followed in this work. Details on spray, combustion and soot modeling are discussed.

Chapter 4 starts with the validation of results for the inert ECN Spray A and Spray D. Then, global combustion parameters are validated and an extensive analysis of spray autoignition and flame structure at quasi-steady state is presented while emphasizing on the relevance of sub-grid flame structure, TCI and nozzle orifice diameter on the development of combustion.

Chapter 5 is devoted to soot modeling results. Changes in flame structure and soot production induced by different ambient oxygen concentration, temperature and composition as well as different injection pressures and injection strategies are analyzed.

Finally, in Chapter 6 concluding remarks and future works are highlighted.

CHAPTER 2

Fundamentals

In general terms, combustion refers to the event in which heat is released by a chemical reaction involving a fuel and an oxidant. After more than a million years using combustion, humanity's oldest technology, its study is still much needed as the majority of energy support systems relies on it [29]. In the field of propulsion systems, the ICE still remains at the core of most practical applications. The combustion process in this type of devices is turbulent in nature as the heat released in the process induces flow instabilities through buoyancy and gas expansion [30]. Besides releasing heat, the turbulent combustion process in ICEs, and particularly in CI engines, also generates NO_x and soot. This last pollutant has been gaining more attention in the past years and the reason is twofold: First, its impact on human health and air quality [10, 13–16]. Second, the stricter pollutant legislation in which both the amount and the size of soot particles are regulated [17]. If this regulations are to be fulfilled, a clear understanding of the phenomena leading to soot production is needed.

The reacting Diesel spray, the study subject of this work and the working principle for CI engines, involves complex phenomena occurring in a broad range of temporal and spatial scales. Within this context, this chapter aims at presenting a comprehensive review on combustion and soot production in Diesel-like sprays. First, the main phenomena involved in the conventional combustion process of the Diesel spray is described. Then, the current understanding of soot production is reviewed in terms of soot precursors, physical and chemical phenomena. Finally, current trends for soot modeling are also reviewed.

2.1. The combustion process in a Diesel spray

As the working principle in CI engines, the study of the Diesel spray is particularly relevant as the need for cleaner and more efficient engines is ever-increasing. The combustion process in a Diesel spray comprises several physical and chemical processes that interact among them in a time interval in the order of 1 *ms*. The next subsections describe the most relevant phenomena involved following a chain of events starting at the time at which the liquid fuel is injected into the high-density, high-temperature air environment until the time at which combustion is controlled by fuel-air mixing. It should be noted that the description outlined in this chapter considers some simplifications since some processes and its interactions are out of the scope of this work. In this regard, the reader should bare in mind that internal-flow, spray-spray interaction, spray-flow field interaction, wall heat transfer and wall impingement are relevant processes in a CI engine combustion chamber.

2.1.1. Atomization

Atomization refers to the process by which a liquid breaks into droplets. In the context of the Diesel spray, atomization is the first process[1] that takes place when the liquid fuel enters the combustion chamber interacting with the high-density, high-temperature air environment. High-velocity liquid fuel discharged from the injector nozzle starts breaking into droplets thus increasing the contact surface between the liquid phase and the surrounding gas phase. This increased interaction among phases enhances mass, momentum and energy transfer, all of which are relevant phenomena to the consequent steps in the combustion process.

It is common to separate the first milliliters of the spray into two distinctive regions as shown in Fig. 2.1. The closest region to the nozzle orifice is known as the *near field*. It comprises the intact liquid core whose length is referred to as *breakup length* and the predominant phenomenon in this region is *primary atomization*. The consequent region is known as the *far field*. It extends beyond the last position where liquid fuel can be found, a distance referred to as *liquid length*, and in terms of atomization is characterized by *secondary atomization* of droplets interacting with the gas phase.

[1] In the Diesel spray chain of events internal-flow phenomena precedes atomization. Recent experimental [31, 32] and modeling studies [33, 34] emphasize the relevance of these phenomena on the consequent development of the spray.

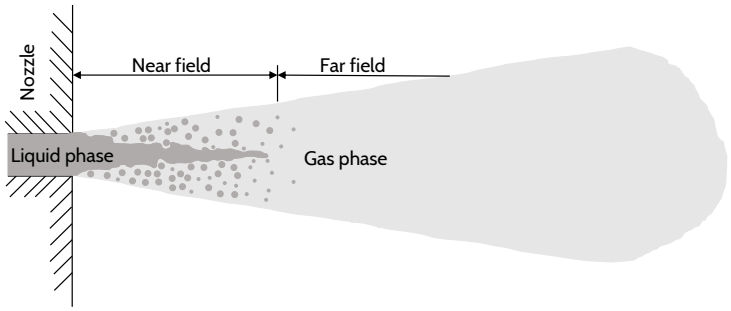

Figure 2.1: *Diagram of spray regions.*

Disintegration of the liquid core in the near field is the consequence of *primary breakup*, a mechanism responsible for the appearance of the first droplets in the spray. The mechanism is governed by complex phenomena including inertial instabilities, turbulence and cavitation. Depending on the nozzle exit velocity, liquid and gas phase properties several breakup regimes can be defined. Reitz and Bracco [35] proposed a classification that includes four regimes:

- The Rayleigh regime at low-Reynolds number where droplets sizes are fairly regular and surface tension effects are predominant.
- The first and second wind-induced regimes at intermediate-Reynolds number where predominant effects are those of aerodynamics forces.
- The atomization regime at higher-Reynolds number where the breakup length tends to zero.

Under CI engine operating conditions, relevant to the Diesel spray, it has been found that only the atomization regime is present [36, 37] implying that the breakup length is independent of the nozzle exit velocity and is in the same order of magnitude as the nozzle diameter. The atomization regime is characterized by a dense intact liquid core and droplets much smaller than the nozzle diameter which increase considerably the degree of complexity for experimental and modeling work [38].

A recent literature review by Magnotti and Genzale [39] illustrates the experimental effort to characterize primary atomization. The authors highlight progress in spray diagnostics from early studies using shadowgraphy [40, 41], with spatial resolution limited to approximately 100 μm, to later improvements in spatial and temporal resolution by the introduction of lasers or LEDs illumination [42, 43]. Magnotti and Genzale concluded that

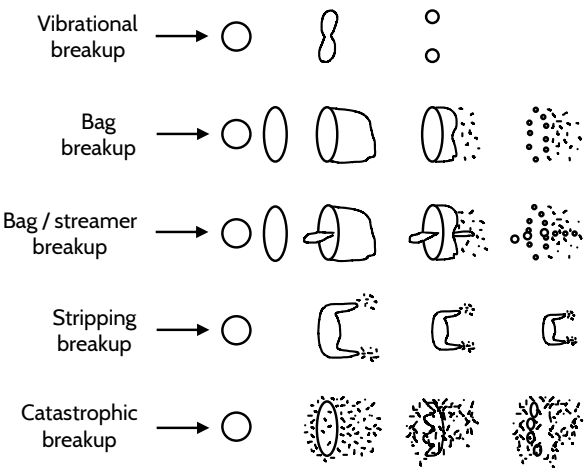

Figure 2.2: *Secondary breakup regimes [38].*

in order to resolve primary droplets from fuel sprays under representative engine operating conditions, further improvement in temporal and spatial resolution is required. Some of today's most promising techniques for the characterization of primary atomization under engine-like conditions are based on the use of X-ray. In this regard, by combining droplets volume and surface area measured through X-ray radiography [44, 45] and ultra-small-angle X-ray scattering [46, 47], the *Sauter mean diameter*[2] (SDM) can be quantified [49–51].

Downstream of the breakup length, relatively large droplets resulting from primary atomization are subject to aerodynamic forces. If these forces are greater than the own surface tension of a droplet, *secondary breakup* takes place and smaller droplets are formed. Several outcomes are possible due to secondary breakup [52] and some of the most common regimes are shown in Fig. 2.2. The transition from one regime to the other can be described in terms of the droplet Weber number which relates aerodynamic forces and the droplet surface tension. Then, vibrational breakup occurs at low-Weber numbers opposite to catastrophic breakup. All regimes are relevant to the Diesel spray, although catastrophic breakup is predominant due to the high-Weber number near the nozzle where atomization phenomena is more intense [38]. Lastly, it is worthwhile to mention that as secondary breakup takes place, droplet-droplet interactions increase giving rise to the

[2]SMD is computed as the droplet volume to surface area ratio. It is an useful metric for droplets drag forces and evaporation rate [48].

appearance of the coalescence phenomenon[3] reported to be one of the main contributors to the high temporal and spatial variability of droplet sizes [53].

At this point, the ultimate outcome of the different phenomena involved in the fuel injection into the high-density, high-temperature air environment is the fast and full atomization of the liquid phase in the near field of the spray. As a consequence, the liquid and the gas phases promptly reach dynamic equilibrium allowing the air-fuel mixture to be characterized by a unique velocity, local composition and thermodynamic conditions [54].

2.1.2. Evaporation and fuel-air mixing

Droplets moving downstream from the nozzle orifice start interacting with the surrounding gas phase promoting air entrainment which is a process linked to the fuel injection induced momentum [55–57]. Entrainment of hot air rises droplets fuel vapor pressure up to evaporation, a process related to three distinctive events namely, droplets deceleration by aerodynamic drag, air heat transfer to droplets and vapor fuel mass transfer to the air [58]. Fig. 2.3 shows an schematic representation of air entrainment and evaporation related phenomena in the fuel-air interface. As a result of evaporation, liquid can only be found from the nozzle exit until a certain axial distance known as the liquid length. This parameter has been extensively studied to characterize the evaporation process in the spray.

It has been experimentally found that the liquid length greatly depends on boundary conditions such as fuel properties [32, 59, 60], environment thermodynamic conditions [55, 56, 61–63] and nozzle orifice diameter [55, 56, 64]. On the contrary, heat released during combustion and injection pressure [55, 56, 60, 62, 63] do not seem to have any influence on the liquid length. Regarding the heat from combustion, it was found by Espey and Dec [61] that the main source from heat transfer to the droplets was the surrounding gas atmosphere since the liquid length was stabilized before the start of combustion. In relation to the injection pressure, Siebers [55] reported that the liquid length is controlled by the fuel-air mixing process. While increasing the injection pressure, the rate of air entrainment is also increased thus the liquid length does not change. Since fuel evaporation is controlled by turbulent mixing, local rates of mass, momentum and energy

[3] Process by which two or more droplets collapse and form a new droplet.

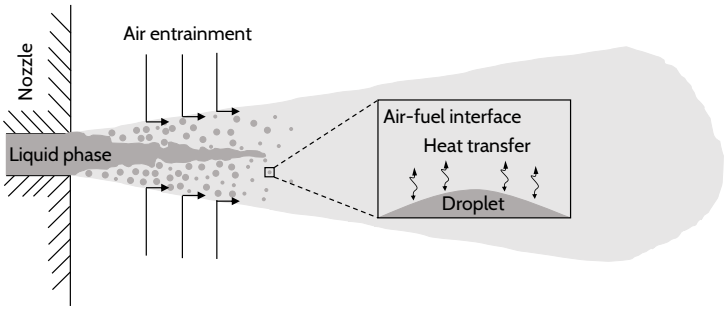

Figure 2.3: *Fuel evaporation and air entrainment schematic [65].*

transfer are less predominant thus reassuring the hypothesis of thermal equilibrium at any point under evaporative conditions in Diesel-like sprays [54].

Following the chain of events, the spray keeps penetrating into the combustion chamber while evaporated fuel mixes with the surrounding air. Both, *spray penetration* (S) and air entrainment are fundamental for the efficient employment of air in the combustion chamber. The experimental characterization of the fuel-air mixing process can be made in terms of macroscopic and microscopic spray metrics. On the macroscopic scale, spray penetration and *spray cone angle*[4] (θ) have been extensively studied[5] [66, 69–72]. From these two parameters, spray penetration has been reported to be the primary estimate for air entrainment in the far field region of the spray [66]. The schematic representation of the spray in Fig. 2.4 shows the spray cone angle and the spray penetration marked at the furthest axial distance reached by the spray tip. It also introduces two distinctive regions in the spray. First, a conical-shaped steady region and a transient region at the head of the spray.

Based on experimental results, several correlations have been proposed [73–77] aiming at establishing a relationship with parameters that can be measured in a straightforward way. Despite differences in proportionality factors most correlations follow the expression

$$S \propto \rho_a^{-0.25} \dot{M}^{0.25} tan(\theta/2)^{-0.25} t^{0.5} \tag{2.1.1}$$

showing the dependency of S on air density (ρ_a), momentum flux ($\dot{M}$), θ and time (t) [78].

[4]Experimental results have shown a strong dependency on optical setup and image processing [66, 67]. Then, in this work more emphasis is made on spray penetration.

[5]A comprehensive review on spray measurements can be found in the work by Fansler and Parrish [68].

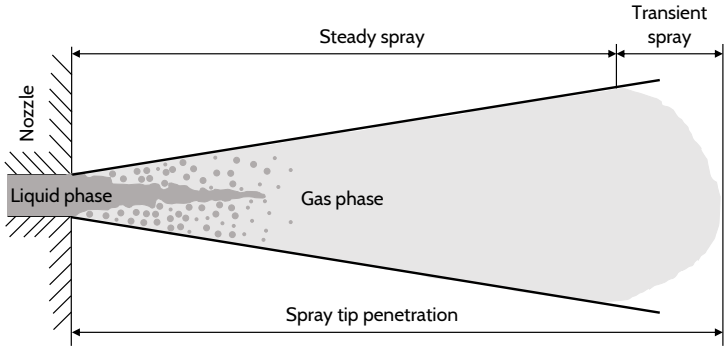

Figure 2.4: *Macroscopic fuel-air mixing spray metrics.*

On the microscopic level, the state of fuel-air mixing is defined based on the *mixture fraction* (Z) concept. An accurate description of the spray mixing state is fundamental for the combustion process due to its tight link to the flame temperature, pollutant emissions and combustion efficiency itself [78]. From a theoretical point of view, the mixture fraction concept has been found to be successful in the description of non-premixed combustion relevant to Diesel-like sprays. In general terms, the mixture fraction is a conserved scalar that defines the state of fuel-air mixing. Classical definitions of Z include those by Bilger [79] and Peters [30]. Both definitions consider the scenario of a two-inlet system with Z bounded between 0 at the oxidizer stream and 1 at the fuel stream with equal diffusivity. Bilger's definition can be expressed based on the conservation of carbon, hydrogen and oxygen atoms according to

$$Z = \frac{Z_C/(mW_C) + Z_H/(nW_H) + 2(Y_{O_2,oxidizer} - Z_O)/(\nu'_{O_2} W_{O_2})}{Z_{C,fuel}/(mW_C) + Z_{H,fuel}/(nW_H) + 2Y_{O_2,oxidizer}/(\nu'_{O_2} W_{O_2})} \tag{2.1.2}$$

where the element mass fraction of C, H and O are denoted as Z_C, Z_H, Z_O and its corresponding molecular weights as W_C, W_H, W_O. Additionally, m and n denote the number of C and H atoms, subscripts $fuel$ and $oxidizer$ denote the fuel and oxidizer streams and ν'_{O_2} denotes the oxygen stoichiometric coefficient.

More recently, classical definitions have been reformulated or extended to account for phenomena not taking into account previously. For instance, Bilger [80] extended his original formulation to make it valid at any point either in the liquid or gas phase with specific formulations based on heat or mass transfer. Similarly, Franzelli et al. [81] introduced a new variable

able to capture the evolution of the disperse phase even if no evaporation takes place. This new mixing-describing variable, coined by the authors as effective composition variable, is a function of the gaseous mixture fraction and the liquid-to-gas mass ratio. Lastly, Gomet et al. [82] extended the two-inlet system formulation to a multiple-inlet system formulation relevant to applications in which, for example, an additional oxygen-enriched stream is introduced to favor flame stabilization.

In the field of experiments, the use of laser-based diagnostics is common for the quantification of the fuel-air mixing process although it is a difficult endeavor due to low signal strength, elastic scattering interferences and limited spatial resolution [78].

2.1.3. Autoignition

Up until this point, the description of the Diesel spray coincides with that of an inert spray. Nonetheless, at this point autoignition is next in the chain of events. Autoignition is the working principle for the start of combustion in CI engines and it refers to the phenomenon associated with the spontaneous burning of a fuel-air mixture. The time elapsed until the start of combustion is known as *ignition delay* (ID), a time interval composed of characteristic physical and chemical times related by the Damköler number (Da):

$$Da = \frac{t_{physical}}{t_{chemical}} \tag{2.1.3}$$

Steps leading to autoignition can be summarized as follows [83]:

- Formation and accumulation of chain carriers[6] (CC) through slow and not very exothermic reactions.
- Fast and highly exothermic reactions, promoted by a critical concentration of CC leading to formation of combustion products and decomposition of CC.

One of the main features of autoignition is the negative temperature coefficient (NTC) behavior. While the temperature increases due to the first exothermic reactions taking place, there is a temperature range (NTC zone) where a loss of reactivity is distinguished. NTC behavior is attributed to the

[6] Active radicals with chain behavior accumulated during ID and consumed when ignition occurs. These active radicals are also characterized by multiplier effect on its reaction rate [83].

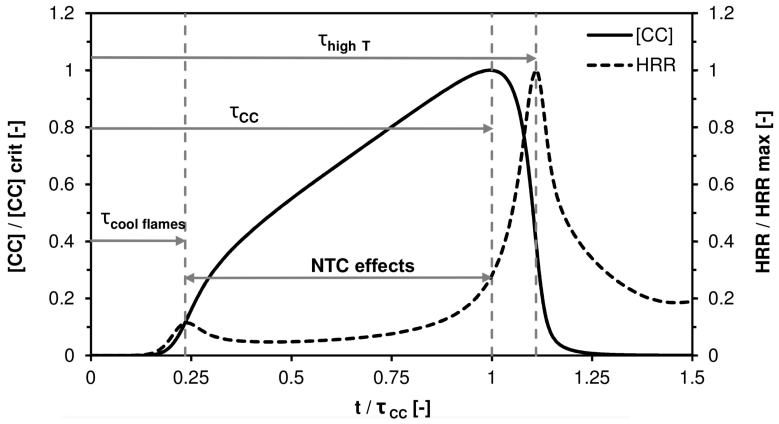

Figure 2.5: *Autoignition characteristic times [83].*

formation of long-chain stable olefins competing with the formation of CC [84]. A pronounced NTC behavior results in a two-stage ignition pattern with a distinguished first brief exothermic stage known as *cool flames* [85].

A schematic of a typical two-stage autoignition pattern is presented in Fig. 2.5. The solid black line depicts the normalized CC concentration[7] while the dashed line shows the normalized heat release rate (HRR).[8] At first, there is a simultaneous raise of CC concentration and HRR that ends with the loss of reactivity marking as well the end of the cool flames stage at time $\tau_{coolflames}$. Next, HRR remains virtually flat during the NTC period while CC concentration continues rising until its maximum value at time τ_{CC} where a rapid increase of HRR starts taking place. Finally, CC concentration decreases as a consequence of combustion and the HRR reaches its maximum level at time τ_{highT}.

In the particular case of the Diesel spray, a global overview of autoignition can be summarized on the basis of the work by Higgins et al. [86]:

- Physical induction: it comprises all phenomena related to atomization, evaporation and fuel-air mixing and it extends until the simultaneous rise of pressure and chemiluminescence become detectable. During this period, fuel evaporation induces a drop in temperature that inhibits ignition. Continued air entrainment raises the fuel-air mixture temperature giving way to the beginning of first-stage ignition.

[7] Normalized by the critical concentration of CC.
[8] Normalized by the maximum HRR.

- First-stage ignition: it extends from the first raise of pressure and chemiluminescence to the time of rapid heat release rate increase. Along this period, fuel is consumed in a broad averaged fuel-rich mixtures of the spray downstream of the liquid length until the tip of the spray. Small quantities of heat are released increasing temperature and pressure which contributes to the start of second-stage ignition.

- Second-stage ignition: increased temperature levels promoted by hot air entrainment and first-stage ignition favors hydrogen peroxide reactions releasing considerable amounts of heat noticeable in the strong HRR premixed-burn peak [58, 87].

More recently, Dahms et al. [88] presented a conceptual model for turbulent ignition of Diesel-like sprays supported by Rayleigh-scattering and CH_2O PLIF with simultaneous schlieren imaging along with one-dimensional non-premixed flame calculations. The authors showed that first-stage chemical reactions initiate at the hot spray radial periphery. From this location, a cool flame wave transports chemical species and heat toward the colder and richer mixtures in the spray core. The completion of the cool flame wave is marked by a quasi-homogeneous state of first-stage ignition with a temporary decrease of chemical and diffusion activity. Finally, second-stage high-temperature ignition occurs over a broad range of rich mixtures forming step gradients that initiate the propagation of a turbulent flame.

2.1.4. Mixing-controlled combustion

In the latest stage of the Diesel spray combustion process, the premixed combustion initiated by autoignition transitions into a diffusion flame. The flame front formed is sustained by the supply of fuel and oxygen whose rate depends on the momentum provided by fuel injection. As a consequence, the combustion process during this phase is mixing-controlled.

A schematic of the flame structure proposed by Dec [89] is shown in Fig. 2.6. Dec's conceptual model is one the most spread visions of the structure of the reacting Diesel spray as it provides a global overview of the complex phenomena taking place. A key feature observed in Fig. 2.6 is that the flame front (solid line) does not reach the nozzle outlet. The distance from the nozzle outlet to the most upstream location of the lifted flame is known as *lift-off length* (LOL). The rich mixture found along the LOL is burned in the partially premixed zone. Further downstream, the flame front surrounds the spray core constituted by intermediate combustion products

and soot which are oxidized in the vicinity of the flame front. Lastly, NO_x are formed in the outer region of the spray favored by lean mixtures and high temperature.

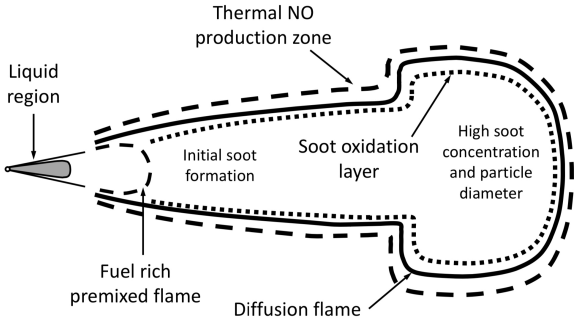

Figure 2.6: *Schematic of the reacting Diesel spray based on Dec's conceptual model [90].*

Continuous advancements in optical diagnostics have lead the way toward a detailed characterization of the structure of Diesel-like reacting sprays. Maes [91] has reported results on the structure at quasi-steady state from experiments performed at various institutions around the world in the context of the ECN. Results include measurements of low- and high-temperature combustion species namely CH_2O and OH and measurements of polycyclic aromatic hydrocarbons (PAHs) and soot. Maes found CH_2O in fuel-rich mixtures downstream of the liquid length and upstream of the LOL. Combined OH and CH_2O measurements show that the former species is consumed around the high-temperature reaction zone. PAHs were visible around the spray center followed by soot ultimately oxidized in the flame front.

Optical diagnostics combined with numerical simulations have also allow a better understanding on relevant features such as the lift-off length. Understanding the mechanisms that drive the stabilization of the flame at the LOL location is inherently a part of the path toward cleaner combustion. In that direction, it has been reported that the stabilization of the flame is governed by autoignition and the downstream topology of the flame [92]. The importance of the LOL resides on its tight link to soot production. The increase in the lift-off length location implies that the flame stabilizes at locations with leaner mixtures giving place to a flame less prone to produce soot up to the point where soot is virtually non-existing [93–95].

2.2. Current understanding of soot production

Ideally, complete stoichiometric combustion of a hydrocarbonated fuel at all points in the combustion chamber of an ICE would lead to the maximum heat release possible and would produce mainly water and carbon dioxide. Not surprisingly, this not the case for any ICE and incomplete combustion products can be found in the form of carbon monoxide, unburned hydrocarbons and, most relevant to this work, soot. The appearance of soot is responsible for the yellowish luminosity of a flame, a phenomenon related to radiation. Increased heat radiation induced by soot is to be avoided in ICEs as it affects efficiency, but it is a desirable feature in industrial furnaces as it improves heat transfer [96].

Soot is a solid carbonaceous substance resulting from fuel pyrolysis at high temperature [97, 98]. Soot is mostly composed of carbon, being C_8H a common empirical formulation [99], although other elements can be found in small quantities. In CI engines, reported soot composition varies depending on the location at which the sample is collected. Thereby, exhaust soot mainly contains carbon and oxygen [100], meanwhile phosphorus, sulfur, atomic oxygen, calcium and zinc can also be found in crankcase soot as the result of the interaction with lubricating oil and due to the wear of engine parts [101]. In terms of structure, soot particles are grape-like clusters of small spheres called primary particles or spherules [29, 58]. Fig. 2.7 shows a typically transmission electron microscopy (TEM) soot structure image with spherules in the range of 11 *nm* and clusters with several sizes. Recent advancements in soot structure characterization have shown that despite greatly variations in the size of spherules, there is a correlation with aggregate size. This finding suggests that the growth of soot particles follows a similar relation for common combustion systems [102].

The study of soot physical and chemical properties in CI engines is an active field of research as can be concluded from the extensive literature review by Wang et al. [103]. The reviewed studies found that composition and structure of soot depend on engine speed and load and more importantly, results show that physicochemical soot properties are related to changes in oxidation reactivity hence on the total amount of soot produced.

Soot production is a kinetically controlled process composed of highly coupled chemical and physical phenomena including gas phase chemical kinetics, particle dynamics and heterogeneous surface reactions [29]. Despite the complexity and the inherent uncertainties of soot production, there is consensus on the main steps involved [98]. Fig. 2.8 depicts the schematic

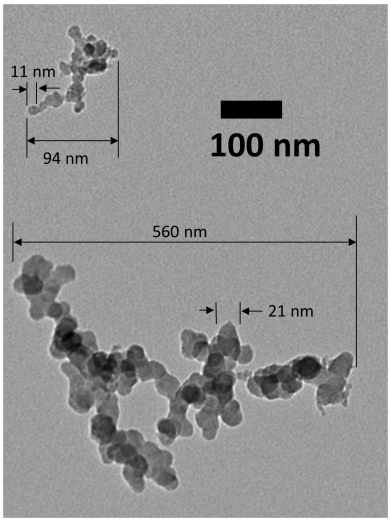

Figure 2.7: *Soot structure image by transmission electron microscopy [102].*

reaction path proposed by Bockhorn [96] in which premixed combustion produces PAHs that later give place to primary particles by nucleation. Small incipient particles then grow in size while reducing in number by condensation, coagulation and surface growth, all simultaneous processes taking place along with oxidation. In the following subsections, the current understanding of soot production is presented through the description of these phenomena.

2.2.1. Gaseous soot precursors formation

PAHs are formed under fuel-rich conditions from unsaturated hydrocarbons and are the basis upon which soot is formed. From unsaturated hydrocarbons, acetylene is the most relevant species not only for the formation of PAHs but also for its growth [29, 96].

The starting point in the evolution of PAHs is the formation of single ring aromatic species. Although benzene is the first aromatic ring, phenyl group and cyclopentadienyl are also involved in the chemical path toward PAHs. Several reactions have been proposed to describe the first aromatic cycle formation and it still remains an open topic [104].

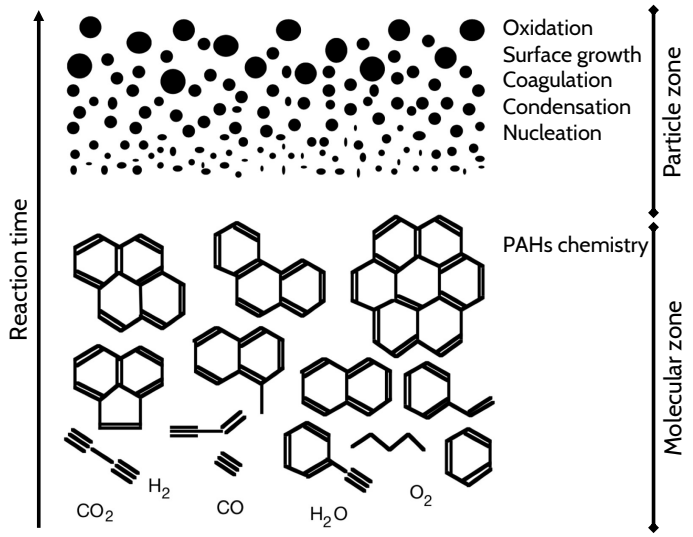

Figure 2.8: *Soot production reaction path schematic [29].*

Similarly to the first aromatic cycle formation, there are several paths that have been proposed over the years to describe the transition of single ring aromatics into PAHs. One of the first elementary reaction mechanisms was proposed by Bittner and Howard [105]. This mechanism explains the formation of naphthalene through the addition of acetylene to phenyl radicals and later to styryl radicals. Another possible path into PAHs formation is described by the H-abstraction-C_2H_2-addition (HACA) mechanism in which molecules grow as a result of alternation of radical formation by hydrogen atom attack and acetylene addition [106, 107]. Finally, PAHs growth and initiation by other species have been reported although numerical simulation results indicate that these pathways end up converging to an acetylene-addition path [108]. The complexity of describing the pathways toward PAHs growth is linked to the transition of large PAHs in the gaseous phase to form the first soot particle trough nucleation.

2.2.2. Physical phenomena

The transition of gaseous soot precursors to the solid phase with the consequent collisional phenomena associated is described in this section. Physical phenomena (see Fig. 2.9 for a graphical summary) includes processes acting on the total soot mass produced (nucleation and condensation) and processes acting on the soot number density (coagulation and agglomeration).

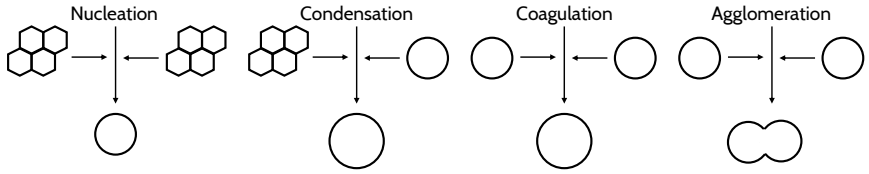

Figure 2.9: *Physical phenomena in soot production [98].*

The appearance of the first soot particles is driven by *nucleation*. Literature reviews by Wang [109] and more recently by Wang and Chung [110] underline that even today particle nucleation remains as one of the least understood soot production processes. Even if the first soot particles, also called nuclei, do not significantly contribute to total soot mass, these are fundamental for mass increase through surface growth. Indeed, nuclei formation rate is directly related to the total soot mass produced [99].

Conceptually, chemical growth and collision of PAHs are two of the most common pathways for describing particle nucleation. In the first case, nuclei is the result of PAHs chemical coalescence [111, 112] while in the second case nuclei forms through physical coalescence [107, 113]. Neither of these pathways is successful in describing the complex nucleation process independently. On one hand, the chemical coalescence pathways fails to describe nucleation in the presence of low H radical concentration. On the other hand, nucleation through physical coalescence is limited by the need of difficult-to-form large PAHs [110].

Despite its inherent limitations, physical coalescence of PAHs is widely extended as a main contributor to soot nucleation. In this context, pyrene dimerization has been extensively used to characterize the transition from the gaseous soot precursor phase toward nuclei. Both experimental and simulation results suggest that collisional phenomena involving pyrene is a suitable way to synthesize the particle nucleation process [113–116].

With the appearance of nuclei, collisional phenomena become relevant. Collisions include PAHs-soot interactions and soot-soot interactions. The collision of PAHs in the gaseous phase with soot particles is known as *condensation* and is a process contributing to the increase of soot mass. Nevertheless, experimental observations suggest that the condensation process is reversible to some extent [117]. This observation has motivated numerical studies that show promising results while underlining the necessity of further research on this topic [114, 118–120].

The collision of soot particles among themselves receives the name of *coagulation*. This process does not intervene in the total soot mass produced but it controls the soot number density. Through coagulation, the boundary between two colliding particles disappears to form a new particle reducing total surface area. In general terms, coagulation is most likely to involve a large soot particle (large surface area) and a small soot particle (higher velocity compared to a large particle) [109]. As particles age, the outcome of soot-soot interactions might not be a new bigger particle but an aggregate of sticked particles [108]. The latter process is called *agglomeration* and it can be seen as a subprocess of coagulation.

2.2.3. Chemical phenomena

Chemical phenomena (graphical summary in Fig. 2.10) taking place on the surface of soot particles include surface growth and oxidation. Neither of these processes act on soot number density but its balance determine most of the total soot mass produced.

Surface growth is the process of mass addition to soot particles through the adsorption of gas phase species of which acetylene is generally accepted as the main contributor [121–123]. The surface growth process is not fully understood, but experimental studies have pointed to semi-empirical descriptions following first-order kinetics [123, 124]. From another point of view, surface growth chemical reactions can be seen as analogous to those related with PAHs growing according to the hypothesis of chemical similarity [107, 125]. Under this hypothesis, surface growth is assumed to be governed by the HACA mechanism. The abstraction of H atoms from the $C-H$ bonds in the surface of soot particles forms radicals that later react with acetylene propagating growth [108]. Experimental studies have also pointed to the existence of an aging phenomenon that causes surface growth rate to decrease with the extend of particle growth [121, 126, 127] thus increasing the complexity of this process. The surface growth process is of paramount importance since, in conjunction with the oxidation rate, it has been reported to be the major contributor to the total amount of soot mass produced [128–130].

On the other hand, when discussing soot production, *oxidation* is normally the last process described although it starts as soon as nuclei appears and lasts throughout the whole soot production process. Unlike any of the other processes, oxidation is the only one reducing the total amount of soot produced. Several species have been reported to contribute to soot oxidation. A recent review by Wang and Chung [110] points at OH and

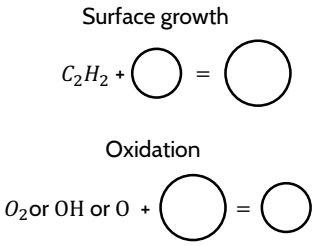

Figure 2.10: *Chemical phenomena in soot production [98].*

O_2 as the dominant species. The first species is particularly relevant for high-temperature oxidation. The second species showed two distinctive phenomena, one related to a decrease in the reactivity as oxidation progresses and the second related to faster oxidation for particles containing curved PAHs structures as compared to planar PAHs. There is a general consensus on the predominance of OH and O_2 for soot oxidation with less relevant contributions from O [29, 131, 132]. Still, a recent study by Frenklach et al. [133] identified a critical role of O atoms. Soot embedded five-member rings are observed to be oxidized by O atoms, a process that was also observed to ultimately control the overall oxidation rate. The authors emphasize that their findings are consistent with the general consensus regarding the relevance of OH and O_2. The authors also remark that oxidation through O atoms is still a feature of the highly complex nature of the mechanisms involved in soot oxidation.

2.3. Soot modeling

In order to meet ever-stricter particulate matter regulations in the automotive sector, tools are required to help guide the development of combustion modes and devices that can comply these regulations. Computational tools need to advance in accordance to the current understanding of the complex soot production process. In this section, a review on soot modeling approaches is made. In this regard, one of the most common classifications is based on the review work by Kennedy [134] in which soot modeling efforts at the time were classified in empirical correlations, semi-empirical models and models with detailed chemistry. Two decades later after the work presented by Kennedy, models have continued to evolve toward more comprehensive descriptions of soot production. In this section, soot modeling work is

reviewed based on the number of soot relevant quantities described. Thus, models are classified in empirical correlations and one-equation models, two-equation models and lastly detailed models.

2.3.1. Empirical correlations and one-equation models

In a first approximation, soot modeling can be approached by empirical correlations based on experimental data. This approach is particularly useful in the automotive industry as a non-expensive way to link soot emissions to fuel type and engine operating conditions. Aiming at characterizing the soot tendency of fuels, Calcote and Manos [135] proposed a threshold sooting index (TSI) on the basis of a critical equivalence ratio. The TSI, later extended to fuel mixtures by Olson et al. [136], is still a broadly used soot indicator today [137–139]. The concept of a critical equivalence ratio was also used by Takahashi and Glassman [140] and Harris et al. [129] in their attempt to characterize soot tendencies. The authors added the flame temperature and C/H ratio to the correlation and reported satisfactory results.

Although effective in predicting the soot tendency of a fuel or mixture, simple empirical correlations are not sufficient to assess the complete effect of operating conditions and time dependency of soot evolution in practical devices. Such is the case of CI engines in which conditions beyond mixture-related quantities and fuel structure need to be accounted for. In this regard, Khan et al. [141] formulated the rate of particle formation in terms of pressure, equivalence ratio of unburned gas and temperature allowing the soot mass loading (expressed in kg/m^3) to be tracked as a function of time. Similarly, Mehta and Das [142] proposed a correlation accounting for the effect of the spray and swirl mixing rate, fueling rate, compression ratio, temperature at injection and engine speed.

Under the need of more details in the soot production process in CI engines, Hiroyasu et al. [143] proposed a one-equation model that describes the total amount of soot produced in terms of formation and oxidation processes according to

$$\frac{dm_s}{dt} = A_f m_{fuel} P^{0.5} e^{-E_f/RT} - A_{ox} m_s X_{O_2} P^{1.8} e^{-E_{ox}/RT} \tag{2.3.1}$$

where the subindex f and ox refer to soot formation and oxidation, respectively. E_f and E_{ox} are the activation energy for the two controlling processes and lastly A_f and A_{ox} are scaling factors used to match the target experi-

mental data. In Equation 2.3.1, the soot formation mechanism is modeled as a first-order reaction from fuel vapor (m_{fuel}) while oxidation follows a second-order reaction between soot (m_s) and oxygen molar fraction (X_{O_2}).

Hiroyasu's model is among the most widely used soot models for CI engines, partly due to its simple formulation and low-computational cost for CFD simulations. Although, it should be kept in mind that its predictability is limited as it heavily relies on the choice of pre-exponential factors and activation energies [144–146]. The Hiroyasu-NSC model, so called for the incorporation of the work by Nagle and Strickland-Constable [147], modified the original Hiroyasu's formulation considering a different approach for determining the oxidation rate. The Nagle and Strickland-Constable model (NSC) describes carbon oxidation by two mechanisms involving more reactive A sites and less reactive B sites yielding to the net reaction rate in units of $kmol/m^2s$ according to

$$R_{Total} = \left(\frac{K_A P_{O_2}}{1 + K_Z P_{O_2}} \right) x_v + K_B P_{O_2} (1 - x_v) \tag{2.3.2}$$

where P_{O_2} is O_2 partial pressure and the proportion of A sites is determined as

$$x_v = \frac{P_{O_2}}{P_{O_2} + K_T / K_B} \tag{2.3.3}$$

with the rate constants given by

$$K_A = 20 e^{-15098/T} \tag{2.3.4}$$

$$K_B = 4.46 \times 10^{-3} e^{-7650/T} \tag{2.3.5}$$

$$K_T = 1.51 \times 10^{5} e^{-48817/T} \tag{2.3.6}$$

$$K_Z = 21.3 e^{2063/T} \tag{2.3.7}$$

Assuming soot particles are spherical and uniform in size, Equation 2.3.1 can be rewritten as

$$\frac{dm_s}{dt} = A_f m_{fuel} P^{0.5} e^{-E_f/RT} - A_{ox} m_s \frac{6}{\rho_s D_s} R_{Total} M_s \tag{2.3.8}$$

where ρ_s, D_s and M_s are the soot density, nominal particle diameter and molecular weight, respectively.

The Hiroyasu-NSC model has also been extensively used for CI engines CFD simulations. Patterson et al. [148] investigated the effects of injection pressure and split injections using the Hiroyasu-NSC model pointing at more realistic results when this model was used. More recently, Micklow and Gong [149] extended the Hiroyasu-NSC model to account for the effect of oxidation through *OH* finding that this oxidation mechanism plays an important role in the late combustion cycle when O_2 concentrations are low. Dempsey et al. [150] carried out a comprehensive numerical study of soot production in a CI engine over a wide range of operating conditions and fuel injection setups (including level of exhaust gas recirculation, nozzle number of holes and diameter, injector included angle, start of injection and injection pressure) with a particular focus on piston bowl design (including a "Mexican hat", reentrant and non-axisymmetric profiles). The authors highlighted the limitations of the Hiroyasu-NSC model in accurately predicting soot. Despite the overall good agreement for all injection setups using the baseline "Mexican hat" piston bowl profile, it was found that the model either under-predicted or over-predicted engine-out soot emissions for the reentrant and non-axisymmetric profiles, respectively.

Under simpler conditions, compared to those of a CI engine, Moiz et al. [151] assessed the Hiroyasu-NSC model capabilities to predict soot production in a single Diesel-like spray in a constant-volume combustion vessel following a multiple-injection strategy. The results show good qualitative agreement with experimental data for a baseline setup with 900 *K* ambient temperature, 0.3 *ms* pilot injection, 0.5 *ms* dwell time and 1.2 *ms* main injection. The model also qualitatively reproduced expected trends when varying ambient temperature and dwell time.

Over the years, other one-equation soot models have been proposed following the two-step approach upon which the Hiroyasu's model was formulated. The capabilities of these models have been tested in laminar non-premixed flames [152] and, more relevant to this work, CI engines [153, 154]. Despite the field of research, one-equation soot models have proven to be computationally efficient and useful in predicting soot trends but have shown limited capabilities in terms of quantitative comparisons with experimental results when operating conditions are varied.

2.3.2. Two-equation models

Aiming at a more comprehensive description of the soot production process, two-equation soot models incorporate soot subprocesses beyond the simplified formation-oxidation formulation used in one-equation models. In fact,

most two-equation soot models are based on the phenomenological description outlined in Section 2.2. The modeling of surface-related phenomena in a two-equation soot model requires solving an additional equation i.e. one equation is solved for soot mass fraction and another one is solved for soot number density causing just a minor increase in computational cost compared to one-equation models.

Early works include the model proposed by Tesner et al. [155]. In their work, soot measurements in an acetylene-hydrogen flame served as basis for developing a model that included a simple equation for the rate of soot nuclei production and one for soot number density. This last equation was required to model the decrease in nuclei concentration through collisional phenomena. From another perspective, Moss et al. [156] introduced a model that extended beyond nuclei formulated on the basis of laminar ethylene-air flame measurements. The increase in soot volume fraction was modeled through surface growth and inception of new particles while soot number density was considered to increase and decrease due to inception and coagulation, respectively. The model would be later reformulated to account for soot oxidation through OH and O_2 [157].

Leung, Lindstedt and Jones [158] proposed one of the most extensively used two-equation soot models. The model was originally formulated and validated for laminar counterflow flames although the authors emphasized on its possible applicability to turbulent flames. Soot production is approached through four global reaction steps solved for conservation equations of soot mass fraction and soot number density. The total soot mass predicted is the result of the competition between nucleation, surface growth and oxidation steps. Nucleation is assumed to be governed by products of fuel pyrolysis from which acetylene is considered as the main contributor according to

$$C_2H_2 \longrightarrow 2C(s) + H_2 \tag{2.3.9}$$

The reaction rate for the nucleation step was formulated to account for the formation of incipient particles and initial surface growth following

$$\dot{\omega}_n = 1 \times 10^4 e^{-21100/T}[C_2H_2] \tag{2.3.10}$$

where $[C_2H_2]$ denotes the molar concentration of acetylene. Henceforth, soot subprocesses reaction rates are in units of $kmol/m^3s$ and species molar concentration, in units of $kmol/m^3$, are denoted by square brackets.

The second step contributing to the increase of soot mass is surface growth. Indeed, surface growth by addition of acetylene is the governing step for the increase of soot mass following

$$C(s) + C_2H_2 \longrightarrow 3C(s) + H_2 \tag{2.3.11}$$

with the reaction rate defined as

$$\dot{\omega}_g = 6 \times 10^3 e^{-12100/T} \sqrt{A_s}[C_2H_2] \tag{2.3.12}$$

where the number of active sites for surface growth is assumed to be proportional to the square root of soot surface area (A_s). Then, soot surface area in units of $1/m$ can be expressed as

$$A_s = \pi \left(\frac{6Y_s}{\pi \rho_s N_s} \right)^{2/3} \rho N_s \tag{2.3.13}$$

with Y_s, N_s, ρ_s and ρ denoting soot mass fraction, soot number density, soot density (set to be that of graphite i.e. 2000 kg/m^3) and mixture density, respectively.

Oxidation of soot is considered through O_2 based on the work by Lee, Thring and Beér [159]. The O_2 oxidation step is described according to

$$C(s) + \frac{1}{2}O_2 \longrightarrow CO \tag{2.3.14}$$

with rate constants adjusted to target the maximum specific soot oxidation rate in a laminar co-flow methane-air flame yielding to

$$\dot{\omega}_{O_2} = 1 \times 10^4 T^{0.5} e^{-19680/T} A_s[O_2] \tag{2.3.15}$$

From the last three subprocesses, soot nucleation not only contributes to the increase of soot mass but also to the increase of soot number density through

$$\dot{\omega}_{n,N_s} = \frac{2N_a}{C_{min}} \dot{\omega}_n \tag{2.3.16}$$

where N_a is Avogadro's number and C_{min} (set to be 100 [158]) is the number or carbon atoms in incipient nuclei. Lastly, the decrease in soot number density due to agglomeration is modeled using a normal square dependence through

$$nC(s) \longrightarrow C(s)_n \tag{2.3.17}$$

with the reaction rate defined according to

$$\dot{\omega}_{agg} = 2C_a \left(\frac{6M_s}{\pi\rho_s}\right)^{1/6} \left(\frac{6kT}{\rho_s}\right)^{1/2} \left(\frac{\rho Y_s}{M_s}\right)^{1/6} (\rho N_s)^{11/6} \tag{2.3.18}$$

C_a is the agglomeration constant (set to 9 [158]), M_s is the soot molecular weight set to be that or carbon (12 $kg/kmol$), k is the Boltzmann's constant ($1.38054x10^{-23}$ J/K) and T is the mixture temperature.

Since the Leung, Lindstedt and Jones [158] model[9] was first introduced in 1991 it has been extensively used for different practical applications ranging from laminar counterflow flames, the application upon which the model was developed, to laminar co-flow and even turbulent spray applications. Table 2.1 summarizes research work from the last two decades where the Leung model has been used. The first table entry (highlighted with bold font) is the original Leung model and is included as a reference point to compare with later modifications proposed by other authors. For the sake of brevity, if more than one paper has been published by the same group of authors then just the most recent work to date is included. In Table 2.1 particular attention is paid to the formulation of nucleation and surface growth reaction rates since most of the proposed modifications are carried out on these subprocesses. On the contrary, source terms for soot number density remain barely unchanged[10] and are not included in Table 2.1. Depending on the application, several values for the pre-exponential factor for the nucleation and surface growth steps have been reported with the aim of matching experimental data. As for oxidation, the reaction rates proposed by Lee, Thring and Beér [159] (Lee for brevity), Bradley et al. [161] (Bradley for brevity), Nagle and Strickland-Constable [147] (NSC), Fenimore and Jones [163] (Fenimore for brevity) and Neoh et al. [165] (Neoh for brevity) are used fairly regularly and the cases where these formulations have been modified are denoted by a superscript.

The different Leung model formulations proposed over the years evidence that even if the model brings a more comprehensive description of soot production, compared to simpler one-equation models, the description is not sufficiently general and some degree of calibration is still required to match experimental results. Besides different constant values, a potential way of improving results relies on the soot precursor choice. In this regard, Vishwanathan and Reitz [168] extended the original Leung model to tar-

[9] From this point the model will be referred to as Leung model.

[10] Formulations are identical with minor differences for some constants with the exception of the work in [169] and [173] where agglomeration is neglected.

Table 2.1: *Review of two-equation soot models. Last three columns show the references for oxidation reaction rates. The acronyms LCT, LCF, LP and TS stand for laminar counterflow flames, laminar co-flow flames, laminar premixed flames and turbulent sprays, respectively. All reaction rates in units of* $[kmol/m^3s]$.

Ref.	Flame	Nucleation	Surface growth	O_2	OH	O
[158]	**LCT**	$\mathbf{1x10^4e^{-21100/T}[C_2H_2]}$	$\mathbf{6x10^3e^{-12100/T}\sqrt{A_s}[C_2H_2]}$	**Lee**[a] [159]	-	-
[160]	LCF	$0.63x10^4e^{-21100/T}[C_2H_2]$	$0.75x10^3e^{-12100/T}A_s[C_2H_2]$	Lee[a] [159]	Bradley[a] [161]	-
[162]	LCF	$1.7x10^3e^{-7548/T}[C_2H_2]$	$6x10^3e^{-6038/T}A_s[C_2H_2]$	NSC[a] [147]	Fenimore[a] [163]	-
[164]	LCT	$1x10^4e^{-21100/T}[C_2H_2]$	$3.468x10^3e^{-12100/T}A_s[C_2H_2]$	Lee [159]	Neoh [165]	Bradley [161]
[166]	LCT	$6.48x10^4e^{-21100/T}[C_2H_2]$	$9.0006x10^3e^{-12100/T}A_s[C_2H_2]$	Lee [159]	Neoh [165]	-
[167]	LCF	$1x10^4e^{-21100/T}[C_2H_2]$	$6x10^3e^{-12100/T}\sqrt{A_s}[C_2H_2]$	NSC [147]	Fenimore [163]	Bradley [161]
[168]	**TS**	$\mathbf{2x10^3[A_4]}$	$\mathbf{9x10^4e^{-12100/T}\sqrt{A_s}[C_2H_2]}$	**NSC**[a] [147]	**Fenimore**[a] [163]	**Bradley** [161]
[169]	LP	$7.7x10^6e^{-21100/T}[C_2H_2]$	$3x10^{-7}e^{-12100/T}(\pi d_p^2)^{\alpha}\rho N[C_2H_2]$	Lee [159]	Bradley [161]	-
[170]	TS	$1x10^4e^{-21100/T}[C_2H_2]$	$3x10^3e^{-12100/T}\sqrt{A_s}[C_2H_2]$	Lee [159]	Bradley [161]	-
[171]	LCF	$1x10^4e^{-21100/T}[C_2H_2]$	$6x10^3e^{-12100/T}\sqrt{A_s}[C_2H_2]$	NSC [147]	Fenimore [163]	Bradley [161]
[172]	TS	$1x10^4e^{-21100/T}[A_4]$	$14e^{(P/P_{ref})^{1.4}}e^{-12100/T}\sqrt{A_s}[C_2H_2]$	Lee [159]	Fenimore [163]	-
[173]	LCT	$1x10^3e^{-16103/T}[C_2H_2]$	$7x10^2e^{-10064/T}\sqrt{A_s}[C_2H_2]$	NSC [147]	Fenimore [163]	Bradley [161]
[174]	TS	$1x10^4e^{-21100/T}[C_2H_2]$	$9x10^4e^{-12100/T}\sqrt{A_s}[C_2H_2]$	NSC [147]	Fenimore [163]	Bradley [161]
[174]	TS	$2x10^3[A_4]$	$9x10^4e^{-12100/T}\sqrt{A_s}[C_2H_2]$	NSC [147]	Fenimore [163]	Bradley [161]
[175]	TS	$1x10^4e^{-21100/T}[C_2H_2]$	$3.99x10^3e^{-12100/T}\sqrt{A_s}[C_2H_2]$	Lee [159]	Bradley [161]	-
[176]	TS	$1x10^4e^{-21100/T}[C_2H_2]$	$6x10^3e^{-12100/T}\sqrt{A_s}[C_2H_2]$	Lee [159]	Neoh [165]	Bradley [161]
[177]	TS	$1x10^4e^{-21100/T}[C_2H_2]$	$9x10^3e^{-12100/T}A_s[C_2H_2]$	Lee[a] [159]	Fenimore[a] [163]	-

[a] Modified with respect to the original formulation.

get soot production in Diesel combustion applications. The Vishwanathan and Reitz [168] model[11] (highlighted with bold font in Table 2.1) is the two-equation model used in this thesis for the study of soot production (results are presented in Chapter 5). The Gokul model, considers soot inception through pyrene graphitization. The authors highlight the importance of considering PAHs chemistry for soot inception specially in the case of low-temperature combustion where PAHs high-concentration zones appear further downstream of the main ignition zone. Moreover, the use of pyrene ($A4$ with chemical formula $C_{16}H_{10}$) is in line with the current understanding on soot nucleation outlined in Subsection 2.2.2. Thus, the nucleation step follows

$$C_{16}H_{10} \longrightarrow 16C(s) + 5H_2 \tag{2.3.19}$$

with the reaction rate defined as

$$\dot{\omega}_n = 2 \times 10^3 [A_4] \tag{2.3.20}$$

where $[A_4]$ denotes the molar concentration of pyrene.

As for the surface growth step, the definition is the same as that of Equation 2.3.12 although the pre-exponential factor has been increased by a factor of 15, compared to the original Leung model, yielding to

$$\dot{\omega}_g = 9 \times 10^4 e^{-12100/T} \sqrt{A_s} [C_2H_2] \tag{2.3.21}$$

In addition to oxidation through O_2, oxidation through OH is also taken into account. For O_2, the NSC model is used with updated Arrhenius coefficients suggested by Ladommatos et al. [178] giving place to

$$K_A = 30e^{-15800/T} \tag{2.3.22}$$

$$K_B = 8 \times 10^{-3} e^{-7640/T} \tag{2.3.23}$$

$$K_T = 1.51 \times 10^5 e^{-49800/T} \tag{2.3.24}$$

$$K_Z = 27e^{3000/T} \tag{2.3.25}$$

For OH, the reaction step proposed by Fenimore and Jones [163] is used following

[11] From this point the model will be referred to as Gokul model.

$$C(s) + OH \longrightarrow CO + H \tag{2.3.26}$$

with the reaction rate defined as

$$\dot{\omega}_{OH} = 127 \times 10^3 \gamma_{OH} X_{OH} T^{-0.5} A_s \tag{2.3.27}$$

where γ_{OH} and X_{OH} are the OH collision efficiency (set to 0.13) and molar fraction, respectively. In the above expression, the pre-exponential factor has been increased by a factor of 12 with respect to the original formulation by Fenimore and Jones [163].

As in the case of the Leung model, soot number density is considered to increase due to particle inception and to decrease due to agglomeration. The latter step coincides with Equation 2.3.18 while the first one is reformulated according to

$$\dot{\omega}_{n,N_s} = \frac{16 M_s}{M_{nuclei}} \dot{\omega}_n \tag{2.3.28}$$

with M_{nuclei} being the mass of incipient nuclei calculated assuming a uniform nuclei diameter ($d_{nuclei} = 1.28 \times 10^{-9}\ m$) following

$$M_{nuclei} = \frac{\pi \rho_s}{6} d_{nuclei}^3 \tag{2.3.29}$$

Although two-equation models still rely on constants to match experimental results, these type of models provide a more comprehensive description of soot production while maintaining a relatively low-computational cost as only one more transport equation is solved compared to one-equation soot models. In this direction, Tao et al. [179] presented soot results for a heavy-duty CI engine and compared the Hiroyasu-NSC soot model and an eight-step two-equation soot model. Despite the need of fitting constants for both models, the authors reported improved soot distribution results when the eight-step two-equation soot model was used. The improvement in results is attributed by the authors to a better description of soot production physics.

Before proposing the Gokul model, Vishwanathan and Reitz [180] also worked on a comparison study between the Hiroyasu-NSC soot model and a nine-step two-equation soot model for a turbulent n-heptane spray in a constant-volume vessel. Similarly to the observations by Tao et al. [179], the authors found that fitting constants was required for both models to

match the experimental results although the authors reported that no significant changes were needed for the two-equation soot model compared to the Hiroyasu-NSC soot model. Moreover, the authors also reported an insignificant CPU time increase for the two-equation soot model.

Another example of soot models comparison can be found in the review work of Skeen et al. [181]. The review work focuses on soot production in an n-dodecane turbulent spray injected in a quiescent environment. Experimental and modeling contributions from several institutions participating in the ECN were reported. Soot results using the Hiroyasu-NSC, the Leung model, the Gokul model and the two-equation model proposed by Moss et al. [156] were compared. A straightforward comparison between one-equation and two-equation models results was not feasible due to differences in CFD codes and computational setups. Nonetheless, results suggest that simplified models using acetylene (i.e the Hiroyasu-NSC and the Moss et al. [156] model) might not be accurate enough for describing soot spatial distribution hence justifying the need for more comprehensive approaches that might also consider PAHs precursors as also suggested by Vishwanathan and Reitz [168].

2.3.3. Detailed models

As stricter legislation on soot emissions are expected to be introduced, the ability to predict particle size distribution characteristics becomes more attractive. Like two-equation models, most detailed models describe the soot production process in terms of the phenomena outlined in Section 2.2. The main difference resides in its ability to describe the development of the soot particle size distribution function (PSDF) which is not included in two-equation models. The description of the PSDF is achieved by formulating conservation equations for its properties. For this purpose, the *method of moments* and the *sectional method* are among the most commonly used approaches.

The method of moments developed by Frenklach et al. [107, 182] describes the soot production process by assuming the shape of the PSDF and using its statistical moments defined in general terms as

$$M_r = \sum_{i=1}^{\infty} i^r N_i \tag{2.3.30}$$

where M_r is the r^{th} moment of the PSDF and N_i is the number density of soot particles of size class i. Equation 2.3.30 is the most generalized form of the PSDF statistical moments, but it has been shown that it can be extended to a bi-variate formulation based on soot aggregates volume and surface area [183, 184].

The method of moments has been successfully used for the description of the evolving morphology of soot. In this regard, Balthasar and Frenklach [185] reported results for laminar premixed flames in which nucleation was identified as the governing process for particle shape and the transition from coalescent to aggregate growth. Later, Bisetti et al. [186] also studied soot morphology, this time in turbulent non-premixed flames, and found a dependency on the location of soot aggregates in mixture fraction space. In terms of quantitative comparisons to experimental results, some limitations have been reported for the method of moments. An extensive study of laminar premixed and non-premixed flames by Mehta, Haworth and Modest [187] showed mixed results with ratios of computed to measured peak soot volume fraction ranging from 0.00025 to 97. Likewise, Donde et al. [188] reported over-predicted soot volume fraction results for turbulent non-premixed flames attributing the quantitative error to possible errors in the treatment of turbulence, approximations in its interaction with chemistry and uncertainties in soot processes reaction rates. In line with this last observation, Hatzipanagiotou et al. [189] presented a study on the calibration of a soot model based on the method of moments in order to quantitatively reproduce soot measurements from a multi-hole Diesel injector in a constant-pressure combustion vessel. In the engine research field, results show qualitative agreement over a wide range of operating conditions [190–192].

From another perspective, the sectional method describes the PSDF by discretizing the soot particle domain into a finite number of sections each of which represent a particle size. Further, the sectional model can be subdivided into two different approaches, namely aerosol discrete sectional model and chemical discrete sectional model, depending on the way soot particles interactions are treated [193].

The sectional method has been extensively used in many combustion applications. Recently published results for laminar premixed [114, 194], laminar non-premixed [195–198] and turbulent non-premixed [199, 200] flames support its use as a promising tool for detailed soot modeling. For turbulent sprays, Aubagnac-Karkar et al. [201] modeled soot production in a Diesel-like spray finding reasonable good qualitative agreement for

parametric variations of ambient temperature and oxygen concentration. For CI engines, the works by Aubagnac-Karkar et al. [202] and Duvvuri et al. [203] show, as in the case of similar works with the method of moments, good qualitative agreement. In this regard, Ibrahim et al. [204] reported a comparison of soot results from a CI engine using two detailed models, one based on the method of moments and another based on the sectional method. The authors found similar results with a 7% error compared to experimental measurements.

2.4. Summary

Throughout this chapter, the combustion of a Diesel-like spray and the soot production process have been reviewed. The chain of events leading to combustion of a Diesel-like spray is composed of highly non-linear, multi-phase, multi-scale phenomena. Under CI engine relevant conditions, liquid fuel injected into a high-temperature, high-pressure environment undergoes primary breakup forming droplets, secondary breakup forming smaller droplets, vaporization and air entrainment ultimately leading to autoignition. The turbulent reacting spray is then characterized by mixing-controlled diffusion combustion in which soot production is favored. In such a scenario, soot modeling is a challenging task being affected by assumptions and uncertainties not only of its own subprocesses, but also of the underlaying processes aforementioned.

As for soot modeling approaches, the literature review shows that one-equation, two-equation and detailed models cover most applications. One-equation models, although computationally efficient and simple to implement, heavily depend on calibration to match experimental data with results limited to soot quantity variables. Two-equation models introduce an additional conservation equation for soot number density allowing for a more comprehensive description of soot production while maintaining a simple implementation and relatively low-computational cost compared to one-equation soot models. Lastly, detailed models currently offer the most comprehensive description of soot production by including the particle size distribution within its formulation. Nonetheless, this type of models are computationally expensive [104, 193] and although they have been used for CI engine applications its extensive use is still limited.

In this thesis, soot modeling is focused on two-equation models as of today this type of models offer a good compromise between accuracy and computational cost. In particular, the Gokul model is used throughout this work. A detailed description of the thesis modeling approach is given in the next chapter.

CHAPTER 3

Modeling approach

From the phenomenological description in Chapter 2, it is clear that the chain of events leading to soot production in Diesel-like sprays is composed of highly non-linear, multi-phase and multi-scale phenomena. Thus, the thesis modeling approach aims at assessing the different phenomena involved following a strategy of three stages. First, Section 3.1 in this chapter is devoted to the description of the spray model. Second, the approach for handling TCI is described in Section 3.2. Third and last, Section 3.3 deals with the approach for soot modeling.

As stated in Chapter 1, this thesis is framed within the ECN context. Consequently, well-established experiments from this network are used for validation of CFD results. The ECN was launched as a collaborative effort to advance scientific understanding of combustion at engine relevant conditions and to identify priorities for further experimental and computational research [28]. Over the years, experimental contributions from several institutions around the globe have allowed for the development of an extensive archive for several operating conditions. For this thesis, the primary condition from the ECN archive is the Spray A consisting of a single-hole nozzle injecting liquid fuel into a high-temperature, high-pressure quiescent environment with thermodynamic conditions relevant to CI engines that use moderate exhaust gas recirculation (EGR) levels.

Experimental data used for validation have been measured under the same operating conditions at different institutions and are available at the ECN website [28]. Spray tip penetration and liquid length measurements have been carried out at CMT-Motores Térmicos using nozzle 210675 (Spray A) [71, 205] and nozzle 209135 (Spray D) [206]. Spray A mixture fraction and velocity fields were measured at Sandia National Laboratories (SNL) using nozzle 210677 [66] and at IFP Energies nouvelles using nozzle 210678

Table 3.1: *Fuel injection and thermodynamic reference condition.*

Injection conditions	
Fuel	n-dodecane
Nozzle diameter[a]	89.4 μm Spray A
	190.3 μm Spray D
Injection pressure	150 MPa
Fuel temperature	363 K
Thermodynamic conditions	
Ambient temperature	900 K
Ambient density	22.8 kg/m^3
Ambient composition[b]	$X_{O_2} = 0.15$
	$X_{N_2} = 0.85$

[a] Nozzle reference number 210675 and 209135 for Spray A and Spray D, respectively.
[b] For the inert condition $X_{N_2} = 1$.

[207], respectively. Nominal diameters for the three Spray A nozzles are 89.4 μm for nozzle 210675, 83.7 μm for nozzle 210677 and 88.6 μm for nozzle 210678. Table 3.1 summarizes the reference fuel injection and thermodynamic conditions.

3.1. Spray modeling

The thesis spray modeling approach is based on the use of CFD simulations. These are carried out with CONVERGE [208] CFD solver in the framework of the Lagrangian parcel, Eulerian fluid approach to handle the multi-phase nature of the Diesel-like spray. The computational domain consists of a 50 mm radius and 102 mm length cylinder.[1] The mesh grid is comprised of 2 mm cubes and is auto-generated by CONVERGE's cut-cell Cartesian method. Grid mesh resolution is added near the nozzle area using a truncated cone-shaped fixed embedding with a minor radius of 1 mm, a major radius of 5 mm and a length of 10 mm. Further grid mesh resolution is added if needed based on velocity, temperature and fuel mass fraction gradients using CONVERGE's adaptive mesh refinement (AMR) capabilities.

The Lagrangian parcel approach is used for the description of the liquid phase in conjunction with sub-models for droplet atomization, collisions, drag and evaporation. Atomization is accounted for by a modified version of the KH-RT model in which aerodynamic instabilities are responsible for primary breakup while secondary breakup is the result of the competing

[1] The domain is large enough as to prevent spray-wall interaction.

Kelvin-Helmholtz (KH) and Rayleigh-Taylor (RT) mechanisms. Collision of droplets formed through atomization are described with the no time counter (NTC) model and droplet drag is modeled considering variations in drop shape using a distortion parameter. Lastly, the Frossling correlation is used to estimate the droplet radius rate of change due to evaporation [209].

For the Eulerian fluid description, the Favre-averaged Navier-Stokes equations are solved within a RANS framework. The standard $k-\varepsilon$ turbulence model is used with $C_{\varepsilon 1} = 1.55$ to account for round jet correction [210, 211]. This approach for RANS turbulence modeling has been shown to be suitable in Diesel-like spray applications for which the renormalization group (RNG) $k-\varepsilon$, another commonly used turbulence model, is reported to over-estimate the entrainment rate [48, 212]. The pressure implicit with splitting of operators (PISO) method is used to handle the pressure-velocity coupling. The numerical scheme is second-order central with the exception of turbulence solved following a first-order upwind scheme. Lastly, a time-step control based on the maximum number of cells a parcel can travel in a single time-step was used yielding to values in the order of 0.2 μs.

3.2. Turbulence and chemistry interaction

Combustion modeling in this thesis is focused on the comparison of two diametrically opposite assumptions for the sub-grid flame structure. On one hand, CONVERGE's build-in SAGE detailed chemical kinetics solver [213] assuming well-mixed (WM) conditions. On the other hand, the Unsteady Flamelet Progress Variable (UFPV) combustion model [90, 214] based on the flamelet concept.

The following subsections are devoted to the description of the WM and the UFPV combustion models. Nonetheless, it is worth mentioning that the choice of the reaction scheme used to describe the fuel oxidation path is also of particular relevance. In this regard, two well-known chemical mechanisms are used and compared. The baseline scheme is a skeletal mechanism with 54 species and 269 reactions presented by Yao et al. [215].[2] This mechanism describes the oxidation of n-dodecane as a Diesel surrogate and it has been partly tailored to reproduce Spray A experimental results. As the Yao mechanism does not consider PAH chemistry, needed for soot modeling with PAH precursors, the reaction scheme developed by Narayanaswamy et al.

[2]From this point the chemical mechanism proposed by Yao et al. [215] is referred to as the Yao mechanism.

[216][3] is also used. The Narayanaswamy mechanism describes n-dodecane oxidation with 255 species and 2289 reactions accounting for aromatic species including pyrene. Pérez [90] conducted a detailed analysis of the Yao and Narayanaswamy mechanisms. In his study, Pérez compared constant-pressure homogeneous reactor results at the thermodynamic conditions of Spray A. It was found that the Yao mechanism predicts shorter cool flame interval and ignition delay time, an observation that is later reproduced in CFD turbulent spray calculations.

3.2.1. The well-mixed model

CONVERGE build-in SAGE detailed chemical kinetics solver [213] is the WM model used in the following chapters. This WM model solves, at each computational cell and time-step, the net production rate of species k for reaction $i = 1, 2, ..., I$ according to

$$\dot{\omega}_k = \sum_{i=1}^{I} (\nu''_{ki} - \nu'_{ki}) q_i \tag{3.2.1}$$

where ν'_{ki} and ν''_{ki} are the stoichiometric coefficients for reactants and products, respectively, and q_i is the rate of progress variable for the i^{th} reaction.

Then, governing equations for the conservation of mass and energy are solved. The governing equation for mass conservation follows

$$\frac{d[k]}{dt} = \dot{\omega}_k \tag{3.2.2}$$

where $[k]$ denotes the molar concentration of species k and $\dot{\omega}_k$ is evaluated with Equation 3.2.1.

As for the conservation of energy, the governing equation follows

$$\frac{dT}{dt} = \frac{V\frac{dP}{dt} - \sum_k (\overline{h}_k \dot{\omega}_k)}{\sum_k ([k]\overline{c}_{p,k})} \tag{3.2.3}$$

with $\overline{h}_k$ and $\overline{c}_{p,k}$ being the molar specific enthalpy and molar constant-pressure specific heat for a given species k. As pointed out by Senecal et al. [213], the temperature obtained with Equation 3.2.3 is used to update

[3] From this point the chemical mechanism proposed by Narayanaswamy et al. [216] is referred to as the Narayanaswamy mechanism.

the chemical rate coefficients while the temperature of any cell is updated based on species concentration once the detailed chemistry calculation has converged.

It should also be bare in mind that the net production rate of species k is a function of computed temperature and species k mass fraction Y_k. In a RANS framework, this observation implies the introduction of a commutation error due to temporal averaging given that $\widetilde{\dot{\omega}}_k \neq \dot{\omega}_k(\widetilde{Y}_k, \widetilde{T})$. Although this commutation error is expected to be small, its influence is to be considered.

3.2.2. The UFPV model

The Unsteady Flamelet Progress Variable (UFPV) combustion model has been developed at CMT-Motores Térmicos [90, 214] and implemented in CONVERGE CFD code through user defined functions. The UFPV model is formulated under the assumption that a turbulent flame can be described as a set of strained laminar counterflow flamelets [217]. This assumption is relevant in high-Damköhler number flows (as in the case of Diesel-like combustion applications) in which the chemical characteristic time is small compared to the physical characteristic time. In this type of flows, the thin layer where combustion is sustained remains laminar since turbulence cannot modify it locally and instantly [30].

The transient evolution of species mass fraction in a counterflow flamelet in mixture fraction space is solved according to

$$\frac{\partial Y_k}{\partial t} = \frac{\chi}{2}\frac{\partial^2 Y_k}{\partial Z^2} + \dot{\omega}_k \tag{3.2.4}$$

where the net production rate of species k is solved through the ordinary differential equation (ODE) chemical system defined by the chemical mechanism. The scalar dissipation rate (χ) in Equation 3.2.4 accounts for the strength of convective and diffusive processes assuming a steady profile [30] following

$$\chi(a, Z) = \frac{a}{\pi}\exp[-2(\mathrm{erfc}^{-1}(2Z))^2] \tag{3.2.5}$$

where a is the strain rate and erfc^{-1} is the inverse complementary error function.

The prescribed χ profile expression can be normalized by the scalar dissipation rate at stoichiometric conditions (χ_{st}). The normalized profile yields to an expression independent of the strain rate according to

$$\chi(\chi_{st}, Z) = \chi_{st} \frac{F(Z)}{F(Z_{st})} \tag{3.2.6}$$

To solve the set of flamelets describing the turbulent flame, two codes are used in this thesis. LFLAM [218], a code developed at Centro de Investigaciones Energéticas, Medioambientales y Tecnológicas (CIEMAT) and the flamelet code [219] developed at Argonne National Laboratory (ANL) both of which are used throughout Chapter 4 and Chapter 5.

In the framework of the UFPV model, transient laminar flamelet solutions are re-parametrized from a temporal basis to a normalized progress variable (c) basis. The normalized progress variable ranges from 0 in the inert state to 1 in the fully burned state and is defined as

$$c = \frac{Y_c - Y_c^{inert}}{Y_c^{steady} - Y_c^{inert}} \tag{3.2.7}$$

where Y_c is the progress variable, Y_c^{inert} is the progress variable at the inert condition[4] and Y_c^{steady} is the progress variable from the flamelet steady solution. Y_c is defined as a linear combination of key species mass fraction which monotonically increases with time such that a bijective relationship exists [218].

To account for the effect of turbulence, a presumed probability density function (PDF) approach is used for mixture fraction and scalar dissipation rate assuming statistical independence between them [220]. For mixture fraction, a beta function defined by its mean value $\widetilde{Z}$ and its variance $\widetilde{Z''^2}$ is used according to $P_Z(Z; \widetilde{Z}, S)$. In the latter expression, S is a segregation factor calculated as

$$S = \frac{\widetilde{Z''^2}}{\widetilde{Z}(1-\widetilde{Z})} \tag{3.2.8}$$

For the scalar dissipation rate, a log-normal function is used according to $P_\chi(\chi_{st}; \widetilde{\chi}_{st}, \sigma)$, assuming that $\sigma = \sqrt{2}$ [218].

With the PDF approach, any average value $\widetilde{\psi}$ can then be obtained through

[4] In this work the inert condition is the result of adiabatic ideal mixing between fuel and air.

$$\widetilde{\psi}(\widetilde{Z},S,\widetilde{\chi}_{st},\widetilde{t}) = \int_0^{\infty}\int_0^{Z} \psi(Z,\chi_{st},\widetilde{t}) P_Z(Z;\widetilde{Z},S) \, P_\chi(\chi_{st};\widetilde{\chi}_{st},\sigma)\, dZ\, d\chi_{st} \tag{3.2.9}$$

Taking into account the re-parametrization in terms of the normalized progress variable, in the turbulent manifold average values are queried according to $\widetilde{\psi}(\widetilde{Z},S,\widetilde{\chi}_{st},\widetilde{Y}_c)$ with $\widetilde{Y}_c = \widetilde{Y}_c(\widetilde{Z},S,\widetilde{\chi}_{st},\widetilde{c})$.

As for the mean value of χ, it can be obtained through

$$\widetilde{\chi} = \left(\int_0^{\infty} \chi_{st} P_\chi(\chi_{st};\widetilde{\chi}_{st},\sigma)\, d\chi_{st}\right)\left(\frac{1}{F(Z_{st})}\int_0^{Z} F(Z) P_Z(Z;\widetilde{Z},S)\, dZ\right) = \widetilde{\chi}_{st} J(\widetilde{Z},S) \tag{3.2.10}$$

where J (only dependent on $\widetilde{Z}$ and S) relates $\widetilde{\chi}_{st}$ and $\widetilde{\chi}$ retrieved from the CFD calculation using

$$\widetilde{\chi} = C_\chi \frac{\varepsilon}{k}\widetilde{Z''^2} \tag{3.2.11}$$

Ultimately, the manifold is composed of lookup tables discretized with 41 points for $\widetilde{Z}$, 17 points for S, 27 points for $\widetilde{\chi}_{st}$ and 51 points for $\widetilde{c}$. The coupling of the manifold within the CFD code is accomplished through the chemical source term for the species transport equation calculated as

$$\dot{\widetilde{\omega}}_k = \frac{\widetilde{Y}_k^{tab}(\widetilde{Z},S,\widetilde{\chi}_{st},\widetilde{Y}_c(t+\Delta t)) - \widetilde{Y}_k^{cell}(t)}{\Delta t} \tag{3.2.12}$$

where Δt is the CFD simulation time-step, $\widetilde{Y}_k^{cell}$ is the species mass fraction in the cell and $\widetilde{Y}_k^{tab}$ is the species mass fraction tabulated in the manifold in the subsequent time-step for which $\widetilde{Y}_c(t+\Delta t)$ is calculated as

$$\widetilde{Y}_c(t+\Delta t) = \widetilde{Y}_c(t) + \dot{\widetilde{\omega}}_{Y_c}(\widetilde{Z},S,\widetilde{\chi}_{st},\widetilde{Y}_c(t))\Delta t \tag{3.2.13}$$

Chemistry progresses in time following Equation 3.2.13 where $\widetilde{Y}_c(t)$ is calculated based on CFD species concentration and $\dot{\widetilde{\omega}}_{Y_c}$ (generic nomenclature for $\partial\widetilde{Y}_c/\partial t$) is retrieved from the manifold.

As a final remark on the coupling of the manifold within the CFD code, it is worth mentioning that not all species included in the chemical mechanism are transported. In fact, only 12 species are transported (these are $C_{12}H_{26}$, C_2H_2, CH_2O, CO, CO_2, H, H_2O, O, O_2, OH, $A4$[5] and $A4R5$) while some sink species are used to account for the atomic element mass of the not-transported species. In this work, C_7H_{14}, H_2 and $O_{2_{virt}}$ [6] are used as sink species for carbon, hydrogen and oxygen, respectively.

With the outline of the UFPV model presented, it is now relevant to discuss the progress variable definition. The baseline definition used in this work is a linear combination of combustion's major species according to

$$Y_{c_{baseline}} = 0.75 \times CO + CO_2 + H_2O \tag{3.2.14}$$

The choice of species is based on the extended definition $Y_c = CO+CO_2$ [90, 169, 214, 221]. The addition of H_2O and the weighting factor for CO were introduced to ensure that Y_c increases monotonically with time. In addition to the baseline definition, a dedicated progress variable has been used for soot modeling. This dedicated progress variable was defined to account for slower species relevant to soot production. In order to add resolution for PAH chemistry, the progress variable dedicated to soot modeling is calculated as

$$Y_{c_s} = 0.75 \times CO + CO_2 + H_2O + 650 \times A4R5 \tag{3.2.15}$$

The choice of Cyclopenta[cd]pyrene ($A4R5$) for the progress variable is supported on its similarity to the temporal evolution of $A4$ in mixture fraction space. Fig. 3.1 shows the evolution of $A4$ and $A4R5$ for the Spray A reference condition. Despite quantitative differences, both species qualitatively agree with similar onset times and peak value locations at rich mixtures.

The weighting factor for $A4R5$ was set to ensure enhanced resolution for high Y_c values where PAH chemistry is relevant while maintaining resolution for moderate and low values of Y_c which are more relevant to autoignition and main combustion, respectively. The change in Y_c resolution is assessed through a so-called combustion ratio (CR) calculated as

$$CR = 100\frac{(Y_{c_s})_{max}}{(Y_{c_s})_{threshold}} \tag{3.2.16}$$

where $(Y_{c_s})_{max}$ and $(Y_{c_s})_{threshold}$ denote the maximum Y_{c_s} value and its value at a given threshold, respectively.

[5] $A4$ is the soot precursor species for the Gokul model.

[6] $O_{2_{virt}}$ is an artificial species assumed to have the same thermo-physical properties of O_2.

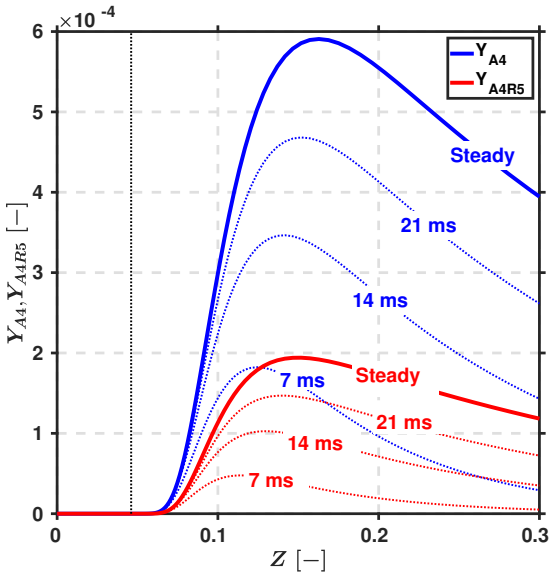

Figure 3.1: *A4 and A4R5 temporal evolution for the reference Spray A condition with $\chi_{st} = 0.4662\ 1/s$ using the Narayanaswamy mechanism. The steady solution is plotted with a solid line while the unsteady solution is plotted with dotted lines. Vertical dotted line is plotted at Z_{st}.*

An schematic of the method used to estimate CR is presented in Fig. 3.2 for an arbitrary mixture fraction. Dashed horizontal lines mark the maximum and threshold levels for Y_{c_s}. The threshold level is the inflection point at which $Y_{c_{baseline}}$ and Y_{c_s} are no longer equal and is defined as the first point to meet $(Y_{c_s}/Y_{c_{baseline}}) < 0.005 \times (Y_{c_s}/Y_{c_{baseline}})_{max}$.

The computed combustion ratio for the Spray A reference condition is shown in Fig. 3.3 for several stoichiometric scalar dissipation rate levels. For lean and slightly rich mixtures (left and right of the stoichiometric mixture fraction plotted with a vertical dotted line) the CR remains at a value of 100% as no *A4R5* is present thus $Y_{c_s} = Y_{c_{baseline}}$. At richer mixtures, more relevant to soot production, the CR starts to decrease with the increase of *A4R5*. At its lowest level, CR is greater than 45%. This value leads to the conclusion that with the proposed definition for Y_{c_s} at least 45% percent of its resolution is devoted to Y_c values relevant to autoignition while the rest is devoted to values relevant to soot production.

To further analyze the importance of the progress variable definition, Fig. 3.4 shows acetylene and pyrene profiles at rich mixtures namely, $Z = 0.10$ and $Z = 0.12$. Solid lines are used to plot species profiles with $Y_{c_{baseline}}$ while dotted lines are used with Y_{c_s}. Both, acetylene and pyrene profiles,

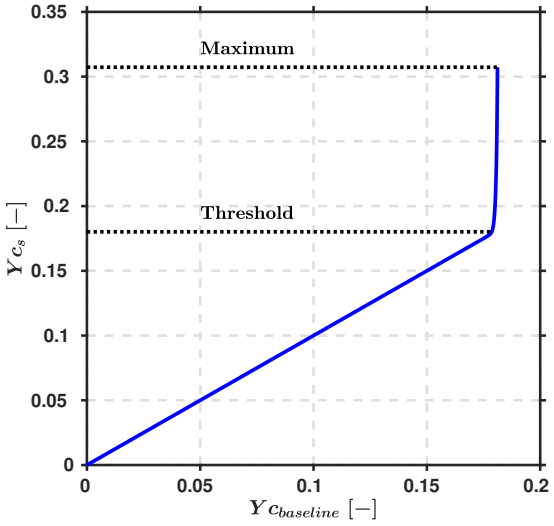

Figure 3.2: *Comparison of progress variable definitions at an arbitrary mixture fraction.*

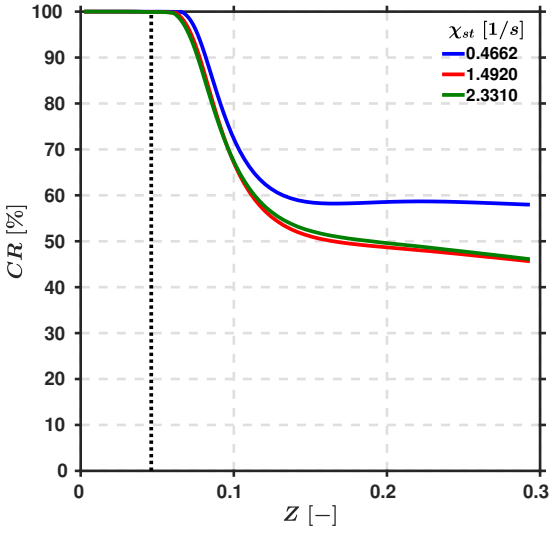

Figure 3.3: *Combustion ratio for different levels of scalar dissipation rate for the Spray A reference condition. A vertical dotted line is plotted at the stoichiometric mixture fraction.*

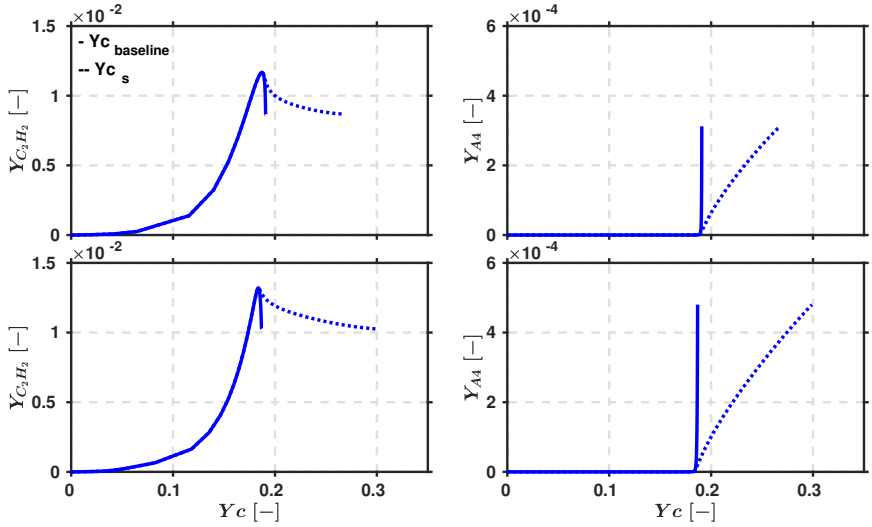

Figure 3.4: *C_2H_2 and A4 profiles for $Z = 0.10$ (top row) and $Z = 0.12$ (bottom row) for the reference Spray A condition with $\chi_{st} = 0.4662\ 1/s$ using the Narayanaswamy mechanism. Solid line for the baseline progress variable and dotted line for the soot progress variable.*

show abrupt changes close to $Y_c = 0.2$ which is not a desirable feature since it promotes interpolation errors. On the other hand, Y_{c_s} shows smoother profiles due to the enhanced resolution at high Y_c values.

Finally, at this point it is worth mentioning that in this thesis a variant of the UFPV model is assessed. This variant is introduced under the name of UFPV-0 model and it aims at isolating effects to evaluate the influence of the sub-grid flame structure assumption on the autoignition sequence and combustion global parameters. As logically expected, the UFPV-0 model shares most of the features from the UFPV model with the exception of the PDF approach. The UFPV-0 manifold comprises the laminar flamelet solutions thus facilitating the comparison between the WM and the flamelet sub-grid flame structure assumption for which results are presented in the next chapter.

3.3. Soot modeling

As outlined in Chapter 1, the soot modeling approach if focused on a two-equation soot model. In Chapter 2, the Gokul model was introduced as the model used for the study of soot production. The reader should bare in mind that, as previously mentioned in Subsection 2.3.2, the Gokul model

is an extension of the widely used Leung model for which, among other changes, the surface growth pre-exponential factor was fitted to target soot experimental data under a RANS framework using a one-way coupling[7] with a WM model. In Chapter 5, results for a preliminary assessment (in Section 5.1) of the Gokul model evidences the need for the readjustment of soot subprocesses constants when using a two-way coupling with the UFPV model.

From the literature review on two-equation soot models (a summary is reported in Table 2.1) it was seen that fitting of the surface growth pre-exponential factor is a generalized way to target experimental data. Consequently, in this work a similar approach is followed based on this observation. To target soot volume fraction at quasi-steady state, the soot surface growth pre-exponential factor is fitted to 15×10^3. The proposed factor lays between the value used in the Leung model (2.5 times higher) and the Gokul model (6 times lower).

In addition to the change in the surface growth step, the OH oxidation rate factor was set to 106 [164]. This change is also supported by results for the preliminary assessment of the model that are discussed in Section 5.1. The 106 factor is one order of magnitude lower than that in the Gokul model which was increased by a factor of 12 compared to the original factor proposed by Fenimore and Jones [163]. Lastly, an oxidation step through O was introduced although OH and O_2 remain the major species contributing to soot oxidation as reported by Frenklach et al. [133]. The O oxidation step is based on the work by Guo, Liu and Smallwood [164] following

$$C(s) + O \longrightarrow CO \tag{3.3.1}$$

with the reaction rate defined as

$$\dot{\omega}_O = 55.4 \gamma_O X_O T^{-0.5} A_s \tag{3.3.2}$$

where the atomic oxygen collision efficient constant (γ_O) is set to 0.5 [164].

3.4. TCI and soot modeling

In this section, the handling of TCI and soot modeling is discussed. The terms *one-way coupling* and *two-way coupling* refer to whether or not soot production affects the spray gas phase. With the *one-way coupling*, soot production does not affect the spray gas phase and, in consequence, the

[7] There's no interaction between the gas phase and soot production.

production of soot does not change species concentration, temperature, heat release rate or any other gas phase variable. In this work, the well-mixed model is run with a one-way coupling. Transport equations for soot mass fraction and soot number density are solved using mean temperature and species concentrations at CFD runtime using

$$\dot{\omega}_{Y_s} = (16\dot{\omega}_n + 2\dot{\omega}_g - \dot{\omega}_{O_2} - \dot{\omega}_{OH})M_s \tag{3.4.1}$$

for the soot mass fraction source term while the soot number density source term follows the expression

$$\dot{\omega}_{N_s} = \dot{\omega}_{n,N_s} - \dot{\omega}_{agg} \tag{3.4.2}$$

where $\dot{\omega}_{n,N_s}$ and $\dot{\omega}_{agg}$ are calculated according to Equation 2.3.28 and Equation 2.3.18.

For the *two-way coupling*, soot production and the spray gas phase interact with each other. This coupling is achieved by incorporating the calculation of soot reaction rates within the flamelet framework. Two additional transport equations are solved for the set of laminar strained flamelets namely, soot mass fraction and soot number density according to

$$\begin{aligned}\rho\frac{\partial Y_s}{\partial t} = &-\frac{1}{4}\left(\frac{\partial \rho\chi}{\partial Z} + \frac{\chi}{D}\frac{\partial}{\partial Z}(\rho D)\right)\frac{\partial Y_s}{\partial Z} \\ &-\sqrt{\frac{\chi}{2D}}\frac{\partial}{\partial Z}(\rho Y_s V_s) + \dot{\omega}_{Y_s}\end{aligned} \tag{3.4.3}$$

and

$$\begin{aligned}\rho\frac{\partial \widehat{N_s}}{\partial t} = &-\left[\frac{1}{4}\left(\frac{\partial \rho\chi}{\partial Z} + \frac{\chi}{D}\frac{\partial}{\partial Z}(\rho D)\right) + \frac{\chi}{2D}\rho V_s\right]\frac{\partial \widehat{N_s}}{\partial Z} \\ &+\left(e^{-\widehat{N_s}} - 1\right)\sqrt{\frac{\chi}{2D}}\frac{\partial}{\partial Z}(\rho V_s) + e^{-\widehat{N_s}}\dot{\omega}_{N_s}\end{aligned} \tag{3.4.4}$$

where D accounts for diffusivity in mixture fraction space, $\widehat{N_s} = ln(N_s + 1)$ is a change of variable needed due to numerical reasons [97] and V_s is the thermophoretic velocity term calculated as

$$V_s = -\frac{1}{2}\frac{\mu}{\rho T}\sqrt{\frac{\chi}{2D}}\frac{\partial T}{\partial Z} \tag{3.4.5}$$

where μ is the dynamic viscosity.

Equation 3.4.3 and Equation 3.4.4 have been derived assuming infinity for the Lewis number thus neglecting molecular diffusion in comparison to thermophoretic forces [97]. The two-way coupling between the soot and gas phase introduces a change in the calculation of the chemical source term in Equation 3.2.4 such that $\dot{\omega}_k = \dot{\omega}_k^{\text{gas}} + \dot{\omega}_k^{s}$ with superscripts "gas" and "s" denoting the gas phase and soot, respectively.

A full schematic of the two-way coupling within the UFPV model framework is shown in Figure 3.5. A set of laminar strained flamaletes are solved both for the steady and unsteady states. The introduction of the progress variable allows for the re-parametrization of the solution to describe the progress of combustion from the initial inert to the fully burned state. By presumed PDF integration, TCI is accounted for and a flamelet manifold is generated. The flamelet manifold contains key mean species mass fraction ($\widetilde{Y}_k$) and the mean progress variable source term ($\widetilde{\dot{\omega}}_{Y_c}$) and can be query based on mean mixture fraction ($\widetilde{Z}$), segregation factor (S), mean stoichiometric scalar dissipation rate ($\widetilde{\chi}_{st}$) and mean progress variable ($\widetilde{Y}_c$). The tabulated flamelet solutions are coupled with the CFD solver through the chemical source term for the species transport equation ($\widetilde{\dot{\omega}}_k$) evaluated with Equation 3.2.12.

Under this approach, soot reaction rates calculated for the laminar strained flamelets are also handled with the presumed PDF integration scheme to account for TCI. Besides tabulated values for $\widetilde{\dot{\omega}}_{Y_c}$ and $\widetilde{Y}_k$, the flamelet manifold includes mean reaction rates for nucleation ($\widetilde{\dot{\omega}}_n$), surface growth ($\widetilde{\dot{\omega}}_g^*$) and oxidation through O_2 ($\widetilde{\dot{\omega}}_{O_2}^*$), OH ($\widetilde{\dot{\omega}}_{OH}^*$) and O ($\widetilde{\dot{\omega}}_O^*$). The asterisk superscript denotes soot surface area specific reaction rates i.e. $\widetilde{\dot{\omega}}_g^* = \dot{\omega}_g / \sqrt{A_s}$, $\widetilde{\dot{\omega}}_{O_2}^* = \dot{\omega}_{O_2}/A_s$, $\widetilde{\dot{\omega}}_{OH}^* = \dot{\omega}_{OH}/A_s$ and $\widetilde{\dot{\omega}}_O^* = \dot{\omega}_O/A_s$. Tabulating soot surface area specific reaction rates prevents unphysical soot diffusion in mixture fraction space [97]. With the two-way coupling, the tabulated soot reaction rates are used to calculate soot mass fraction and soot number density source terms ($\dot{\omega}_{Y_s}$ in Equation 3.4.3 and $\dot{\omega}_{N_s}$ in Equation 3.4.4) that are passed to the CFD solver in order to solve the corresponding transport equations. The soot mass fraction source term is calculated according to

$$\widetilde{\dot{\omega}}_{Y_s} = [16\widetilde{\dot{\omega}}_n + 2\widetilde{\dot{\omega}}_g^* \sqrt{A_s} - (\widetilde{\dot{\omega}}_{O_2}^* + \widetilde{\dot{\omega}}_{OH}^* + \widetilde{\dot{\omega}}_O^*)A_s]M_s \tag{3.4.6}$$

As for the soot number density source term, it follows the expression

$$\widetilde{\dot{\omega}}_{N_s} = \widetilde{\dot{\omega}}_{n,N_s} - \widetilde{\dot{\omega}}_{agg} \tag{3.4.7}$$

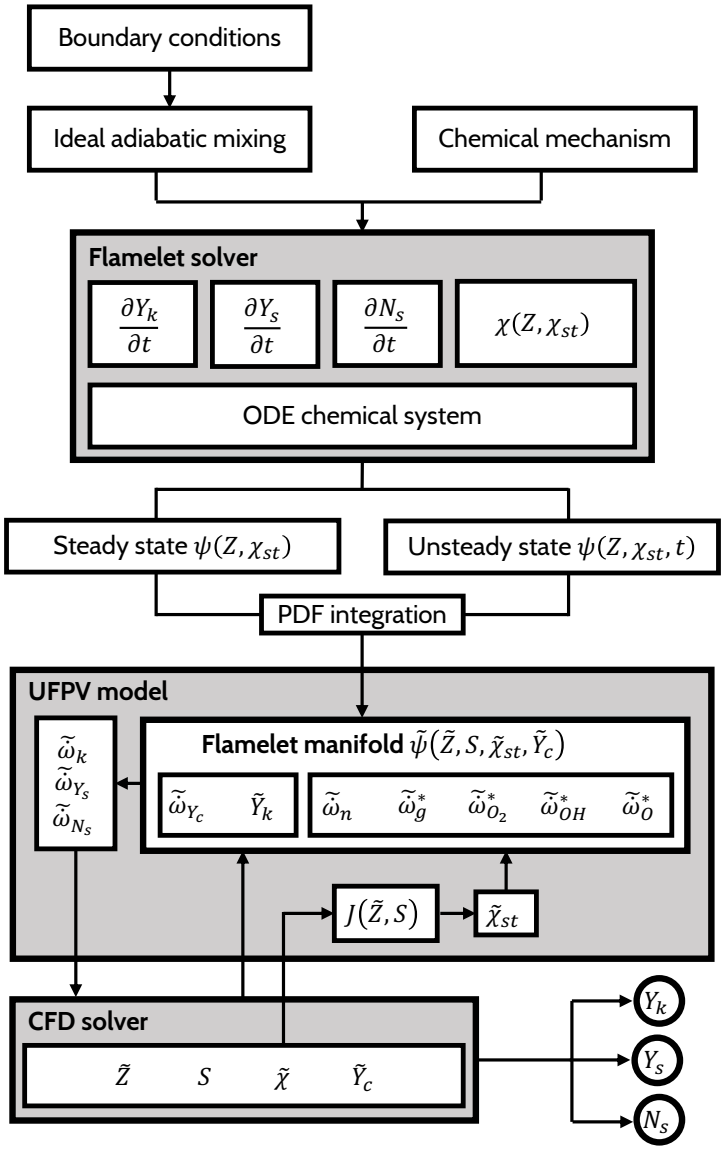

Figure 3.5: *TCI and soot modeling with the two-way coupling within the UFPV model framework.*

where, as with the one-way coupling, $\tilde{\dot{\omega}}_{n,N_s}$ and $\tilde{\dot{\omega}}_{agg}$ are calculated according to Equation 2.3.28 and Equation 2.3.18.

In Equation 3.4.6 and Equation 2.3.18 the variables A_s, T, ρ, Y_s and N_s are retrieved from the CFD solver.

3.5. Summary

In this chapter, a complete overview of the thesis modeling approach has been outlined. With the Diesel-like spray being the main target, spray modeling in this work follows the Lagrangian parcel, Eulerian fluid approach. In relation to combustion modeling, the interaction of turbulence and chemistry is at the core of the thesis modeling approach. In this regard, a detailed chemistry solver under the assumption of a well-mixed sub-grid flame structure and an advanced flamelet-based combustion model are chosen for the study of TCI. The chemical mechanisms used are those proposed by Yao et al. [215] and Narayanaswamy et al. [216]. As for soot modeling, the Gokul model and consequent modifications to the default soot surface growth pre-exponential factor and oxidation steps were described since this two-equation soot model is used for the subsequent study of soot production.

Finally, close attention was paid to the interaction between soot and the gas phase. One-way and two-way couplings were described. The first one is used with the WM model where soot production does not interact with the gas phase. On the contrary, the two-way coupling used with the UFPV model includes soot modeling at the flamelet level where the gas phase is modified by the production of soot. Results obtained under the modeling approach outlined in this chapter are presented in the next two chapters.

CHAPTER 4

Spray combustion

The modeling approach outlined in Chapter 3 is used in this chapter to model spray combustion. With soot being at the end of a long chain of highly complex phenomena, evidenced from the description in Chapter 2, combustion modeling is crucial to lay the groundwork upon which soot production will be later studied. The reference condition for the ECN Spray A and Spray D is the target condition to validate numerical results. The analysis of combustion modeling is not limited to differences between modeling approaches but the effect of the nozzle orifice diameter on autoignition and flame structure is throughly studied as well. For the description of fuel oxidation the Yao and the Narayanaswamy mechanisms are used. The latter is particularly relevant for soot production as it accounts for PAHs chemistry.

The chapter starts with the validation of the modeling approach under inert conditions. Then, CFD results are validated for global combustion parameters before focusing the analysis on the assessment of sub-grid flame structure assumptions and TCI approaches. Results from the WM model and the UFPV model, described in the previous chapter, are presented along a comprehensive analysis of the spray autoignition sequence and flame structure at quasi-steady state.

Flamelet calculation results used within the UFPV model framework in this chapter were obtained using the LFLAM code [218] developed at Centro de Investigaciones Energéticas, Medioambientales y Tecnológicas (CIEMAT) and the flamelet code developed at ANL [219].

Results presented in this chapter have been partly published in the following paper:

- *A numerical study of the effect of nozzle diameter on diesel combustion ignition and flame stabilization* [222].

4.1. Inert spray validation

In this section, the comparison of experimental and CFD results for the reference inert condition is presented (a summary of injection and thermodynamic conditions can be found in Table 3.1). The same computational setup has been used for the Spray A and the larger Spray D except for the smallest cell size reached through AMR which is 125 μm for Spray A and 250 μm for Spray D. Grid convergence results are reported in Appendix 4.5.

For the validation of global quantities, and following ECN guidelines, the spray tip penetration is defined as the axial distance to the furthest location where the mixture fraction (Z) reaches a value of 0.001 while the liquid length is retrieved at the axial position encompassing 97% of the liquid mass. In Fig. 4.1, experimental measurements are plotted in black with a gray area delimiting the 95% confidence interval while CFD results for spray tip penetration and liquid length are plotted in blue for Spray A and green for Spray D. Despite a slower penetration rate during the first 0.5 *ms* for the larger nozzle, an overall excellent agreement for both spray tip penetration and liquid length is achieved with no need for recalibrating any model constant.

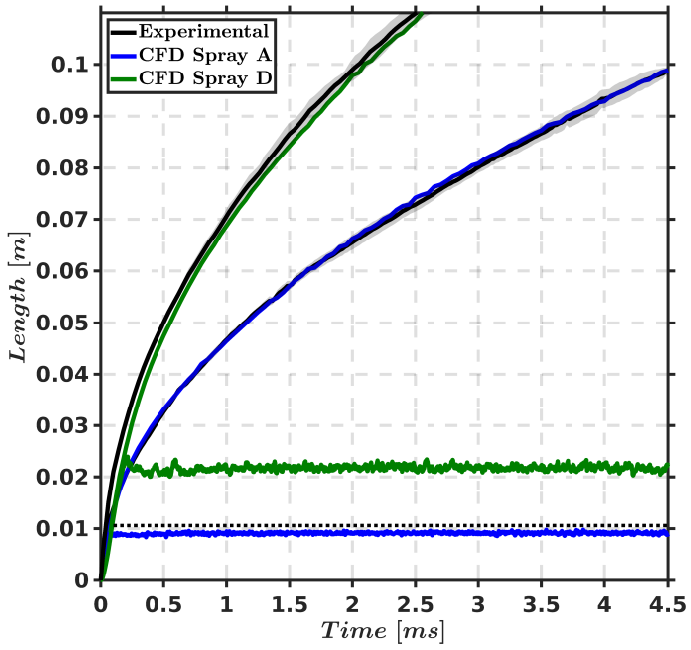

Figure 4.1: *Spray tip penetration and liquid length for the reference Spray A and Spray D under inert conditions.*

As for local quantities validation, spatial coordinates are normalized by the nozzle equivalent diameter ($x^* = x/d_{eq}$) to account for differences in the nominal diameter of the simulated nozzle and the nozzles used for experimental measurements reported in the previous chapter. The nozzle equivalent diameter is calculated according to

$$d_{eq} = d_0(\rho_{fuel}/\rho_a)^{0.5} \tag{4.1.1}$$

where d_0 is the nozzle effective diameter, ρ_{fuel} is the fuel density and ρ_a is the air density.

Fig. 4.2 shows mixture fraction, mixture fraction root mean square (Z_{rms}) and axial velocity in the spray axis at quasi-steady state for the Spray A.[1] The left-hand panel shows how the model successfully predicts Z and Z_{rms} within the 95% confident interval of the experimental measurement. Likewise, the model is also successful in matching the experimental measurement for axial velocity. Some level of disagreement is expected for $x^* < 60$ since the limit of the laser sheet used in the particle image velocimetry (PIV) experiments is located in this region thus increasing experimental uncertainty [207].

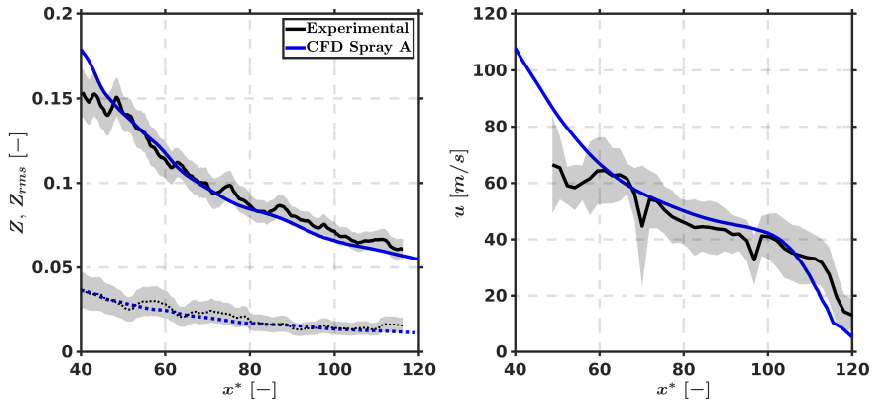

Figure 4.2: *Mixture fraction (solid line) and mixture fraction rms (dotted line) at 5 ms and axial velocity at 1.5 ms along spray axis for inert Spray A.*

Further validation of the mixing field is presented in Fig. 4.3. The upper part of the figure shows mixture fraction radial profiles at two different axial locations. Although CFD results are in excellent agreement at the spray axis, the radial profiles reveal a mixture fraction distribution slightly narrower compared to the experimental data. Similarly, the middle panels

[1] Validation is limited to Spray A results since no experimental data is currently available for Spray D.

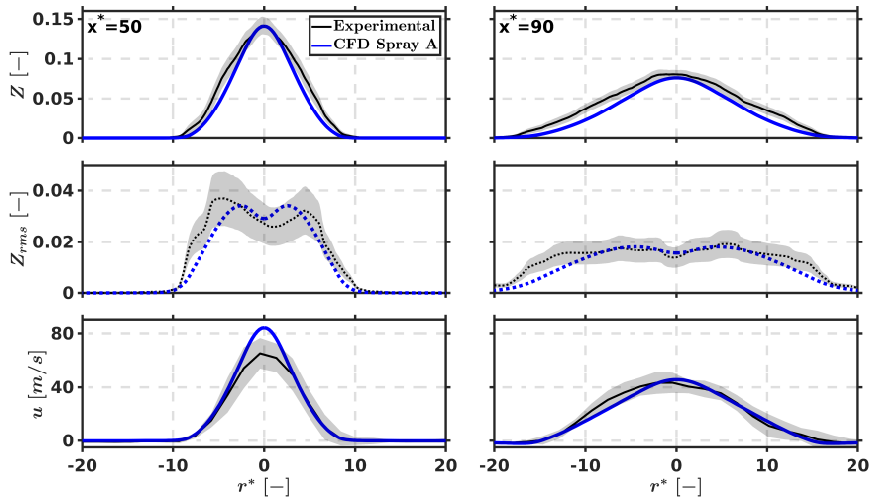

Figure 4.3: *Mixture fraction (top), mixture fraction rms (middle) and axial velocity (bottom) radial profiles at 5 ms for inert Spray A.*

of the figure show mixture fraction rms radial profiles at the same axial locations which, as might be expected from the previous observation, are slightly narrower than the experimental profiles. Lastly, axial velocity radial profiles (bottom panels of the figure) show improved agreement for the radial width in comparison to mixture fraction results. In general terms, the agreement with experimental data is satisfactory with predicted values for Z, Z_{rms} and u close or within the 95% confident interval of the experimental measurement.

4.2. Global combustion parameters

Target conditions correspond to those of ECN Spray A and Spray D with reference fuel injection and thermodynamic conditions summarized in Table 3.1. To assess the sensitivity of combustion global parameters to ambient temperature, Fig. 4.4 shows differences in predicted CFD values compared to experimental results depicted with black squares (vertical lines on top mark the standard deviation of the measurement) for the Spray A. On the experimental side, ID and LOL data is the result of analyzing schlieren and OH^* chemiluminescence images, respectively. Experiments were conducted in a constant pressure vessel at CMT-Motores Térmicos using nozzle 210675 [223] with the exception of the 1000 K case for which measurements were carried out in a constant volume vessel at SNL using nozzle 210370 [28].

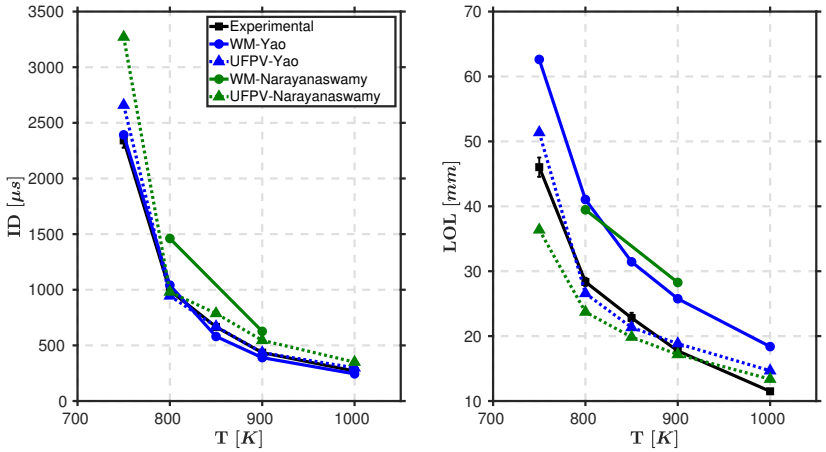

Figure 4.4: *Ignition delay (left) and lift-off length (right) for the Spray A at different ambient temperature conditions.*

On the CFD side, ID and LOL results are obtained following ECN guidelines. ID is defined as the time from the start of injection at which dT_{max}/dt is maximum, with T_{max} being the maximum temperature in the domain. For LOL, the definition is based on OH mass fraction. At each time after the start of combustion, LOL is marked at the closest position to the nozzle to reach 14% of the maximum OH mass fraction. Then, an average value is obtained once the LOL has stabilized.[2] An overall good agreement in terms of ID is seen for the Yao mechanism (results in blue) using both the WM and UFPV models. On the other hand, Narayanaswamy mechanism results show less agreement with experimental data for either combustion model. As for LOL, the combustion model used, or in other words the sub-grid flame assumption used, seems to be more relevant compared to the chemical mechanism choice. In general terms, both combustion models reproduce the trend i.e. shorter LOL with the increase in ambient temperature although the UFPV model predicts a flame stabilized closer to the position reported in the experiments with the exception of the lowest temperature case.

In addition to the study of different ambient temperature conditions, Fig. 4.5 shows results for the reference Spray A condition and the larger Spray D nozzle since these two are the main subject of study in the following section in this chapter. Similarly to previous observations made for Fig. 4.4, Yao mechanism results exhibit a better fit to experimental data

[2]For the 750 K cases the LOL has not yet been stabilized by the end of injection. For these cases, the LOL corresponds to the value at the end of injection.

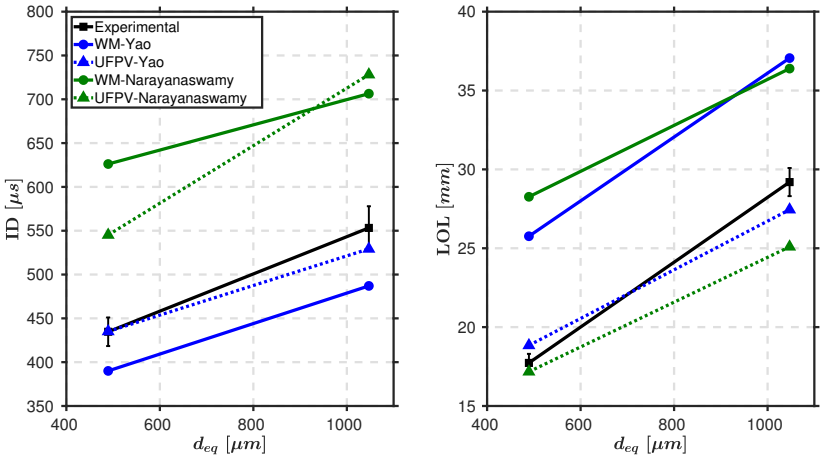

Figure 4.5: *Ignition delay (left) and lift-off length (right) for the Spray A and Spray D reference condition.*

for both combustion models with slightly improved results for the UFPV model while the Narayanaswamy mechanism over-predicts ID for either combustion model and nozzle. As in the case for the Spray A temperature sweep results, the WM and UFPV models reproduce the experimental trend with longer LOL with the increase in nozzle diameter. Observed differences are further discussed in a more detailed analysis of ID and LOL in relation to the autoignition sequence and steady flame structure in Section 4.3 and Section 4.4.

The dynamics of the reacting spray are validated in terms of the spray tip penetration. Fig. 4.6 compares results for Spray A and Spray D. As in the validation for the inert setup, the spray tip penetration is defined as the axial distance from the nozzle where Z reaches a value of 0.001. The experimental result is plotted with a black solid line with a gray shadow to indicate the measurement uncertainty. Excellent agreement between CFD and experimental results is observed for Spray A; meanwhile, for Spray D, a slight over-prediction is observed for both combustion modeling approaches and chemical mechanisms, while the agreement is better for the UFPV model. Differences between predictions and experimental results are linked to the differences in ID observed in Fig. 4.5, which triggers an acceleration of the flow [224]. Aside from spray dynamics, the spray tip penetration is also commonly used as an indicator of the mixing process. Among nozzles, Spray A is expected to be characterized by a faster mixing process compared to the larger Spray D nozzle.

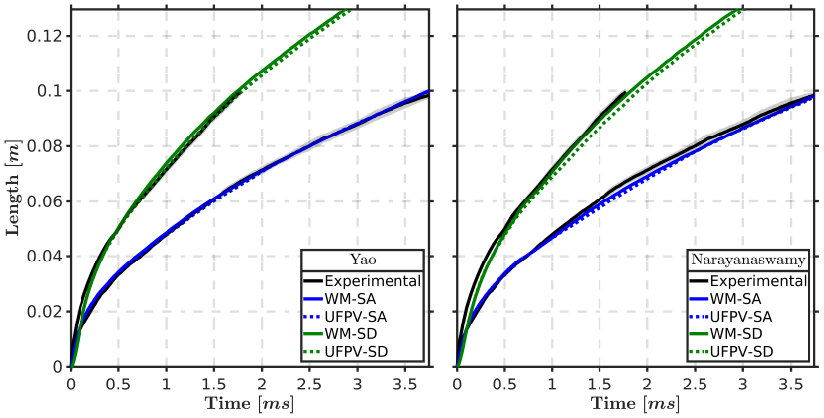

Figure 4.6: *Spray tip penetration for the reacting Spray A and Spray D using the Yao (left) and the Narayanaswamy (right) chemical mechanisms.*

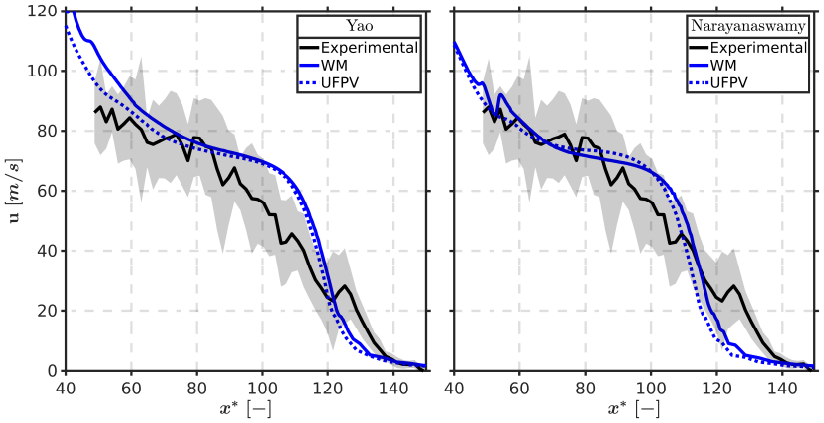

Figure 4.7: *Axial velocity along spray axis at 1.5 ms for the reacting Spray A using the Yao (left) and the Narayanaswamy (right) chemical mechanisms.*

In addition to ID, LOL and spray tip penetration, the computational setup is also validated for axial velocity with available PIV measurements for Spray A at 1.5 *ms*. Fig. 4.7 compares results for this variable along the spray axis which has been normalized by the equivalent diameter such that $x^* = x/d_{eq}$. It is shown that both combustion models and chemical mechanisms predict similar results that match well with the experimental data consistent with the good agreement observed for the spray tip penetration in Fig. 4.6.

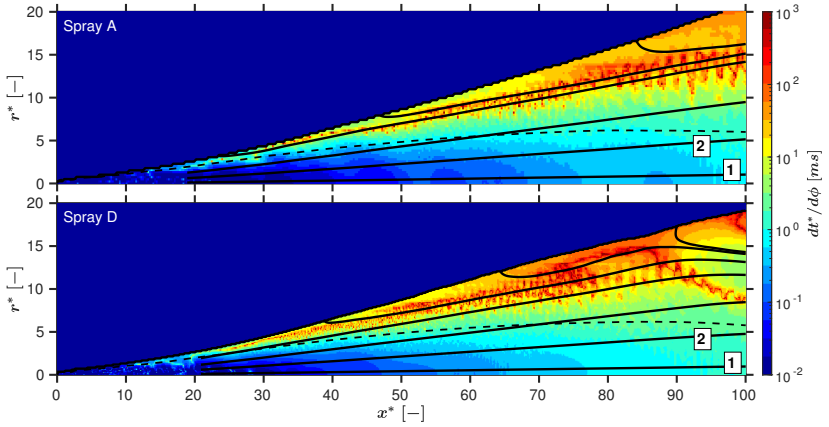

Figure 4.8: *Local residence time for the insert Spray A (top) and Spray D (bottom). Spray spatial coordinates normalized by* d_{eq}.

To provide an additional indicator of the mixing process, a local residence time has been defined based on mixing trajectories (a full description is presented in Appendix 4.5) as the time spent per unit of equivalence ratio (ϕ). Fig. 4.8 shows the local residence time for both Spray A and Spray D under inert conditions. The definition of the residence time in terms of the change of equivalence ratio enables a direct comparison between both nozzle orifices. The analysis of local residence time is then made at 4 *ms*, time at which the spray is already at quasi-steady state. A sample of mixing trajectories (solid lines) and the iso-contour for $\phi = 1$ (dashed line) is also shown. For visualization purposes, the color map is adjusted to logarithmic scale. It can be observed how the structure is similar for both sprays, with increasing values of residence time along any trajectory when moving downstream from the orifice. Among trajectories at the same axial normalized coordinate (consequently at a similar equivalence ratio), there is also an increase of $dt^*/d\phi$ with a local maximum near the spray radius. In summary, the residence time for a given equivalence ratio grows when moving away from the orifice both in axial and radial direction.

Due to the fact that the mixture fraction (hence equivalence ratio) is a conserved scalar, one can state that the convective plus diffusive flow of this variable remains constant between two mixing trajectories and develops with an almost constant angle compared to the axis. By integrating both the mixing trajectories and the residence time concepts, the mixing field created by the spray can be viewed as a set of mixers starting close to the nozzle, which then move away from it, entraining air and spending more

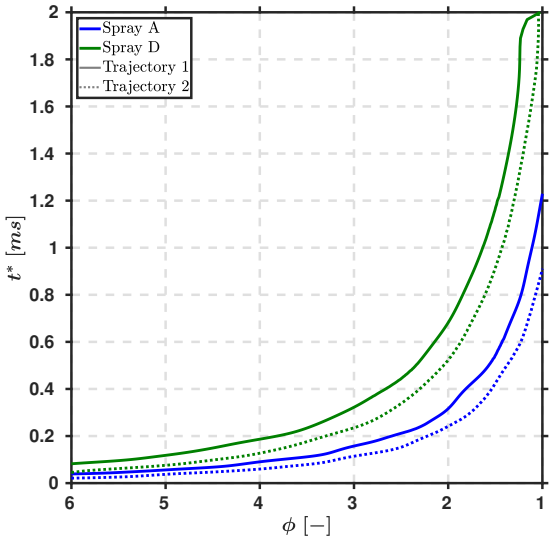

Figure 4.9: *Local residence time for the insert Spray A and Spray D integrated along reference mixing trajectories.*

time on a given equivalence ratio as farther locations are reached. In fact, results in Fig. 4.9 are in line with the latter observation. It is seen that for the reference mixing trajectories[3] any "gas particle" would follow a slower path as it moves along mixing trajectory 1 (closest to the axis) compared to the radially displaced mixing trajectory 2, an observation that holds for both Spray A and Spray D.

To enable further comparison between both nozzles, the upper part of Fig. 4.10 shows spray radius with a solid line and iso-contours of $\phi = 1$ (dashed line) and $\phi = 2$ (dotted line). It is then verified that the normalization of spatial coordinates of the two different nozzles by d_{eq} results in the same value of ϕ for a given set of (x^*, y^*). In addition, if $dt^*/d\phi$ is studied along the reference iso-contours of ϕ (second panel of the figure), it is then verified that this parameter increases with axial distance, in agreement to the contours shown in Fig. 4.8. This confirms that along the spray axis reaching a given equivalence ratio takes longer than along a radially displaced mixing trajectory. Furthermore, for the same value of ϕ the Spray A is characterized by shorter local residence time (thus faster mixing) compared to Spray D. Going back to the previous description of the spray as a set of mixers defined by mixing trajectories leaning out while moving away from the nozzle, the

[3]Mixing trajectory 1 and 2 originate at 5% and 25% of the spray width at 70% of the spray tip penetration.

time spent on a given equivalence ratio will always be longer for the larger nozzle by a factor of around 2, that is, approximately equal to the nozzle orifice increase as can be seen in Fig. 4.9. This has an effect on combustion development, as the following sections will prove.

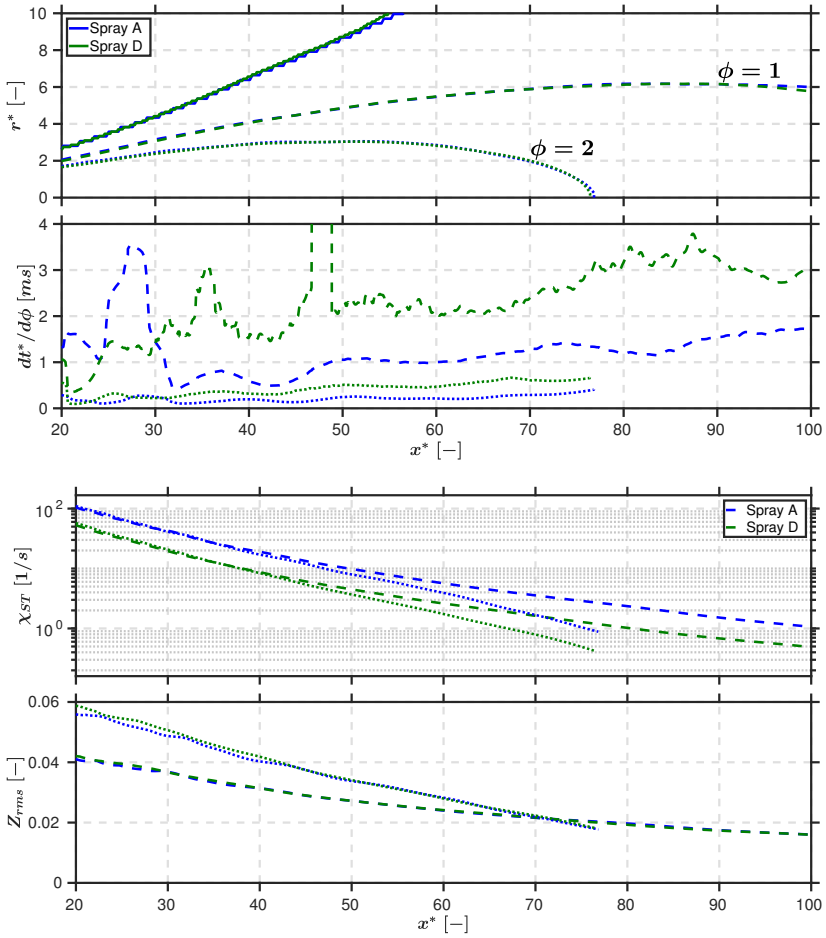

Figure 4.10: *Top: spray radius, $\phi = 1$ and $\phi = 2$ iso-contours for the inert Spray A and Spray D. The next panels show local residence time, stoichiometric scalar dissipation rate and mixture fraction rms profiles along reference ϕ iso-contours. Spray spatial coordinates normalized by d_{eq}.*

To conclude the description of the spray evolution, the third and fourth panels in Fig. 4.10 show the scalar dissipation rate at stoichiometric conditions and mixture fraction rms for Spray A and Spray D, which are input parameters for flamelet models such as the UFPV model. These variables are

plotted along the same reference iso-contours of ϕ shown in the top panel of the figure. Both, χ_{ST} and Z_{rms} profiles, exhibit lower values downstream the nozzle pointing to less intense turbulent fluctuations in the mixture fraction field due to lower mean velocities and consequently lower pulsating components. Results also show that higher χ_{ST} is predicted for Spray A for a given ϕ, in line with faster mixing occurring for the smaller nozzle, which creates more important gradients thus yielding to a more strained mixture state. It is also interesting to note that Z_{rms} profiles for both nozzles virtually fall on top of each other. This normalization of Z_{rms} might be expected giving that the normalization of the axial coordinates leads to the normalization of Z. χ_{ST} profiles on the contrary, do not exhibit the same normalizing feature, since it not only depends on Z_{rms} but also on the ratio ε/k (see Equation 3.2.11). The latter ratio can be interpreted as the inverse of a turbulent mixing time, that being linearly dependent with the nozzle diameter [54], goes in line with decreased χ_{ST} values for the larger nozzle.

4.3. The Spray A

In this section, the ECN Spray A reacting reference condition (see Table 3.1 for injection and thermodynamic conditions) is analyzed in detail. The analysis is focused on the autoignition sequence and the flame structure at quasi-steady state conditions. Results from the WM model, the UFPV-0 model and the UFPV model are compared to assess the implications of the well-mixed or flamelet assumptions for the flame sub-grid structure. All CFD cases presented under this section use the Yao mechanism unless otherwise stated. The concept of mixing trajectories (see Appendix 4.5 for a full description of the concept) is used to enable a direct link between combustion development in spatial coordinates and more-relevant equivalence ratio-temperature ($\phi - T$) coordinates.

4.3.1. autoignition sequence

The autoignition sequence as predicted by the WM model is presented in Fig. 4.11. Panels on the left show color-coded images for the normalized mass fraction[4] of CH_2O depicted in blue and OH depicted in red. These two species are used as tracers for low- and high-temperature ignition. Panels on the right show the contour of the local heat release rate (HRR) along

[4]Species mass fractions have been normalized by its maximum level at the last time in the figure.

with the spray radius plotted with a solid gray line and the most reactive equivalence ratio (ϕ_{MR}) plotted with a dashed green line. Homogeneous reactor 0D calculations were carried out to determine the mixture composition showing the fastest ignition process. Starting from the inert adiabatic mixing conditions, the shortest ID corresponds to $\phi_{MR} = 1.32$ which is in accordance with findings published in the literature for the same chemical mechanism [225]. To further illustrate the autoignition sequence, the last panel of the figure shows the integrated HRR where dot markers are used to indicate the timings for the color-coded images and the local HRR contours.

From the sequence depicted in Fig. 4.11, it can bee seen how the first-stage of ignition starts taking place at around 0.21 *ms* near the spray radial periphery and locations close to ϕ_{MR}. A simultaneous appearance of CH_2O and some degree of heat release is consistent with the use of formaldehyde as a tracer of low-temperature ignition. This observation also agrees well with the idea that ignition requires a certain degree of air-fuel mixing to reach reactive-enough equivalence ratios and temperature conditions, as well as some residence time to allow for the progress of chemistry. Beyond this timing, the location of this low-temperature heat release zone near the spray border is in agreement with longer residence time at the spray radial periphery as previously observed in Fig. 4.8. After the initial appearance of CH_2O at 0.21 *ms*, some sort of low-temperature heat release wave starts progressing towards richer mixtures (with a consistent increase in the integrated HRR in the last panel in Fig. 4.11) in the spray core followed by a quasi-homogeneous state of heat release at 0.3 *ms*. Next, an abrupt decrease in the release of heat throughout the spray cross section is observed between 0.33 *ms* to 0.36 *ms* just prior to the occurrence of second-stage ignition around ϕ_{MR}. At this time and location the color-coded image show a slight decrease in the CH_2O intensity close to the point where the main ignitions is observed to take place. The start of an intense heat release zone around the most reactive equivalence ratio location is accompanied by the appearance of OH, consistent with the choice of this species as a tracer of high-temperature ignition, and the abrupt consumption of CH_2O. Beyond 0.39 *ms*, a diffusion flame is established and the integrated HRR is controlled by mixing as seen in the last row of the figure.

The most relevant features observed in Fig. 4.11 are consistent with the autoignition sequence description presented in the work by Dahms et al. [88]. In this regard, the onset time for the appearance of low-temperature heat release at around 0.21 *ms*, the consequent propagation towards the spray core followed by a quasi-homogeneous state of heat release and finally the

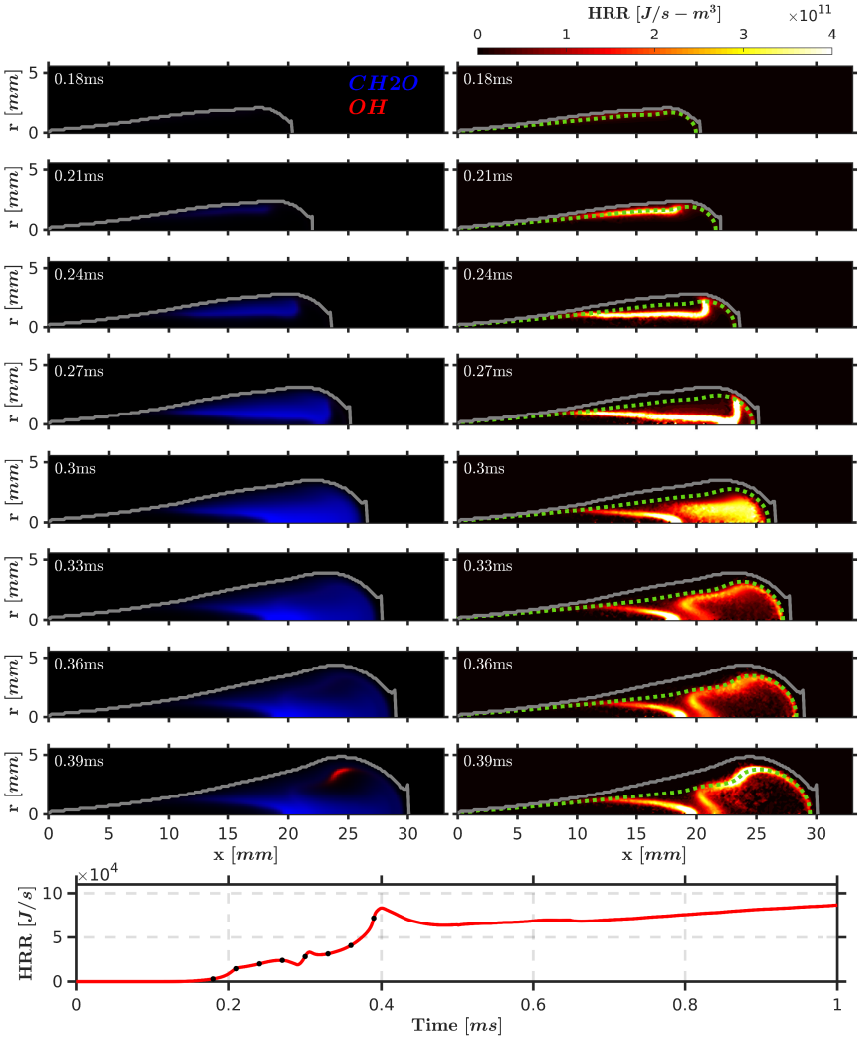

Figure 4.11: *Normalized species mass fraction, time- and spatially resolved local HRR for the Spray A using the WM model and the Yao mechanism. Dashed green contour at ϕ_{MR}. Integrated HRR (bottom) plotted with markers indicating HRR contours timing.*

decrease in chemical activity prior to the second-stage ignition are all features that go in line with the experimental observations and supporting modeling results presented by the authors. On the contrary, the high-temperature heat release zone confined around ϕ_{MR} observed at 0.39 *ms* is in disagreement

with the experimental observation (also supported by modeling results) made by Dahms et al. where main ignition was seen to take place over a wide range of equivalence ratio.

The post-ignition sequence is presented in Fig. 4.12. On the left panels, HRR contours in spatial coordinates are plotted while on the right panels, HRR contours are plotted in $\phi - T$ coordinates. In both type of HRR contours, mixing trajectories are included to bridge a link between spatial and $\phi - T$ coordinates. At 0.39 *ms* two distinctive heat release zones can be distinguished. On the one hand, the intense high-temperature heat release zone which is clearly centered around ϕ_{MR} as seen in $\phi - T$ coordinates. This intense HRR spot observed in spatial coordinates near the spray radial periphery corresponds to the highest temperature in the $\phi - T$ representation. On the other hand, the low-temperature heat release zone (already seen at 0.3 *ms* in Fig. 4.11) is observed to occur over a wide equivalence ratio range, when represented in $\phi - T$ coordinates. Thus, the farthest blue marker from the nozzle at $x \approx 20\ mm$ on the first mixing trajectory (closest to the spray axis) corresponds to the point at $\phi \approx 5$, the next two points at $\phi \approx 4$ and $\phi \approx 3$ correspond to blue markers on the second and third mixing trajectories, respectively. Furthermore, for all three trajectories a second low-intensity heat release front occurs just downstream of the initial one at a slightly higher temperature (around 1200 K). This zone will later result in the LOL stabilization region. Both low- and medium-temperature heat release regions remain essentially steady for the remaining part of the reacting spray evolution, as they are located in the quasi-steady part of the spray.

Finally, a distinctive feature for the WM model post-ignition results, can be observed for times beyond 0.39 *ms*. In this sense, the high-temperature heat release spot observed in spatial coordinates splits into two fronts. One of the fronts progresses upstream, towards the position at which LOL will later stabilized. The other front progresses downstream towards the spray head. The progress of this second heat release front in spatial coordinates can be linked to $\phi - T$ coordinates through the mixing trajectories starting from the axis towards higher radial coordinates in physical space, which correspond to mixing trajectories from richer to leaner values in the $\phi - T$ coordinates. At 0.5 *ms* the heat release front has not yet reached the two trajectories closest to the axis. Consequently, on the $\phi - T$ representation these two mixing trajectories have still not reached the maximum temperature on the map (evidenced by the almost horizontal temperature level between $\phi \approx 2$ and $\phi \approx 3$). At 0.6 *ms* the heat release front has just passed through the

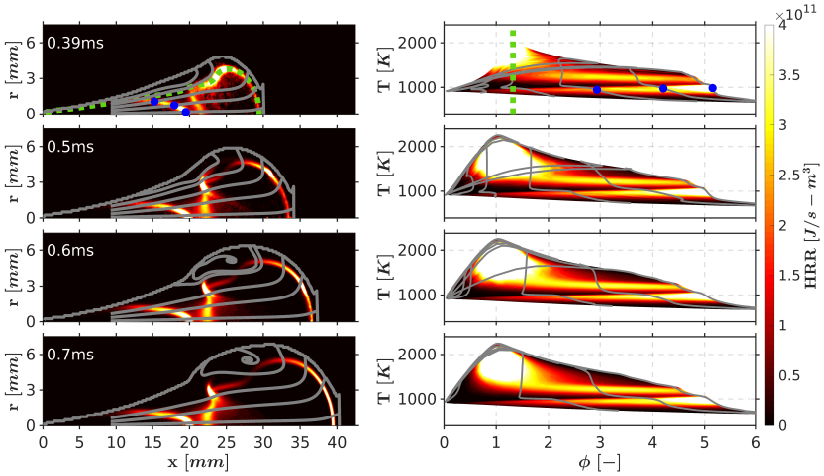

Figure 4.12: *Normalized species mass fraction, time-resolved local HRR in spatial coordinates (left) and $\phi - T$ coordinates (right) for the Spray A using the WM model and the Yao mechanism. ϕ_{MR} highlighted with a green dashed line. Low-temperature heat release zone highlighted with blue markers.*

second mixing trajectory closest to the axis, causing it to reach the maximum temperature on the $\phi - T$ representation for any equivalence ratio value. Lastly, at 0.7 *ms* the heat release front has reached the spray axis and all mixing trajectories have reached the maximum temperature for the whole range of equivalence ratios.

As stated earlier, the analysis of the reacting Spray A is focused on the assessment of the well-mixed and flamelet assumptions for the flame sub-grid structure. Under this statement, the next logical step would be to present results from the UFPV model. Nonetheless, in an attempt to establish an intermediate scenario that might enable a better understanding of the changes introduced when moving from the WM assumption to the flamelet assumption, Fig. 4.13 shows the autoignition sequence for the modified version of the UFPV model, denoted as UFPV-0. With this model, the flamelet manifold is built without any presumed-PDF integration (neither for mixture fraction nor for scalar dissipation rate) in order to better capture spatial details that are otherwise softened by the presumed-PDF integration as later seen in Fig. 4.14. In this way, WM and UFPV-0 results (Fig. 4.11 and Fig. 4.13), show the effect of changing the sub-grid description of the flame structure from the WM to the flamelet formulation, while UFPV-0 and UFPV results (Fig. 4.13 and Fig. 4.14), show the influence of TCI by means of presumed-PDF integration.

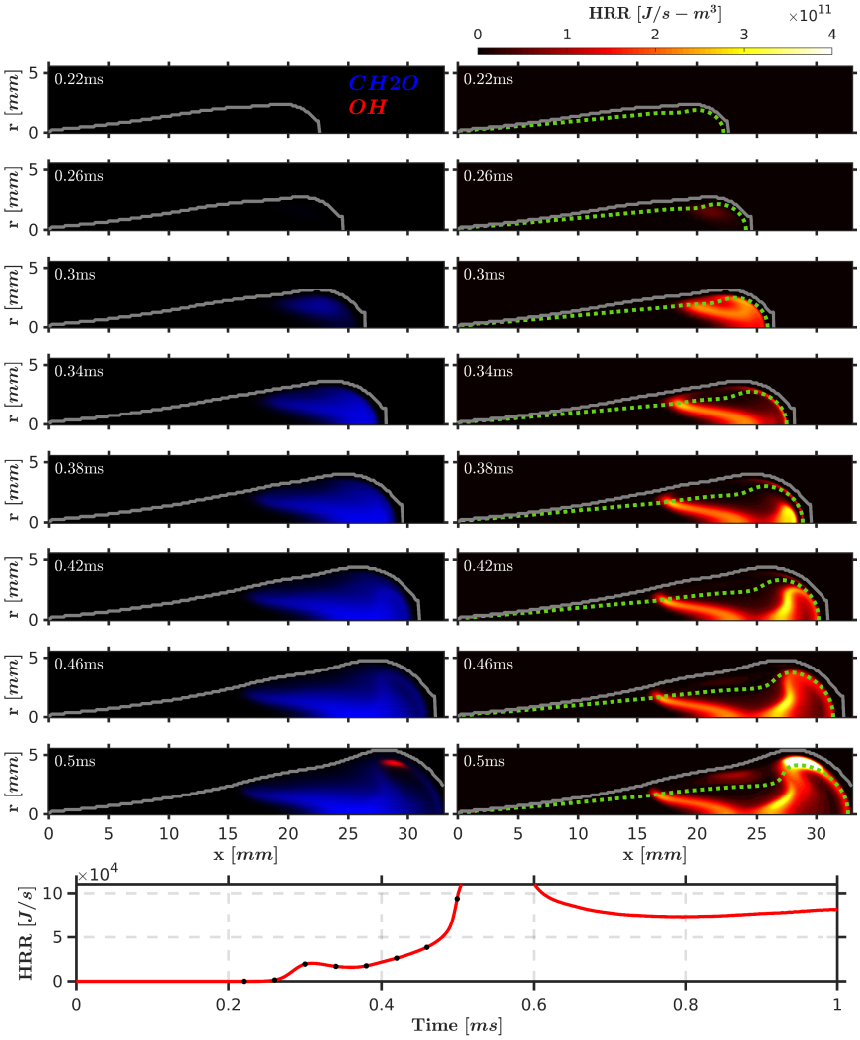

Figure 4.13: *Normalized species mass fraction, time- and spatially resolved local HRR for the Spray A using the UFPV-0 model and the Yao mechanism. Dashed green contour at ϕ_{MR}. Integrated HRR (bottom) plotted with markers indicating HRR contours timing.*

Similarly to WM results, it can be observed from Fig. 4.13 how initially heat is released from the spray radial periphery towards the spray axis before reaching a stabilized cone-shaped low-temperature heat release front at 0.34 *ms*. Early heat release is accompanied, as in the case of WM results, by the appearance of CH_2O. Unlike WM results, where a well-defined low-temperature reaction front was observed in the initial stages (0.24

ms), the evolution of species and heat release seems to be more volumetric with the UFPV-0 model. Furthermore, reactions tend to be located further downstream compared to WM results, probably due to the inhibiting effect of the higher scalar dissipation rate in locations close to the nozzle as seen in Fig. 4.10. The quasi-homogeneous heat release state observed for the WM model at 0.3 *ms* seems to be occurring also for UPFV-0 at 0.38 *ms*, although spatially confined to a region closer to the spray tip near the spray axis. After that, heat release decreases within this reaction zone, which slightly recedes upstream towards the spray radial periphery. Then, high-temperature ignition takes place accompanied by the appearance of OH and the consumption of CH_2O. The high-temperature ignition zone is located at around 27 *mm*, further downstream compared to WM results where this zone was located slightly upstream of 25 *mm*.

Having introduced the intermediate UFPV-0 results, Fig. 4.14 shows the autoignition sequence predicted by the UFPV model using the same layout already described for WM and UFPV-0 results. Once again, first-stage ignition starts taking place near the spray radial periphery. Nonetheless, unlike predictions using the WM model, the UFPV model predicts this first-stage ignition as taking place in a much broader area in the spray and not only around the most reactive equivalence ratio. Moreover, the intensity of this initial release of heat is lower compared to WM results (Fig. 4.11 and Fig. 4.14 share the same color scale), which will be a constant feature through the whole ignition sequence. Next, heat release progresses towards the spray fuel-rich core reaching a quasi-homogeneous reaction state close to the spray head at around 0.32 *ms* similarly to WM results at 0.3 *ms*. However, the low-temperature heat release front is not confined to a concrete region in the spray as it was predicted in the latter model. Additionally, not such an abrupt decrease in chemical activity throughout the spray cross section, prior to second-stage ignition, is observed with the UFPV model (0.36 to 0.4 *ms*) as was the case for the WM model (0.33 *ms*). At 0.4 *ms* an increase in HRR level is visible near the spray radial periphery close to the spray tip, where second-stage ignition eventually takes place at around 0.44 *ms*. This observation is consistent with high residence time and low χ_{ST}, both favorable for autoignition [226]. In terms of autoignition tracer species, CH_2O is again observed to be linked to low-temperature heat release while on the other hand, the presence of OH coincides with the start of high-temperature heat release. This last zone is predicted slightly downstream of 25 *mm* for the UFPV model and slightly upstream of 25 *mm* by the WM model (Fig. 4.11).

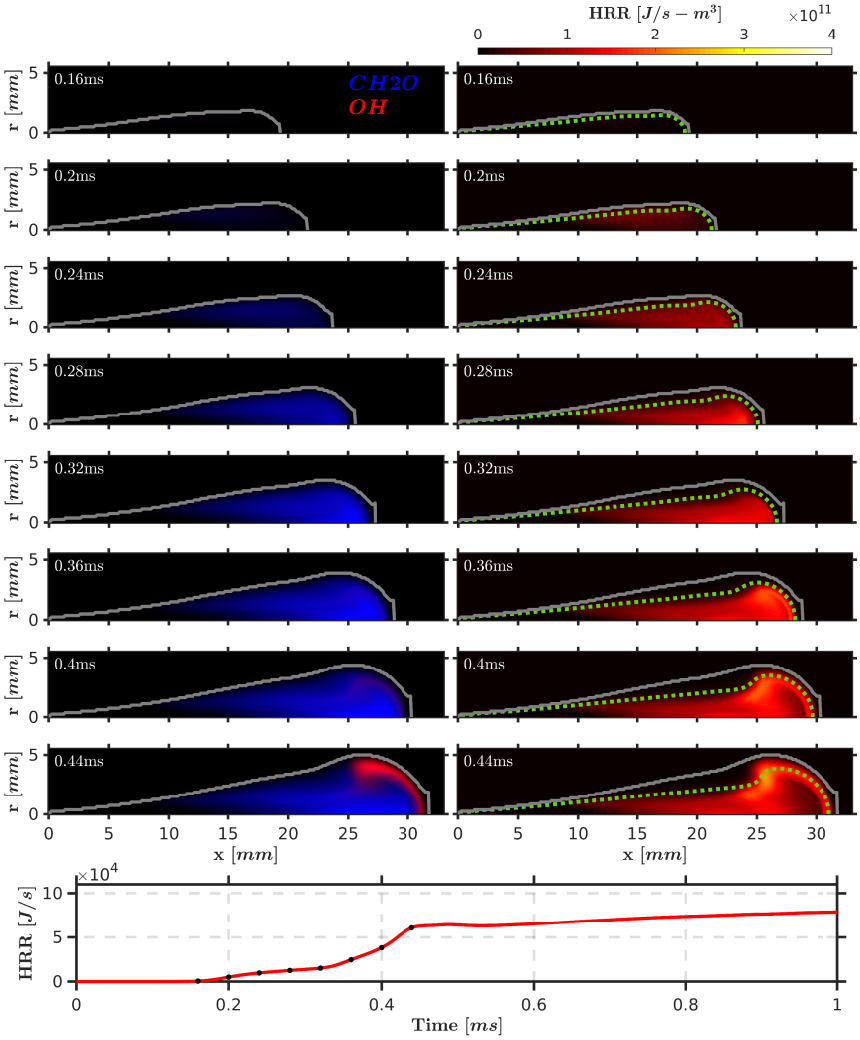

Figure 4.14: *Normalized species mass fraction, time- and spatially resolved local HRR for the Spray A using the UFPV model and the Yao mechanism. Dashed green contour at ϕ_{MR}. Integrated HRR (bottom) plotted with markers indicating HRR contours timing.*

Observed differences between WM and UFPV results obey to two factors. First, the UFPV model makes use of reaction source terms obtained upon the flamelet formulation, in contrast to the homogeneous reactor formulation in the WM model. Second, the UFPV model uses a presumed-PDF approach to account for turbulent fluctuations, which are neglected in the WM model. Regarding differences between UFPV-0 and UFPV results (Fig. 4.13 and

Fig. 4.14), the effect of presumed-PDF becomes quite apparent. The main effect is the smoothing of gradients that results in a more volumetric description of the spray ignition sequence. A second important feature is the decrease in heat release seen both in the spray HRR contours and in the integrated HRR plots. Finally, while the spatial location of all such events is pretty similar, the timing becomes slightly advanced for UFPV. All these results are a consequence of the averaging of the different igniting flamelets.

Based on the conceptual description and experimental observations reported in the literature [88] the UFPV model successfully captures autoignition key features of the ECN Spray A. Low-temperature reactions are seen to be starting at the spray radial periphery and then moving towards the spray axis. The quasi-homogeneous state of low-temperature heat release and the subsequent decrease in chemical reactivity before the main ignition event are also captured by the model. Finally, the model predicts second-stage ignition as taking place in a broader range of mixtures and not being confined around ϕ_{MR}. Diffusion phenomena induced by the scalar dissipation rate as well as the presumed-PDF approach allows the UFPV model to capture this last feature which is not reproduced in a well-mixed approach. Finally, the inclusion of such sub-grid diffusion effects by means of χ_{ST} delays the overall temporal sequence of autoignition in around 0.1 *ms* compared to the well-mixed approach, while the presumed-PDF approach advances back the timing of events in approximately 0.05 *ms*.

The post-ignition sequence predicted by the UFPV model is shown in Fig. 4.15. As already seen in the spatial representation of HRR contours, second-stage ignition takes place in a broader range of equivalence ratios and not just around ϕ_{MR}. Compared to WM results (Fig. 4.12), where a defined steady low-temperature reaction zone was observed to be established upstream (10-20 *mm*) with another intermediate reaction layer close to the axis (around 22 *mm*) and the diffusion flame stabilization occurred by the propagation of two fronts along the stoichiometric surface, UFPV results show a much less intense low-temperature front over a wide spray region (15-25 *mm*) with the main heat release over the whole spray cross-section at around 20-25 *mm*. No transient front evolution is observed around the stoichiometric surface as was the case for the WM model. An important feature, however, is the very different appearance of the heat release at the LOL location, which will be analyzed in the next subsection.

For the sake of brevity all CFD cases presented up until this point use the Yao mechanism. Nevertheless, main features and observations discussed for the Yao mechanism also hold valid for the Narayanaswamy mecha-

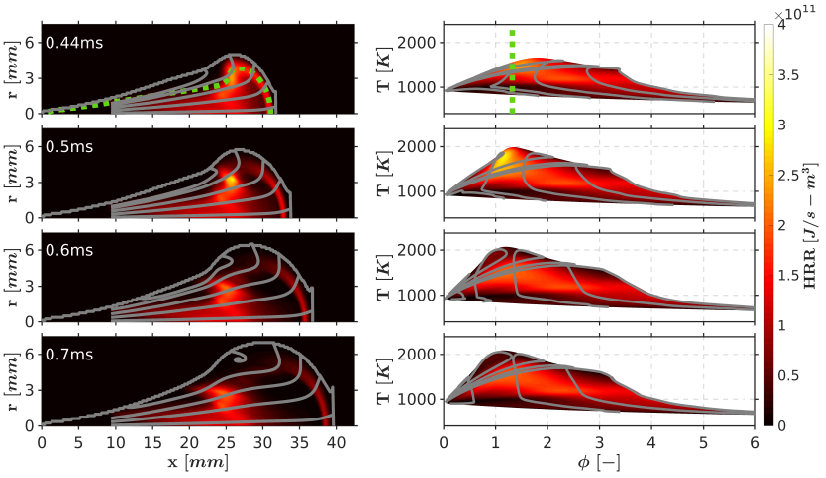

Figure 4.15: *Normalized species mass fraction, time-resolved local HRR in spatial coordinates (left) and $\phi - T$ coordinates (right) for the Spray A using the UFPV model and the Yao mechanism. ϕ_{MR} highlighted with a green dashed line.*

nism. The latter will be later used for the study of soot production in Chapter 5 since it includes PAH chemistry not accounted for in the Yao mechanism. To highlight the similarities in terms of autoignition between the Yao and Narayanaswamy mechanisms, and to conclude this section, Fig. 4.16 shows the autoignition sequence predicted by the UFPV model using the Narayanaswamy mechanism. As mentioned earlier, the main features described for UFPV results with the Yao mechanism are also reproduced by the Narayanaswamy mechanism. First indicators of low-temperature chemical activity (CH_2O and low HRR levels) are observed to appear near the spray radial periphery to then progress toward the spray core until an intense heat release spot is visible at 0.54 *ms*. Beyond this point in time, chemical activity progresses until second-stage ignition, characterized by high heat release rate, is reached with the consequent appearance of *OH* and consumption of CH_2O. An interesting observation is that the autoignition sequence is not as volumetric as for the Yao mechanism results. Due to a longer ID (Fig. 4.5) for the Narayanaswamy mechanism, the autoignition zone is shifted downstream compared to the Yao mechanism. In fact, the quasi-homogeneous heat release state observed for the Yao mechanism (see Fig. 4.14) at 0.28 *ms* around 20-25 *mm* is observed for the Narayanaswamy mechanism at 0.54 *ms* beyond 30 *mm*. As both mixture fraction variance and scalar dissipation rate decrease downstream from the nozzle (see Fig. 4.10), spatial smoothing

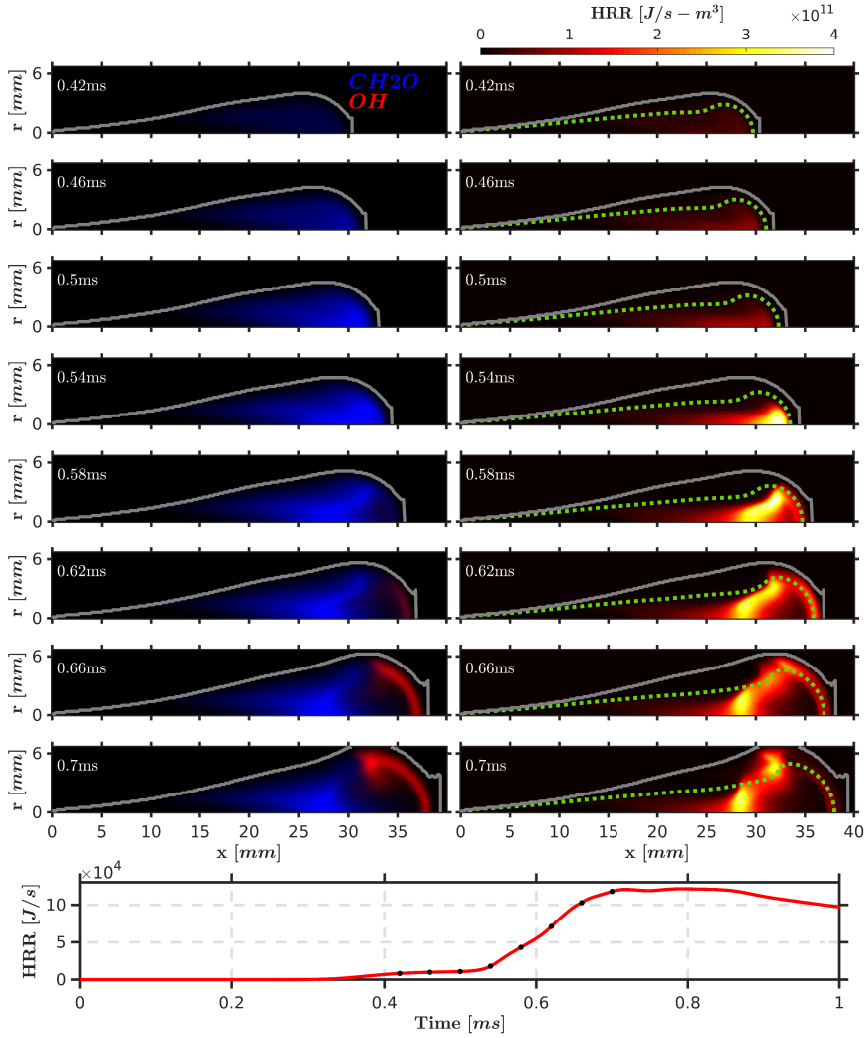

Figure 4.16: *Normalized species mass fraction, time- and spatially resolved local HRR for the Spray A using the UFPV model and the Narayanaswamy mechanism. Dashed green contour at ϕ_{MR}. Integrated HRR (bottom) plotted with markers indicating HRR contours timing.*

effects associated to presumed-PDF integration becomes less relevant thus resembling UFPV-0 results (Fig. 4.13) with sharper structures compared to the aforementioned more volumetric structures seen for the Yao mechanism.

4.3.2. Flame structure at quasi-steady state

In spite of the almost quasi-steady appearance of the reacting spray at 0.7 *ms* in the previous subsection, the analysis of the LOL for all modeling approaches is made for a later time in which the spray head does not interact with the base of the flame. Fig. 4.17 shows color-coded images for the normalized mass fraction[5] of CH_2O, OH and the soot surface growth species C_2H_2 with the spray radius (solid line) and the stoichiometric equivalence ratio surface (dotted line). Both, the WM model (top) and the UFPV model (bottom), predict CH_2O at rich mixtures in the vicinity of the flame base where heat is released from low-temperature reactions. Radially displaced, OH is placed around the stoichiometric surface coinciding with the location of the high-temperature reactions from the diffusion flame. Lastly C_2H_2, a species of particular relevance for the study of soot production in Chapter 5 due to its relevance for the formation and growth of PAHs and the later surface growth of soot (discussed in Section 2.2), is observed to be comprised in the fuel-rich core of the spray between the zones where CH_2O and OH are present.

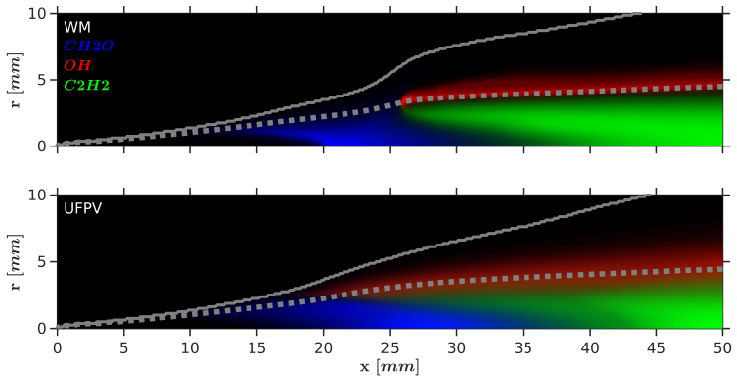

Figure 4.17: *Color-coded image for the Spray A with the WM model (top) and the UFPV model (bottom) using the Yao mechanism.* $\phi = 1$ *highlighted with a gray dashed line.*

The flame structure predicted by the WM and UFPV models qualitatively agrees with experimental results shown in Fig. 4.18. Experimentally, the flame structure is characterized based on planar laser-induced fluorescence (PLIF) and chemiluminescence techniques [207]. 355 *nm* PLIF signal is

[5] Species mass fractions have been normalized by the maximum level in the computational domain.

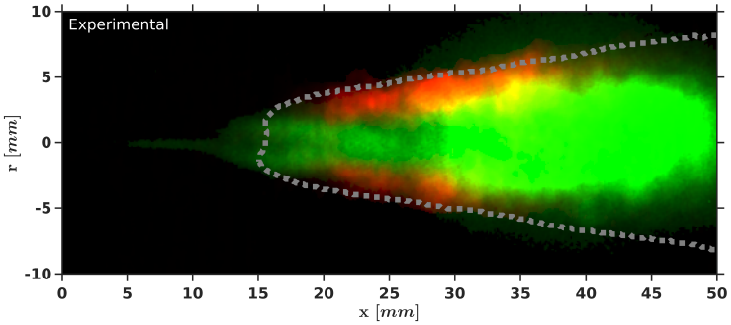

Figure 4.18: *Spray A quasi-steady flame structure with OH PLIF signal in red and 355 nm PLIF signal in green. Gray dotted line corresponds to the contour of OH^* chemiluminescence signal [207].*

an indicative of the presence of CH_2O in the vicinity of the LOL (marked by the most upstream location of the OH^* contour). As discussed by the authors, further downstream, the 355 *nm* PLIF signal is wrapped by the *OH* PLIF signal and its intensity is most likely to be caused by the presence of PAHs relevant for soot production. In terms of heat release rate, in Fig. 4.19 three distinctive areas can be identified i.e. a low-temperature structure (zone I) at the flame base resulting from first-stage ignition, an intermediate partially-premixed flame front (zone II) around the LOL location and a diffusion flame front (zone III) around the stoichiometric equivalence ratio. While zones I and II are quite similar for both models, except for the fact that both fronts are narrower for the well-mixed model due to the absence of sub-grid flamelet diffusion and presumed-PDF integration, the location and appearance of zone II is a key difference between WM and UFPV predictions.

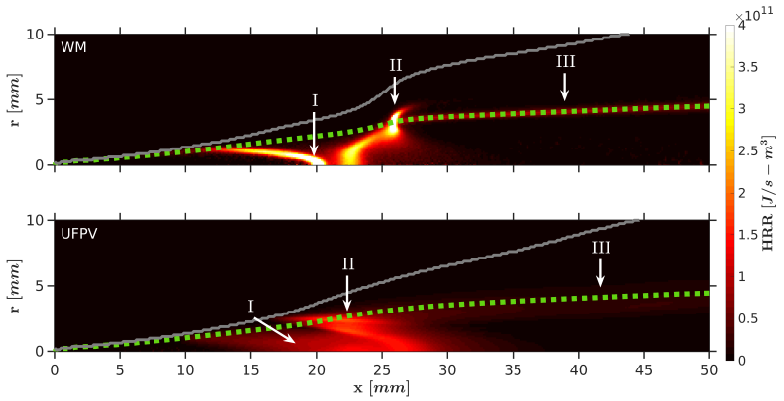

Figure 4.19: *Quasi-steady Spray A local HRR using the WM (top) and UFPV (bottom) models with the Yao mechanism. Dashed line at $\phi = 1$.*

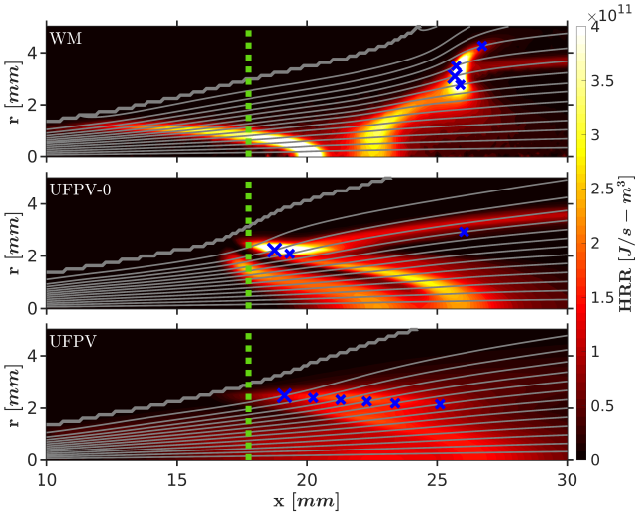

Figure 4.20: *Local HRR contour at quasi-steady state near the LOL location for the Spray A using the WM model (top), the UFPV-0 (middle) and the UFPV model (bottom). Closest mixing trajectory to experimental LOL location (green dashed line) is highlighted with the biggest "X" blue marker.*

Fig. 4.20 shows a zoomed view of the local HRR contour around the area where the LOL is stabilized including results for the well-mixed model, as well as the UFPV and UPFV-0 approaches. Mixing trajectories have been added (solid gray lines) to later allow for the linking oh spatial and $\phi - T$ coordinates. Blue markers are plotted at the locations where *OH* mass fraction reach 14% of the maximum value in the spray following ECN guidelines for the location of the LOL. From Fig. 4.19, low- and high-temperature heat release fronts (Zones I and II) were shown to be spatially decoupled for the WM case. In contrast, the flame structure predicted by the UFPV model around the stabilized LOL position (Fig. 4.20 bottom) shows how Zones I and II are virtually merged. Compared to the WM case, the introduction of χ_{ST} in the UFPV-0 model seems to contribute to the stabilization of Zone I further downstream from the nozzle where χ_{ST} values are lower, as shown in Fig. 4.10. This observation is consistent with a delayed temporal evolution of autoignition (comparing WM and UFPV-0 results) as described in the previous subsection, since high χ_{ST} values near the nozzle inhibit combustion. As for Zone II, sub-grid diffusion seems to contribute to the stabilization of the high-temperature front in both UFPV approaches closer to the nozzle as compared with WM results. Furthermore, the observed intermediate temperature zone close to the spray axis in the WM approach has a very similar shape in the UFPV-0 approach to the low-temperature

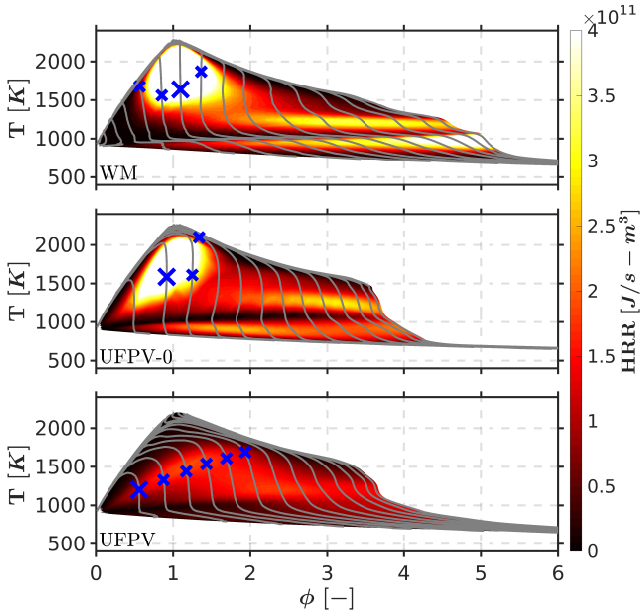

Figure 4.21: *Local HRR contour in $\phi - T$ coordinates at quasi-steady state for the Spray A using the WM model (top), the UFPV-0 (middle) and the UFPV model (bottom).*

one. The averaging role of the presumed-PDF approach is also seen, when comparing UFPV-0 and UFPV, in the sense that both low-temperature zones become eventually merged and the high-temperature heat release drops in intensity. All such features will be analyzed in $\phi - T$ coordinates in the following.

With the inclusion of mixing trajectories, the path followed by a "conserved gas particle" can be depicted both in spatial and $\phi - T$ coordinates. Analysis of WM results (Fig. 4.21 top) reveals how any "conserved gas particle" starts diluting almost along the inert adiabatic mixing trajectory, with a first noticeable increase in temperature as it passes through the low-temperature area (Zone I in Fig. 4.20 top). As already discussed, this initial flame front occurs at a similar temperature but at a different equivalence ratio for every single trajectory depending on the residence time. Beyond Zone I, two types of evolutions can be observed. For mixing trajectories closer to the axis, that is, moving through richer equivalence ratio values, the also mentioned intermediate flame front can be observed at around 22–23 *mm* and correspondingly at a temperature of around 1100 *K*. After that, no heat will be released along those trajectories until reaching the stoichiometric

flame front. On the contrary, mixing trajectories reaching the stoichiometric flame front at around 25 mm directly run into the high-temperature heat release zone, and the intermediate temperature ignition is missing. This is probably due to the shorter residence time associated with such radially displaced trajectories, which enables reaching high-temperature ignition for similar equivalence ratio values as those closer to the axis. The inclusion of UFPV-0 results (Fig. 4.21 middle) allows isolating the effect of χ_{ST} in $\phi - T$ coordinates. As it was already mentioned when analyzing the effects of diffusion in spatial coordinates, there are two distinctive effects. On one hand, when comparing the WM results (no effect of χ_{ST}) with UFPV-0, it becomes clear that diffusion decreases reactivity for low-temperature chemistry (Zone I in Figure 17) as the HRR is less intense in the zone below 1000 K, which becomes evident in the $\phi - T$ representation. On the other hand, high-temperature heat release (upper part in the $\phi - T$ centered around $\phi = 1$) becomes wider in equivalence ratio and temperature ranges, especially toward the lean region. This effect speeds up the transition from low-temperature to high-temperature heat release with the consequent stabilization of LOL closer to the nozzle compared to WM results. Finally, the description can also be carried out for the UFPV model (Fig. 4.21 bottom). In the same way as for spatial coordinates, the distinction among different flame fronts in the $\phi - T$ representation is softened due to averaging. In this case, the low-temperature flame front occurs over a wide region upstream 20 mm for all trajectories, but the trends in the $\phi - T$ representation does not depart substantially from the inert adiabatic mixing line. Instead of separated reaction regions around the LOL as for the WM model, UFPV shows a single high heat release zone starting radially at around 19 mm and reaching the spray axis at around 26 mm. All mixing trajectories flow through this zone, shown by the steep increase in temperature in the $\phi - T$ representation over a wide range of equivalence ratio values.

According to the previous differences in heat release zones, modeling approaches predict different locations for the LOL. On one hand, the WM approach predicts LOL to be stabilized on the mixing trajectory passing through the most reactive spot in the high-temperature heat release zone close to the stoichiometric equivalence ratio. On the other hand, the UFPV model predicts LOL to be stabilized at the lean high-temperature heat release zone. Furthermore, the UFPV-0 shows the underlying flame structure, with an intense stoichiometric combustion, which extends toward both the lean and rich sides, which may bring some remembrance with triple flame structures. Recent findings supported by direct numerical simulations (DNS)

under similar operating conditions show that LOL stabilization might take place at lean, stoichiometric or rich zones depending on the local flame topology including triple flames [227].

4.4. The Spray D

Similarly to the Spray A analysis, this section deals with the autoignition sequence and the flame structure at quasi-steady state for the ECN Spray D reference condition. Thus, thermodynamic conditions are kept unchanged and just the nozzle size is varied from the small nozzle (Spray A) to a bigger nozzle (Spray D). Since the implications of the WM and the flamelet formulations have already been discussed for the Spray A, this section focuses on the effect of the nozzle diameter. Consequently, only results for the UFPV model using the Yao mechanism are presented.

4.4.1. autoignition sequence

After a detailed description of the different combustion modeling approaches for the Spray A case, the UFPV model is used to evaluate the influence of nozzle diameter in Diesel combustion following similar concepts. First, the autoignition sequence of Spray D is analyzed. Autoignition key species (panels on the left) and local HRR contours (panels on the right) are plotted in Fig. 4.22 along with the integrated heat release rate at the bottom of the figure. The sequence depicted in Fig. 4.22 evidences that both nozzles (see Fig. 4.14 for Spray A results) share similar features on how the flame is established, that is, a cool flame originated at the spray radial periphery (in a broader range of mixtures not limited to ϕ_{MR}), a quasi-homogeneous state of heat release (at 0.32 *ms* for Spray A and at 0.37 *ms* for Spray D) and finally a decrease in the HRR prior to second-stage ignition taking place at the spray radial periphery (at 0.44 *ms* for Spray A and at 0.53 *ms* for Spray D). Both, first- and second-stage ignition are seen to coincide in time with the appearance and consumption of CH_2O and OH, respectively, as for the Spray A. In terms of location, second-stage ignition for the smaller nozzle is seen to occur closer to the spray tip compared to Spray D, where this occurs essentially upstream of the spray tip front. Higher χ_{ST} values reported before for Spray A play an important role in the spatial shift of ignition location compared to the larger nozzle. Differences in ignition location among nozzles are consistent with those reported in the literature from experimental observations by Pastor et al. [206].

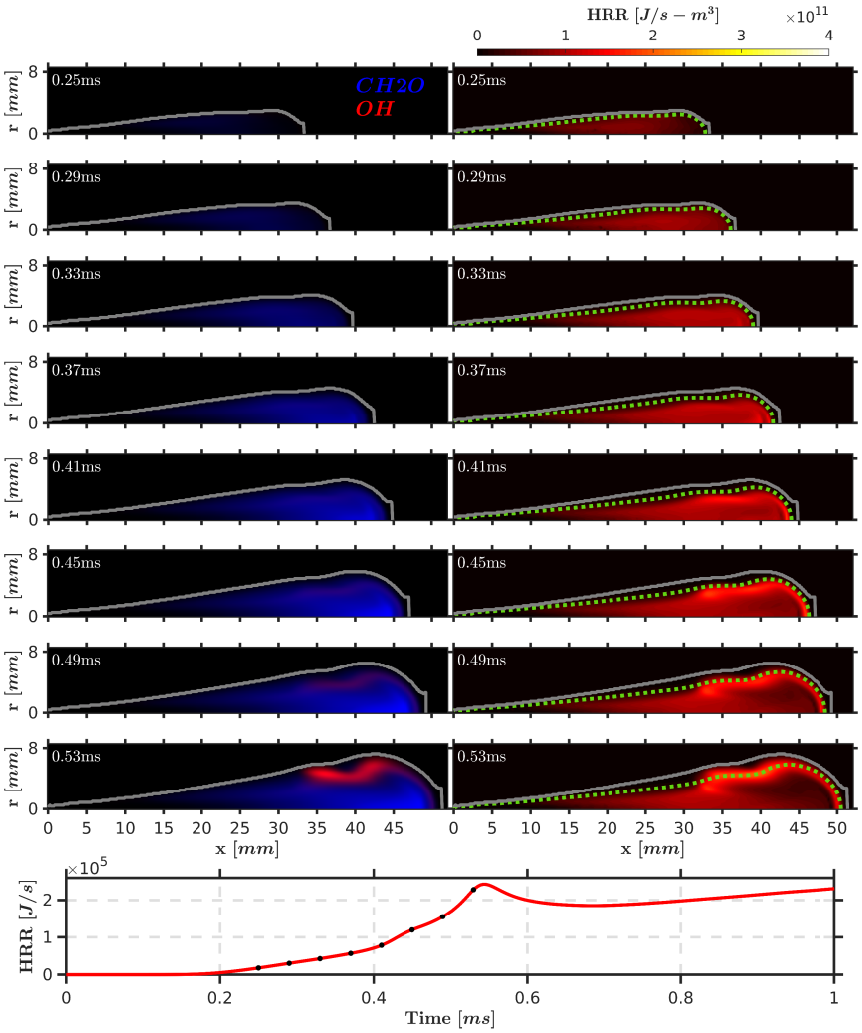

Figure 4.22: *Normalized species mass fraction, time- and spatially resolved local HRR for the Spray D using the UFPV model. Dashed green contour at ϕ_{MR}. Integrated HRR (bottom) plotted with markers indicating HRR contours timing.*

In agreement with previously discussed longer residence time for Spray D, a slower progression of the autoignition sequence is expected compared to Spray A, as it takes more time to reach reactive ignitable mixtures, which might be compensated to some extent by the lower χ_{ST} values of the larger nozzle. From simulation results, the whole ignition sequence is seen to be already delayed from the initial low-temperature stages, and eventually,

Spray D ignites 94 *ms* later compared to Spray A. In that same direction, from experimental observations, Spray D high-temperature ignition occurs 137 *ms* later compared to Spray A. These differences are consistent with a slower mixing process as previously described in Section 4.2. Aside from timing, the general development of the ignition sequence on Spray D occurs at richer mixtures. The longer residence time for Spray D enables the ignition of these richer mixtures which are less favorable from the point of view of temperature and equivalence ratio. This observation will be further analyzed in the next subsection.

4.4.2. Flame structure at quasi-steady state

After ignition, both nozzles also share similar heat release zones at quasi-steady state. The previously observed Zones I, II and III for Spray A (Fig. 4.19 bottom) are also reproduced for Spray D, resulting in a similar flame structure, with an upstream location occurring at richer mixtures for the larger nozzle in accordance to the autoignition comparison. A closer look at Zone II in Fig. 4.23, where LOL is stabilized, confirms the similarity of Spray A and Spray D flame structure. The use of normalized coordinates already points at a stabilization of the flame base at a fuel-richer location in Spray D compared to Spray A. In Fig. 4.23, mixing trajectories are superimposed onto the local HRR contour, and in Fig. 4.24, the corresponding $\phi - T$ representations are shown. The positions where the mixing trajectories cross the contour of the 14% of the maximum OH mass fraction are highlighted with blue markers. As previously observed for Spray A, the closest point to the nozzle, which defines the LOL location, appears for both nozzles in the most radially displaced trajectory, that is, at lean conditions.

Despite evident similarities between the two studied nozzles, a major distinction has already been mentioned, that is, both ignition and LOL stabilization occur in fuel-richer mixtures in Spray D as compared to Spray A. This observation is sustained by a slower mixing process with consequent longer residence time for Spray D. In $\phi - T$ coordinates, Spray D richer combustion is evidenced by the presence of mixing trajectories increasing in temperature for $\phi > 4$, which does not happen for Spray A. Such trajectories are those closest to the spray axis, where the scalar dissipation rate is lower and residence time is longer, which also contributes to the possibility of chemical reactions to progress in richer equivalence ratio zones. On the contrary, trajectories linked to the LOL stabilization location (blue markers in Fig. 4.23 and Fig. 4.24) reach the lift-off limit at similar equivalence ratio and temperature values for both nozzles. However, the different development of

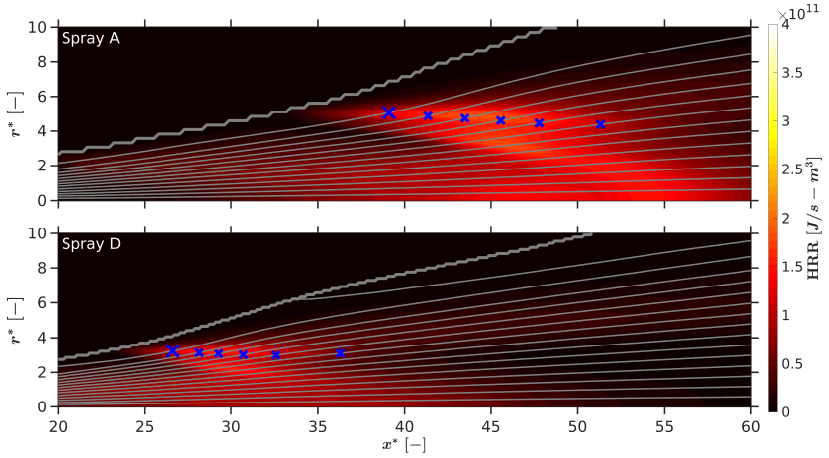

Figure 4.23: *Quasi-steady local HRR for the Spray A (top) and Spray D (bottom) using the UFPV model. Closest mixing trajectory to experimental LOL location is highlighted with the biggest "X" blue marker.*

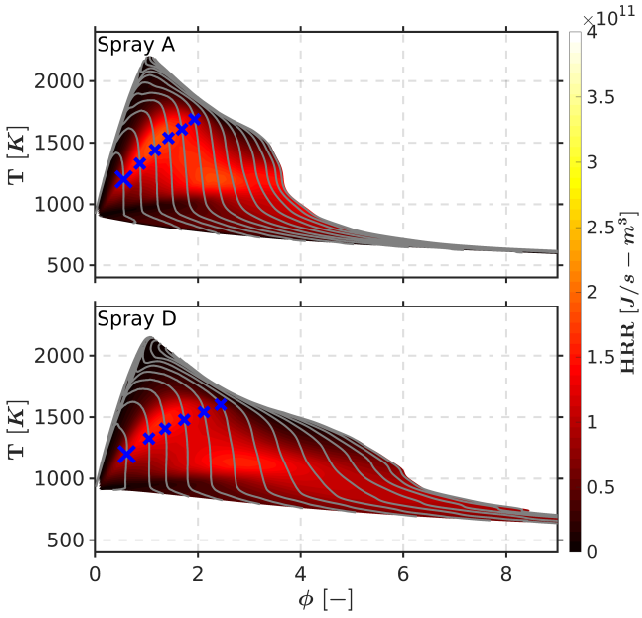

Figure 4.24: *Quasi-steady local HRR in $\phi - T$ coordinates for the Spray A (top) and Spray D (bottom) using the UFPV model. Closest mixing trajectory to experimental LOL location is highlighted with the biggest "X" blue marker.*

the mixing process in terms of spatial distribution and local residence time results in different spatial locations for this high-temperature zone when both nozzles are compared.

4.5. Summary

This chapter comprised the validation of the computational setup under reacting conditions. In addition, a detailed study has been presented emphasizing on the differences that the sub-grid flame structure and TCI induce on the spray autoignition sequence and flame structure at quasi-steady state. Differences induced by the change in the nozzle orifice diameter has also been studied. The main findings can be summarized as follows:

- Under inert conditions, local residence time has been quantified for Spray A and Spray D nozzles. Results show that this parameter increases at locations farther away from the nozzle both in axial and radial directions. For a given equivalence ratio, residence time decreases as mixing trajectories depart radially from the axis. This observation is consistent with the location at which main ignition is observed to take place. Both WM and UFPV models predict main ignition as taking place near the spray periphery. At this location in the spray, two observations should be emphasized. On one hand, a "conserved gas particle" has already diluted as it follows a mixing trajectory. On the other hand, local residence time is high-enough to let chemistry progress at the equivalence ratios more favorable for autoignition.

- The reduction of the nozzle diameter promotes faster mixing. Under inert conditions, the time spent at a given ϕ is shorter in Spray A compared to Spray D. Taking into account the description of the spray as a set of trajectories where mixture fraction is progressively decreasing, this observation means that the faster mixing for Spray A enables earlier reaching of ignitable equivalence ratio values. Therefore, shorter ID time for the smaller nozzle is consistent with shorter residence time.

- For the reacting reference Spray A condition, both WM and UFPV models predict similar global steps leading to main ignition. The main difference is related to the spatial width of the area that characterizes

this event. WM results show main ignition occurring at a narrow range of mixtures centered around ϕ_{MR}. On the contrary, UFPV results show how main ignition takes place on a broader range of mixtures.

- At quasi-steady state, the predicted flame structure for Spray A is remarkably different among the two combustion models. The higher scalar dissipation rate present in the near-nozzle region (only accounted for in the UFPV model) seems to shift further downstream the low-temperature heat release zone compared to WM results. In the high-temperature heat release zone, χ_{ST} is observed to play an opposite role, contributing to the stabilization of the LOL closer to the nozzle in contrast to WM results. The comparison of UFPV and the intermediate UFPV-0 model, considering the flamelet sub-grid structure but not the presumed PDF integration, evidences that one of the reasons for the wider spatial location of reaction zones is the averaging of laminar flamelets, smoothing the gradients within the reacting zones of the spray.

- UFPV results for Spray A and Spray D show a similar ignition sequence for both nozzles. Faster mixing and higher χ_{ST} values for Spray A cause main ignition to occur closer to the spray head compared to Spray D, where the main ignition occurs closer to the spray radial periphery.

- In spatial coordinates, both Spray A and Spray D share a similar flame structure at quasi-steady state. In $\phi - T$ coordinates, Spray D is characterized by richer mixtures being able to ignite. A slower mixing process, thus longer residence time, allows richer mixtures to ignite in the larger nozzle close to the axis, with lower scalar dissipation rate also contributing to this ignition capability.

4.A. Appendix: mesh convergence

The analysis of grid convergence is made for the reference Spray A inert condition. To that end, global and local quantities are analyzed for three meshes with different minimum cell sizes achieved through AMR. For all three cases, a truncated cone-shaped fixed embedding with a minor radius of 1 *mm*, a major radius of 5 *mm* and a length of 10 *mm* is used to add 250 μm cells in the vicinity of the nozzle. Minimum cell sizes of 250 μm, 125 μm and 62.5 μm with a base mesh cell size of 2 *mm* are in accordance to mesh setups used for the study of single-hole nozzle sprays similar to the ones studied in this work [228–230]. Fig. 4.25 shows the results for the spray tip penetration and liquid length (mean experimental value plotted with a dotted line). In terms of liquid length, meshes with 125 μm and 62.5 μm are virtually identical while the coarser mesh predicts a slightly shorter value. In contrast, spray tip penetration results converge for any of the three meshes.

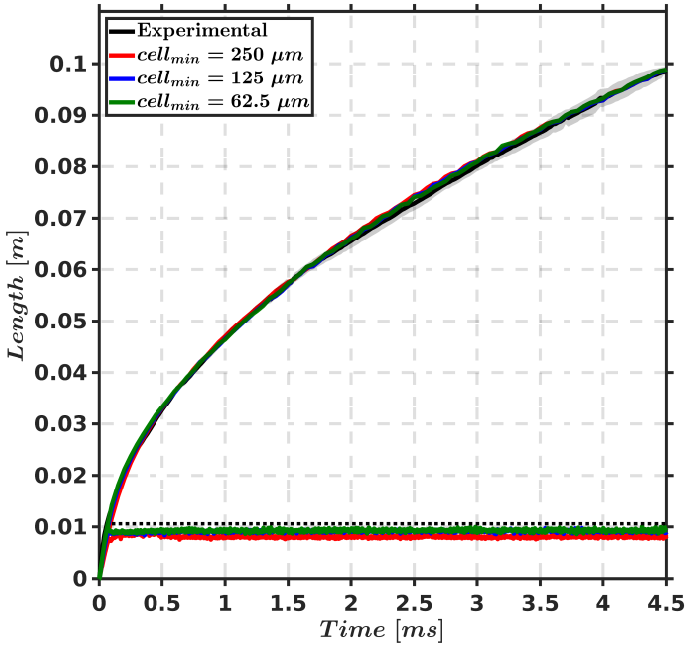

Figure 4.25: *Spray tip penetration and liquid length mesh convergence results for the reference inert Spray A.*

Similarly, results for local quantities evidences mesh convergence. Mean mixture fraction and its variance and axial velocity profiles along the spray axis in Fig. 4.26 along with radial profiles for the same variables in Fig. 4.27 show excellent results for mesh convergence with values that barely change for the different minimum cell sizes.

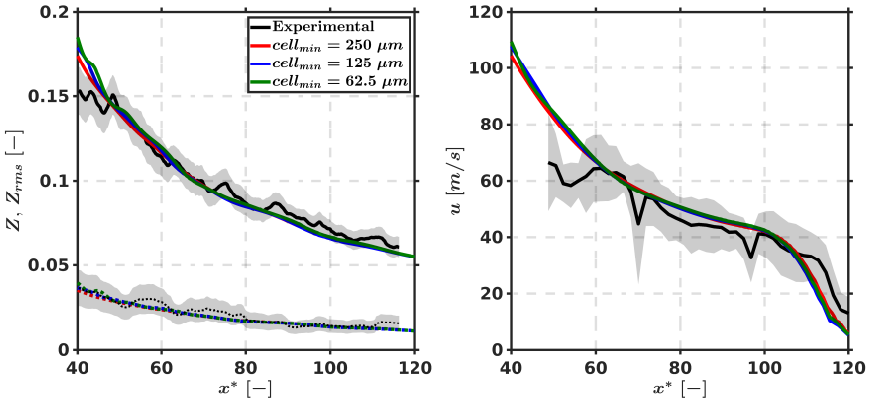

Figure 4.26: *Mixture fraction (solid line) and mixture fraction rms (dotted line) at 5 ms and axial velocity at 1.5 ms mesh convergence results along spray axis for inert Spray A.*

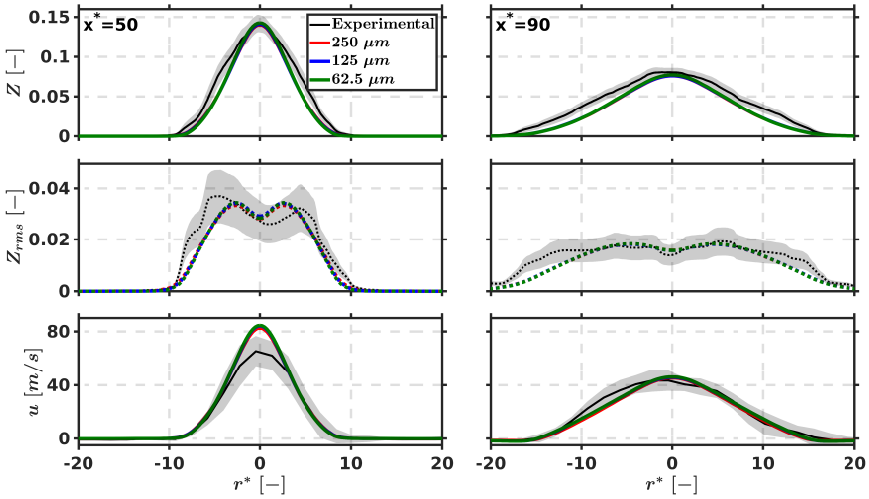

Figure 4.27: *Mixture fraction (top), mixture fraction rms (middle) and axial velocity (bottom) radial profiles at 5 ms for inert Spray A mesh convergence study.*

4.B. Appendix: mixing trajectories

In problems of momentum transfer in fluids, streamlines are commonly used for analysis as these describe the convective flow movement. In cases where convection and diffusion processes also intervene in the transport of species, both terms have to be accounted for when tracking species. Assuming azimuthal symmetry, generally occurring in single spray cases such as the ones under study in this thesis, so-called "mixing trajectories" can be solved by integration of the following equation

$$\frac{dx}{u+u_{dif}} = \frac{dr}{v+v_{dif}} \tag{4.B.1}$$

In Equation 4.B.1, u and v denote the convective components of the velocity field, while u_{dif} and v_{dif} allow for the consideration of the transport flow induced by the diffusion of mixture fraction. For high-Reynolds number sprays and under a RANS approach, turbulent diffusion plays a more dominant role compare to its laminar counterpart. Keeping this in mind, expressions for the diffusive components [231] can be written analogously to Fick's diffusion law according to

$$u_{dif} = \frac{D_t}{Z}\frac{\partial Z}{\partial x} \tag{4.B.2}$$

and

$$v_{dif} = \frac{D_t}{Z}\frac{\partial Z}{\partial r} \tag{4.B.3}$$

Assuming diffusivity equal to RANS turbulent diffusivity, for which the Schmidt number was set to unity, the diffusion coefficient in Equation 4.B.2 and Equation 4.B.3 can be calculated as $D_t = C_\mu k^2/\varepsilon$ with $C_\mu = 0.09$.

To illustrate some of the mixing trajectories main features, the mixing field for inert Spray A and Spray D is shown in Fig. 4.28 for several time instants after the start of injection. The contour of the spray is delimited by the spray radius marked at the locations where Z is 1% of the value on the spray axis. Mixing trajectories, mainly and Eulerian concept, are calculated downstream of the liquid length to avoid any effect induced by Lagrangian parcels. Time development of mixing trajectories agrees with the general evolution of the spray, for which a transient zone progresses at the tip zone, while a quasi-steady flow is established upstream. In this sense, mixing trajectories are almost straight lines, with a direction that barely changes until reaching around 70–80% of the tip penetration. Transient

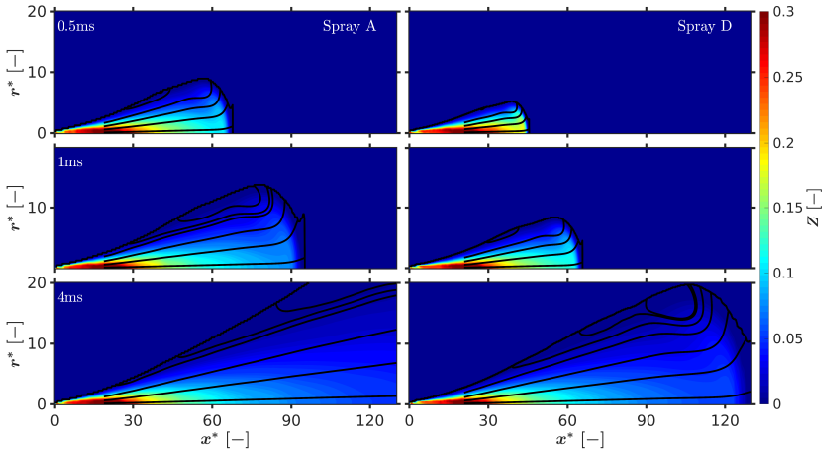

Figure 4.28: *Mixture fraction field and mixing trajectories for the inert Spray A (left) and Spray D (right).*

structures can be observed at the furthest radial locations around the tip of the spray. It is also worth mentioning that by normalizing the axial and radial coordinates, at any given point defined by (x^*, y^*) the same mixture fraction value for both nozzles is reached. This observation is confirmed as trajectories for both nozzles start at $x^* \approx 20 d_{eq}$, indicating that both nozzles have a similar saturation Z value. This is also expected since saturation Z depends on fuel, fuel temperature, ambient temperature and pressure.

Mixing trajectories are also analyzed for auto-similarity in Fig. 4.29. The axial coordinate has been normalized by the spray tip penetration, while the radial coordinate has been normalized by the flow width expressed in terms of the spray radius R. For both nozzles the normalized radial coordinate of a mixing trajectory remains essentially constant until $x/S \approx 0.8$, from which they are clearly affected by the transient nature of the spray tip and its main vortex. This holds for mixing trajectories from the axis until around 70% of the whole radial width. The quasi-steady and self-similarity analysis contribute to support the underlying symmetry in the spray A and Spray D mixing process.

Another feature worth mentioning is that mixing trajectories with constant r/R are closer to the spray axis and correspond to trajectories originated from the spray nozzle, meaning that a "gas particle" following any of these trajectories is diluted as it moves away from the nozzle. On the contrary, trajectories closer to the spray border correspond to "gas particles" entrained

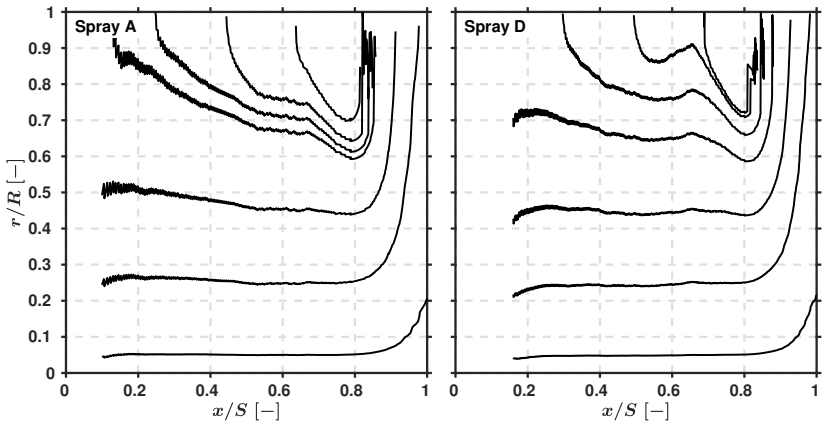

Figure 4.29: *Mixing trajectories radial ratio for the inert Spray A (left) and Spray D (right) at 4 ms.*

into the spray. These entrained "gas particles" follow mixing trajectories that are fuel-enriched before being completely incorporated into the spray after which they continue diluting with the entrainment of air.

Finally, and to provide an additional local indicator of mixing intensity, a local residence time has been defined based on mixing trajectories as the time spent per unit of equivalence ratio according to

$$\frac{dt^*}{d\phi} = -\frac{dt^*}{dl}\frac{dl}{d\phi} = -\left(\sqrt{(u+u_{dif})^2+(v+v_{dif})^2}\right)^{-1}\frac{dl}{d\phi} \tag{4.B.4}$$

In terms of physical meaning, this parameter quantify the time needed to change a unit value of equivalence ratio along a mixing trajectory or, in other words, the time spent at a given ϕ value. This parameter considers the product of two terms. First, the rate of residence time per length unit (dt^*/dl) is solved considering convective and diffusive contributions (Equation 4.B.2 and Equation 4.B.2). Second, $dl/d\phi$ is obtained from the spatial gradient of ϕ as projected along the direction defined by the velocity field i.e. a mixing trajectory.

CHAPTER 5

Soot production

This chapter comprises the study of soot production in Diesel sprays under engine-like conditions. Following the work presented in Chapter 4, here the ECN Spray A reference condition is used as the baseline case from which spray reactivity and mixing parametric variations are later carried out and analyzed. In this regard, this chapter starts with a preliminary assessment of the capabilities of the Gokul soot model focusing on the influence that a one-way or a two-way coupling of the gas phase and soot has on spray combustion. For the description of fuel oxidation, the chemical mechanism proposed by Narayanaswamy et al. [216] is used throughout this chapter. Regarding TCI, the WM model and the UFPV model are thoroughly analyzed in terms of soot production and results are validated with experimental data available through the ECN [28]. Lastly, the UFPV model is used for the study of spray reactivity and mixing parametric variations. Within the UFPV framework, flamelet calculations were carried out using the flamelet code developed at ANL [219].

5.1. Soot model preliminary assessment

The soot modeling approach in this work is centered in the use of a two-equation soot model. In particular, the WM and the UFPV combustion models are coupled to the Gokul model [168]. The soot-gas phase coupling is one-way with the WM model and two-way with the UFPV model in terms of whether or not species consumption through soot subprocesses are taken into account in the gas phase.[1]

[1] A full description of the combustion and soot modeling approaches can be found in Chapter 3.

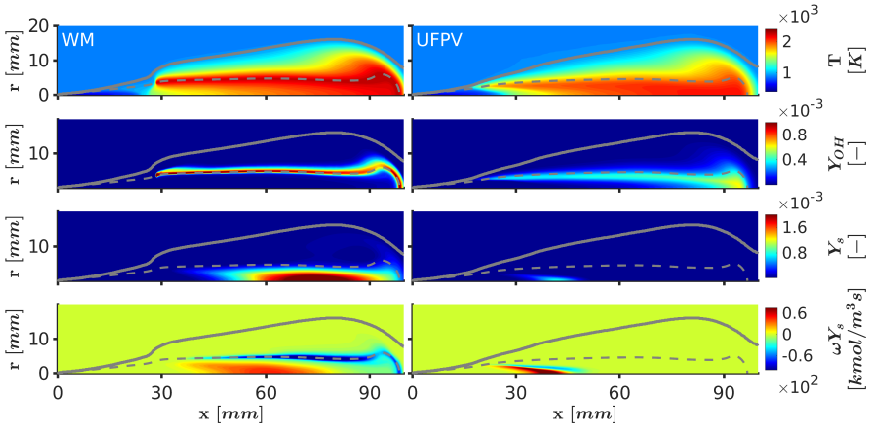

Figure 5.1: *Temperature, OH mass fraction, soot mass fraction and soot mass fraction source term at quasi-steady state using Gokul default constants for the WM (left) and UFPV (right) models. Solid and dashed gray lines plotted at the spray radius location and stoichiometric surface, respectively.*

To exemplify the influence of soot modeling and the different coupling strategies on combustion modeling, Figure 5.1 shows results for combustion-relevant variables namely, temperature and *OH* mass fraction along with the soot mass fraction and soot mass fraction source term fields predicted by the WM and UFPV models.

In contrast to WM results, where maximum temperatures are seen around the stoichiometric surface (gray dashed line), UFPV results with the two-way coupling between the gas phase and soot show a shift of maximum temperatures toward the spray fuel-rich core. From the flame structure analysis in Chapter 4 under Subsection 4.3.2 it was seen that the UFPV model predicted *OH* to be located around the stoichiometric surface thus confirming that the location shift toward fuel-rich mixtures is induced by the soot-gas phase interaction. This feature is clearly seen in the *OH* mass fraction field (Figure 5.1) where the high-concentration zone is seen at 90 *mm* at the spray axis for the UFPV model while for the WM model *OH* is more evenly distributed around the stoichiometric surface. As for soot, the WM model predicts its appearance at rich mixtures extending from around 30 *mm* up to the spray head beyond 90 *mm*. The UFPV model, predicts much less soot which is confined to a narrow fuel-rich region of the spray barely reaching 55 *mm*. To better understand differences in how soot is distributed within the spray, the soot mass fraction source term field is plotted in the last panel in Figure 5.1. Although soot formation is more intense in the UFPV model, soot is quickly oxidized thus confining it within the spray fuel-rich

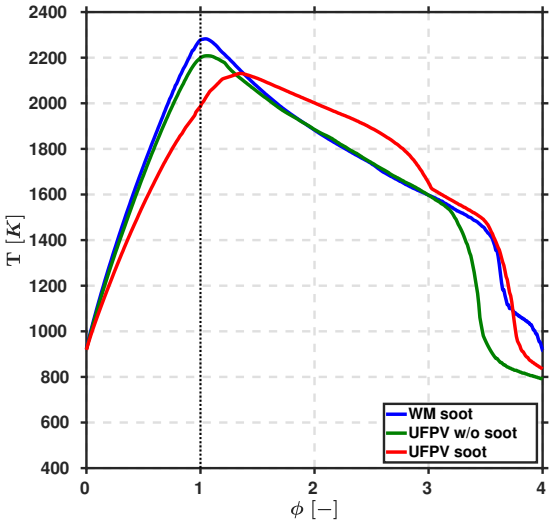

Figure 5.2: *Maximum temperature and mean equivalence ratio at quasi-steady state for the WM model and UFPV models with and without soot modeling using Gokul default constants. Dashed vertical line plotted at stoichiometric equivalence ratio.*

inner core. WM model results show less intense soot formation but more intense soot oxidation which, unlike UFPV results, is seen to take place around the stoichiometric surface.

To further illustrate implications of the different combustion-soot modeling implementations, maximum temperature at mean equivalence ratio[2] is plotted in Figure 5.2. This time, UFPV results without soot modeling are included as reference. The $\phi - T$ representation is consistent with the temperature field depicted in Figure 5.1 where it was already inferred that peak temperatures for the two-way coupling UFPV model were shifted toward rich mixtures. Moreover, the inclusion of reference UFPV model results without soot modeling confirms that the temperature shift is indeed a consequence of the interaction between the gas phase and soot.

Since the gas phase and soot interaction takes place at flamelet level, closer attention is paid to how soot modeling affects combustion at this level. Figure 5.3 depicts results for the transient evolution at two time instants and the steady solution for a reference flamelet with $\chi_{st} = 9.324\ 1/s$. At 0.6 ms, results for the soot precursor $A4$, C_2H_2 and temperature match for the cases with and without soot modeling. At this time, no $A4$ has been

[2]The maximum temperature is retrieved from equivalence ratio bins.

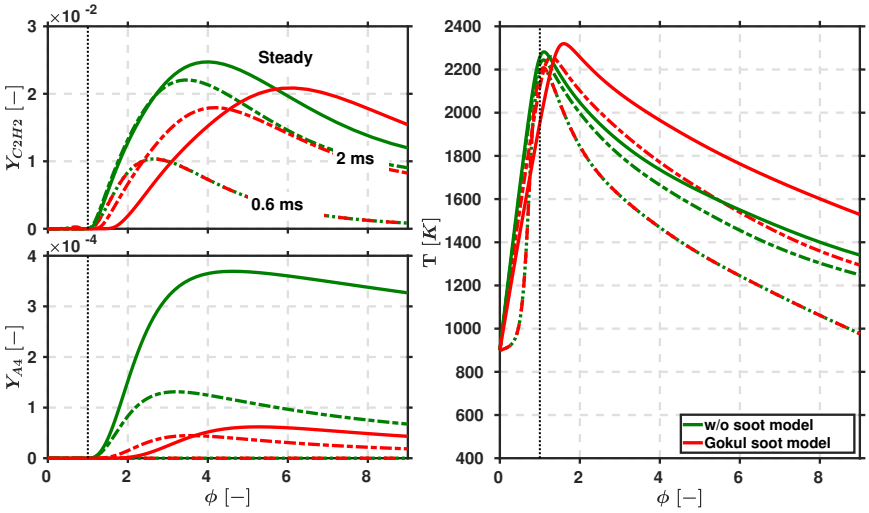

Figure 5.3: *Flamelet results (χ_{st} = 9.324 1/s) for the transient evolution of C_2H_2 mass fraction, A4 mass fraction and temperature with and without soot modeling using Gokul default constants. Dashed vertical line plotted at stoichiometric equivalence ratio.*

produced hence no soot inception has taken place and no C_2H_2 has been consumed through surface growth. At 2 *ms*, less amount of *A*4 is seen for the case with soot modeling as part of this species has been consumed into soot nuclei. Similarly, less amount of C_2H_2 is also seen as this species has been consumed through surface growth. With the consumption of both *A*4 and C_2H_2 the temperature shifting starts to gain relevance. At steady state, the temperature profile for the case with soot modeling peaks at rich mixtures consistently with the previous observation in the CFD results. It is then evident that the soot-gas phase two-way coupling, with the consequent consumption of soot-relevant species, induces the shift of combustion toward rich mixtures.

Results shown up until this point evidence that default constants for the Gokul model are not suitable for the UFPV model using a two-way coupling. Thus, a new set of constants are proposed as described in Section 3.3. Flamelet results for the proposed set of constants and for the reference case without soot modeling are shown in Figure 5.4 for the same flamelet used in Figure 5.3. From the steady flamelet results for *OH* and combustion major species namely, *CO*, CO_2 and H_2O it can be observed that unlike the case with default soot constants in the Gokul model, where the consumption of species by the soot model induced a strong shift toward rich mixtures, the

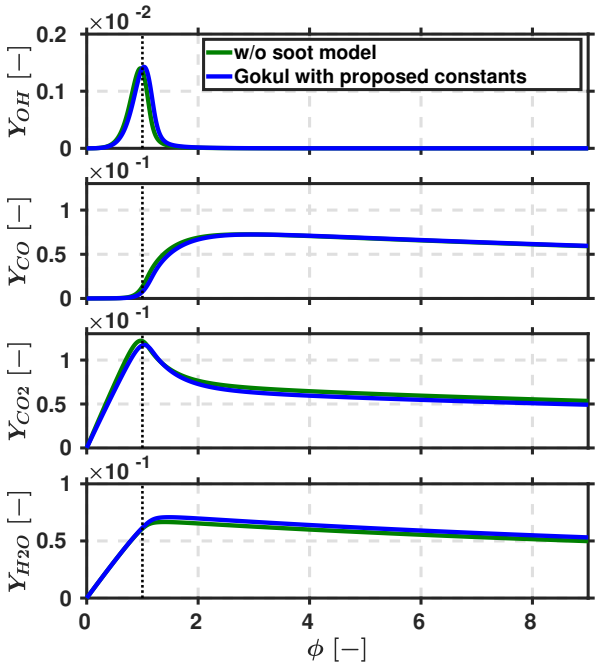

Figure 5.4: *Flamelet results ($\chi_{st} = 9.324\ 1/s$) at steady state for OH, CO, CO_2 and H_2O mass fraction with and without soot modeling using the Gokul model with proposed constants. Dashed vertical line plotted at stoichiometric equivalence ratio.*

set of proposed constants seems to be more in line with results from the reference case without soot modeling with OH, CO_2 and H_2O peak values and CO onset point around $\phi = 1$. In the next sections, results for both the WM with one-way coupling using default soot constants and the UFPV with two-way coupling and proposed constants will be further analyzed.

5.2. Analysis of the reference condition

Throughout this section, soot results from the WM model and the UFPV model are validated for the Spray A reference condition (full description of injection and thermodynamic conditions in Table 3.1). One-way coupling WM model results were obtained using default constants for the Gokul model. UFPV model results on the other hand, were obtained with the two-way coupling using the proposed set of constants reported in the previous section. For validation purposes, Figure 5.5 comprises a comparison of the optical thickness (KL) field from the experimental measurements and

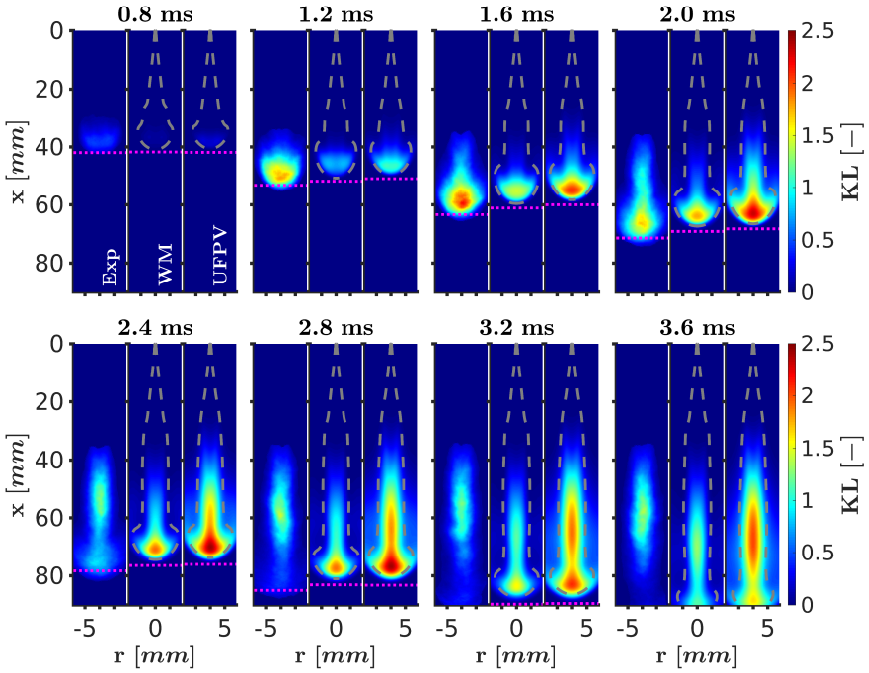

Figure 5.5: *Optical thickness for the WM model with default Gokul constants and UFPV with proposed constants for the Gokul model. Dashed gray line marks the stoichiometric surface and dotted horizontal line marks the spray tip penetration.*

from the CFD simulations which was computed trough soot volume fraction (SVF) forward Abel transformation. SVF and soot mass experimental results for the reference condition are reported in [78] where experiments where conducted in a constant pressure combustion vessel fed with a stream of O_2 and N_2.

The sequence depicted in Figure 5.5 comprises the transient evolution of KL from its early detection in the experiment around 0.8 *ms* to 3.6 *ms* time at which the experimental data has reached the quasi-steady state. For reference, a dashed pink line is drawn to mark the spray tip penetration for both the experimental and CFD cases. For these latter, the stoichiometric surface is also included in the figure with a dashed gray line. At 0.8 *ms* soot is detected in the experiment near the spray head. With the progression of time, measured KL value increases with a peak at 1.6 *ms* after which it seems to remain stable. In terms of structure, the measured KL cloud seen at 0.8 *ms* evolves into a mushroom-shaped structure at 2 *ms*. Beyond this time, the head of the mushroom-shaped structure seems to be detached (visible at

2.4 *ms*) and quickly dissipated, giving place to an ellipse-shaped structure barely unchanged beyond 2.8 *ms*. As for the CFD results, at 0.8 *ms* there is virtually no soot compared to the measured value in the experiments. At this time, 365 μs have passed since the ignition delay time in the experiment, but only 174 μs and 255 μs have passed since their respective ignition delay times for the WM and UFPV models, respectively. The over-prediction in ID is consistent with the delay in the appearance of soot and a shorter tip penetration (already discussed in the previous chapter). Qualitatively, both models reproduce the transient behavior seen in the experiment. First, the soot cloud forms at the fuel-rich head of the spray. Then the soot cloud transitions into a mushroom-shaped structure whose head eventually detaches and dissipates, point at which the ellipse-shaped soot structure becomes quasi-steady. The transient evolution in the CFD cases is slower compared to the experiment. In fact, while measured KL seems to reach quasi-steady state at 2.8 *ms* the CFD results show that at 3.6 *ms* the spray has not yet reached this state. In terms of spatial distribution, qualitatively the measured KL distribution seems to fall between WM and UFPV results in the radial direction while both models over-predict the extension of the soot cloud. At 3.6 *ms* the WM model predicts a narrow soot structure contained within the stoichiometric surface while the UFPV model predicts a broader soot structure beyond the limit of the stoichiometric surface.

Derived from KL measurements, Figure 5.6 shows the instantaneous total soot mass from the experiment (solid black line) and CFD cases. It is worth mentioning that the experiment field of view (FOV) is limited to a 20×90 *mm* window, so in order to make a fair comparison, soot mass from the CFD cases has been integrated within a region of interest that match the experiment FOV dimensions. From the experimental data, it is seen how soot starts appearing some time after ID to continuously grow up until 1.9 *ms*. Beyond this time, soot mass gradually drops until approximately 3 *ms*. At this time the spray is out of the FOV, but the main soot structure has reached quasi-steady state and is fully located within the FOV as can be seen at 3.2-3.6 *ms* in Figure 5.5.

On the CFD side, some of the features already inferred from the comparison of the optical thickness field are also observed when comparing soot mass data. For instance, longer ignition delay time for both CFD cases contributes to longer soot onset time compared to the experiments. Both, WM and UFPV models predict a slower soot mass growth process that extends until the time (approximately 3 *ms*) at which the spray leaves the region of interest causing a small drop in soot mass (between 3.5-5 *ms*) after which it reaches

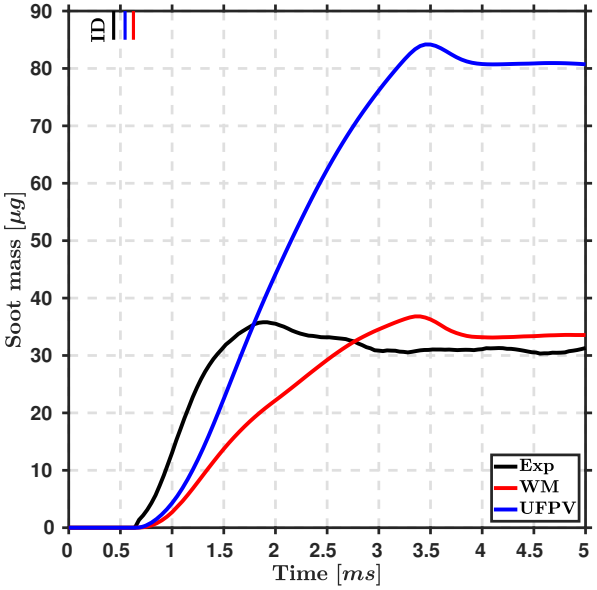

Figure 5.6: *Integrated soot mass for the WM model with default Gokul constants and UFPV with proposed constants for the Gokul model. Vertical line marks ignition delay time.*

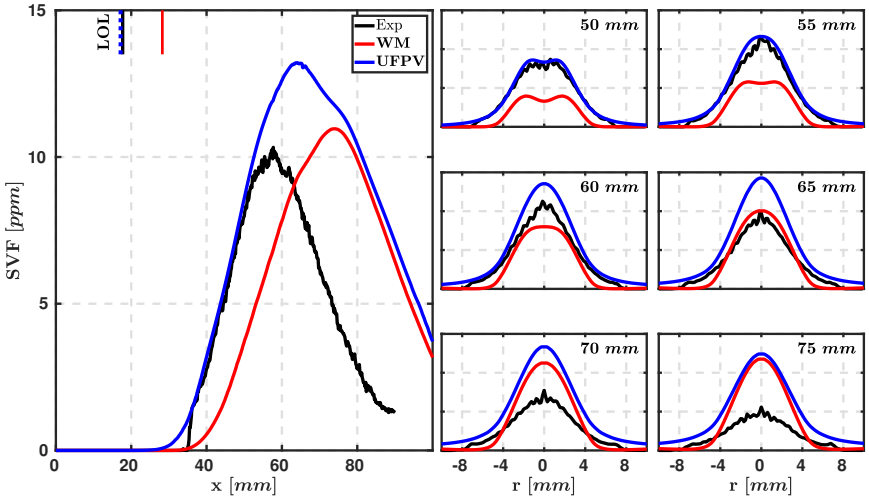

Figure 5.7: *Soot volume fraction axial and radial profiles at quasi-steady state for the WM and UFPV models. Vertical line marks lift-off length location.*

quasi-steady state. Between both CFD cases, the WM model predicts a slower initial soot mass ramp-up and in contrast it predicts a quasi-steady soot mass amount closer to the experiment in comparison to the UFPV model. This last observation is consistent with a narrower soot structure as already seen in Figure 5.5. To analyze soot spatial distribution in more detail, Figure 5.7 shows soot volume fraction profiles at quasi-steady state. KL measurements have been averaged (between 3.4-5-4 *ms*) and deconvolved to obtain the SVF field. The panel to the left shows the SVF profile along the spray axis with vertical lines marking the LOL position. Panels to the right show axial profiles from 50 to 75 *mm*.

Differences in LOL (UFPV results matches experimental data while WM results over-predict it) are consistent with the lag observed in the SVF axial profile. The excellent agreement for the UFPV model (up until 55 *mm*) is also the result of the soot surface growth pre-exponential factor choice. Radial profiles (right-hand side in Figure 5.7) show that not only the ramp-up is well captured by the UFPV model, but also the SVF field width. Further downstream from 55 *mm*, both peak value and width are over-predicted with the consequent over-prediction of soot mass seen in Figure 5.6. As for WM model results, the SVF profile is under-predicted up until 63 *mm* and over-predicted downstream this point with radial profiles narrower than its experimental counterpart at any location.

It is worth emphasizing that although soot mass results might match experimental data, the way in which this mass is distributed within the spray might not be as accurately predicted and vice-versa. Such is the case of the WM and UFPV results. On the one hand, the WM model is able to capture soot mass amount at quasi-steady state, but it fails to predict its spatial distribution. The UFPV model on the other hand, offers a better description of the spatial distribution of soot (limited to the ramp-up region) while failing to predict the total soot mass in the spray at quasi-steady state.

The full picture in terms of soot spatial distribution can be seen in Figure 5.8). The experimental data, WM and UFPV results are depicted along with a dashed pink line marking the LOL location. Additionally, for the CFD results the dashed line marks the stoichiometric surface, the outer gray line marks the spray radius and the inner gray lines mark mixing trajectories. Labels 1 and 2 are used to highlight reference mixing trajectories[3] that will later be used for further analysis. This figure summarizes key aspects on

[3]Mixing trajectory 1 and 2 originate at 5% and 25% of the spray width at 70% of the spray tip penetration following the same criteria introduced in Chapter 4.

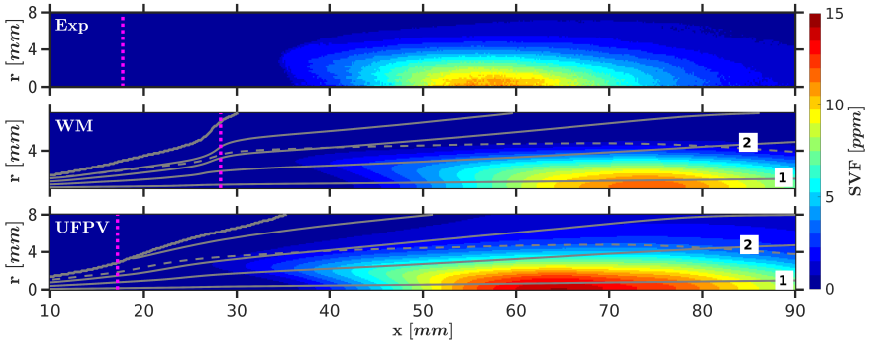

Figure 5.8: *Soot volume fraction field at quasi-steady state for the experimental measurement, WM and UFPV models. Vertical line marks lift-off length location. For CFD results, spray radius, stoichiometric surface and mixing trajectories are also included. Reference mixing trajectories are labeled as mixing trajectory 1 (closest to spray axis) and mixing trajectory 2.*

soot spatial distribution prediction with radially narrower and broader (for the WM and UFPV models results, respectively) soot structures which are also longer compared with the experimental data.

Soot mass fraction, soot mass fraction source term, temperature, $A4$ (increased by a 300 factor) and C_2H_2 mass fraction are plotted along reference mixing trajectories in Figure 5.9. Panels on top, depict results along mixing trajectory 1 (closest to the spray axis) and panels on the bottom part depict results for mixing trajectory 2. Soot mass fraction results (solid line on the left-hand side panels) are consistent with differences in LOL i.e. shorter LOL for the UFPV case enables soot to be produced at richer mixtures compared to the WM case. The soot mass fraction source term (dotted line on the left-hand side panels) shows how both models start producing soot at rich mixtures, then soot is transported toward leaner mixtures to be oxidized around the stoichiometric surface where its source term becomes negative.

In terms of flame structure (panels on the right), the WM and UFPV models predict similar results for temperature and C_2H_2 near the spray axis (top panel) although differences arise for the radially displaced mixing trajectory 2 (bottom panel). On the contrary, $A4$ profiles show noticeable differences in either mixing trajectory with much less $A4$ predicted for the WM model compared with the UFPV model. An interesting feature is that the equivalence ratio onset value and even the shape of $A4$ mass fraction profiles match those of the soot mass fraction source term. Thus, it should be

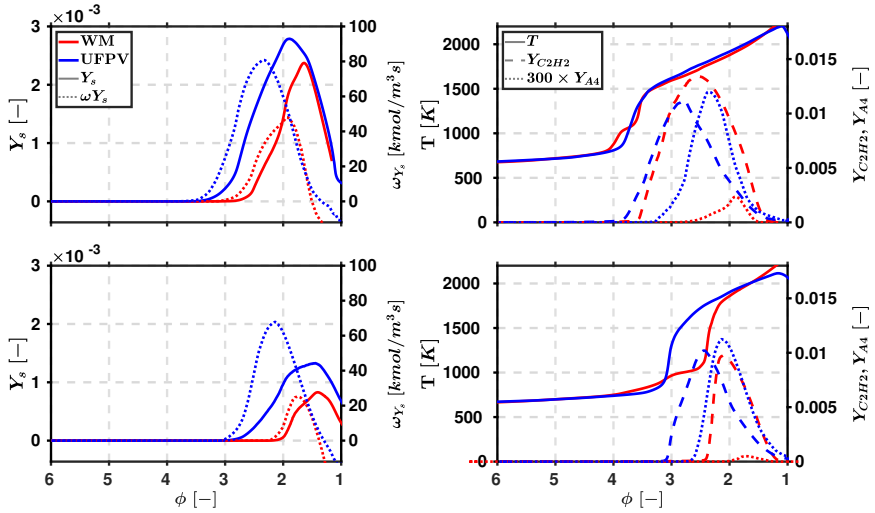

Figure 5.9: *Soot mass fraction, soot mass fraction source term, temperature, C_2H_2 mass fraction and A4 mass fraction (increased by a factor of 300) at quasi-steady state along reference mixing trajectories. Top panel corresponds to results along mixing trajectory 1 while the bottom panel corresponds to mixing trajectory 2.*

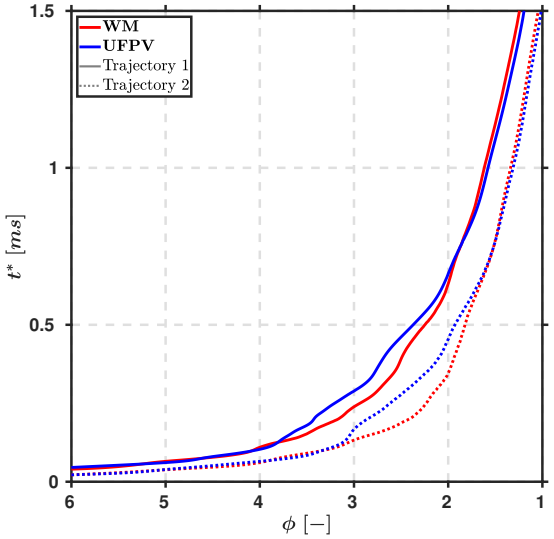

Figure 5.10: *Residence time at quasi-steady state along reference mixing trajectories for the WM and UFPV models. Solid lines correspond to results along mixing trajectory 1 (closest to spray axis) while dotted lines correspond to mixing trajectory 2.*

emphasized that the precursor species is critical for the spatial distribution as it plays a key role on the soot mass fraction source term despite its much less relevance in terms of total soot mass produced.

Besides variables with inherent relevance for soot production such as temperature, species precursor ($A4$) and species responsible for soot surface growth (C_2H_2), the residence time, introduced in Chapter 4 as a variable of paramount importance for combustion, is unequivocally important for soot production as well. To illustrate its relation to soot production, Figure 5.10 shows this variable integrated along the same reference mixing trajectories from Figure 5.9. Between CFD cases, differences for either mixing trajectory are mostly negligible with the exception of equivalence ratios around the LOL. In terms of differences among mixing trajectories, the closest one to the axis (mixing trajectory 1) exhibits a longer residence time thus any "gas particle" moving along this path is more prone to produce soot since the high-temperature region takes place at richer mixtures with the consequent production of $A4$ and C_2H_2 at richer equivalence ratios in contrast to a radially displaced mixing trajectory shown to produce less soot (Figure 5.9 bottom).

Contributions to soot production from the different soot subprocess can be qualitatively assessed by comparing Figure 5.11 and Figure 5.12 for the WM model and the UFPV model, respectively. First, it is observed that source term peak values from subprocesses contributing to the increase in soot mass (nucleation and surface growth) occur upstream from the location of the soot mass fraction peak for both combustion models as it was already inferred from Figure 5.9. In this same matter, by taking a look at the magnitudes from nucleation and surface growth source terms it is clear that the latter is the most relevant contributor to soot mass. If now the focus is placed on differences among combustion models, the most noticeable one corresponds to the magnitude of the surface growth step. In relation to the oxidation source terms, the different species considered yield to the oxidation of soot in the vicinity of the stoichiometric surface. Oxidation through O_2 is within the same order of magnitude for the WM and the UFPV models while the OH oxidation source term shows a noticeable difference in its peak value. As for the oxidation step through O (only accounted for in the UFPV model) it is relegated to a minor contribution to soot oxidation. Between the WM model and the UFPV model, differences in order of magnitude for surface growth and oxidation through OH are expected based on the different reaction rate factors discussed in Chapter 3.

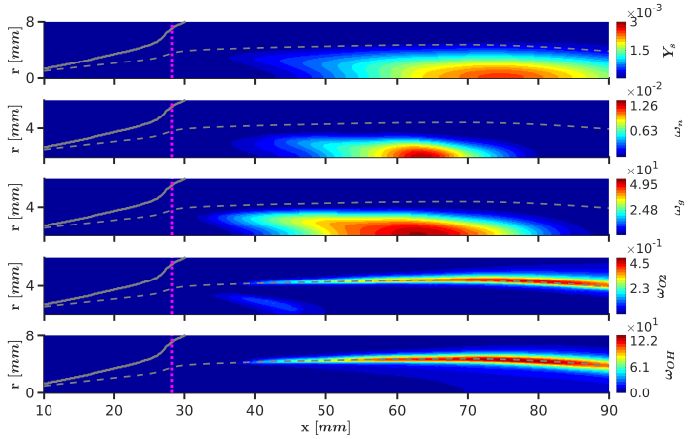

Figure 5.11: *Soot mass fraction and subprocesses source term fields at quasi-steady state for the WM model. Source terms in units of $kmol/m^3s$. Solid and dashed gray lines plotted at the spray radius location and stoichiometric surface, respectively. Vertical line marks lift-off length location.*

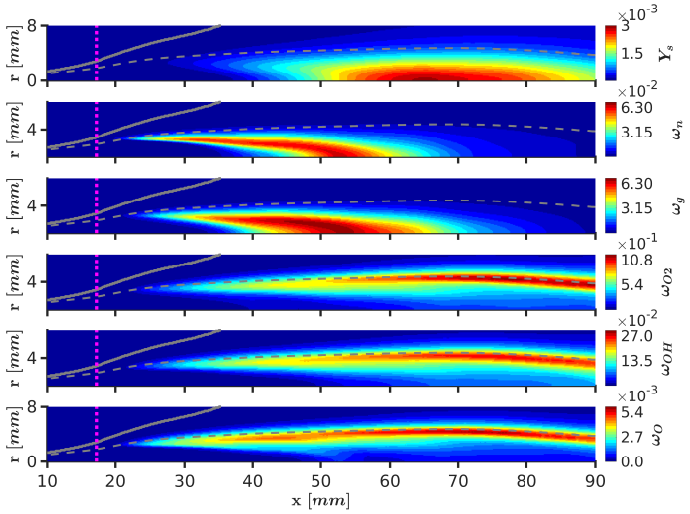

Figure 5.12: *Soot mass fraction and subprocesses source term fields at quasi-steady state for the UFPV model. Source terms in units of $kmol/m^3s$. Solid and dashed gray lines plotted at the spray radius location and stoichiometric surface, respectively. Vertical line marks lift-off length location.*

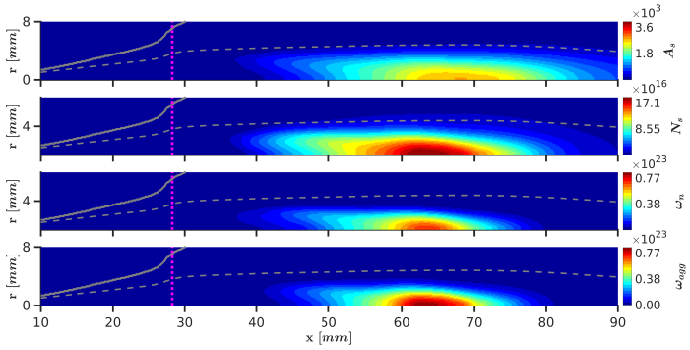

Figure 5.13: *Soot surface area, number density and source term fields at quasi-steady state for the WM model. Units are of* $1/m$, $particles/kg$ *and* $particles/m^3s$, *respectively. Solid and dashed gray lines plotted at the spray radius location and stoichiometric surface, respectively. Vertical line marks lift-off length location.*

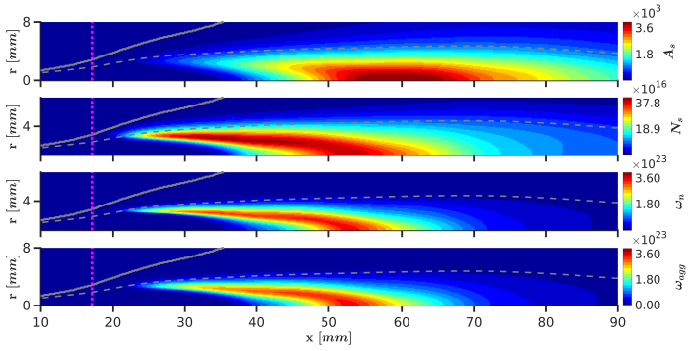

Figure 5.14: *Soot surface area, number density and source term fields at quasi-steady state for the UFPV model. Units are of* $1/m$, $particles/kg$ *and* $particles/m^3s$, *respectively. Solid and dashed gray lines plotted at the spray radius location and stoichiometric surface, respectively. Vertical line marks lift-off length location.*

Lastly, Figure 5.13 and Figure 5.14 depict fields relevant to the number of soot particles produced. Top panels show results for the soot surface area which is a function of the soot mass fraction and number density (see Subsection 2.3.2). This variable is relevant for surface subprocesses (surface growth and oxidation) show an ellipse-shaped distribution for both combustion models (WM results in Figure 5.13 and UFPV results in Figure 5.14) similar to that of the soot volume fraction field. Soot number density and its source terms (nucleation and agglomeration) however, show differences

among combustion models. For the WM case, the zone of high concentration of particles near the spray axis coincides with the zone of large soot surface area. For the UFPV case, the zone of high concentration of particles is radially displaced toward the stoichiometric surface close to the LOL location and it is closer to the spray axis further downstream.

Similarities in the ellipse-shaped soot volume fraction structure seen for both combustion models in Figure 5.8 seem to indicate that soot surface area has a more predominant role than the number of particles itself. In this regard, the soot surface (function of Y_s and N_s) available for surface growth and oxidation is more relevant for soot production than the number of particles.

5.2.1. Soot model sensitivity analysis

From the previous subsection it is clear that UFPV model results show the best agreement in terms of soot distribution within the spray. Nevertheless, this agreement is limited to the ramp-up region up until approximately 55 *mm*. Further downstream, soot volume fraction is over-predicted with higher peak values and wider radial profiles compared to experimental data and the consequent over-prediction of soot mass. Two sources of uncertainty are assessed in order to shed some light on how results might be improved.

First, the soot oxidation subprocess. Having fitted the soot surface growth pre-exponential factor to target the experimental SVF field, the oxidation source term is modified seeking to overcome the over-prediction in SVF (downstream 55 *mm*) and soot mass observed in Figure 5.6 and Figure 5.7. Thus, the net oxidation source term i.e. the combined contribution from O_2, OH and O is increased by a factor of 2.5.

Results for the integrated soot mass are shown in Figure 5.15. Fitting the oxidation source term has the potential to match the experimental value at quasi-steady state while not changing the ID time (vertical line drawn at ID time fall on top of each other). As for spatial distribution, the 2.5 increase in the oxidation source term improves SVF results along the spray axis (left-hand side panel in Figure 5.16), retaining the good agreement in the ramp-up region (vertical lines marking LOL location also remain unchanged) and enhancing the agreement downstream 55 *mm* although SVF is still over-predicted at these locations. Radial profiles (right-hand side panels in Figure 5.16) also show that, as might be expected, the oxidation source term not only acts axially but radially. The improved agreement in soot mass and SVF axial profile comes at the expense of narrower SVF radial profiles at any location compared to experimental data.

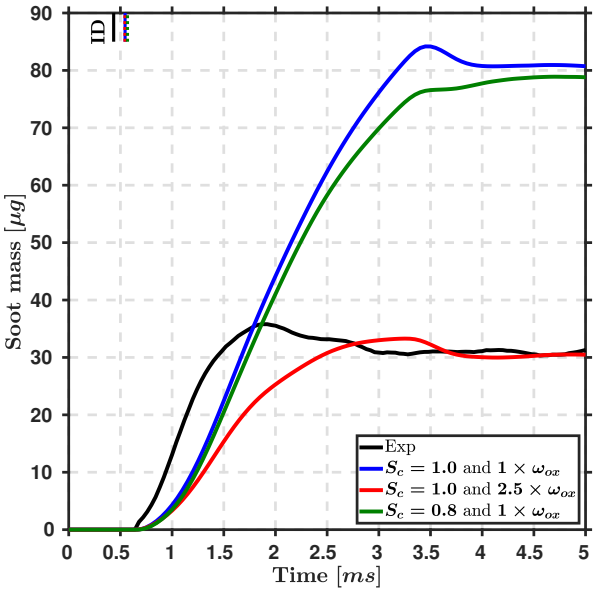

Figure 5.15: *Integrated soot mass sensitivity to soot oxidation rate and turbulent Schmidt number for the UFPV model. Vertical line marks ignition delay time.*

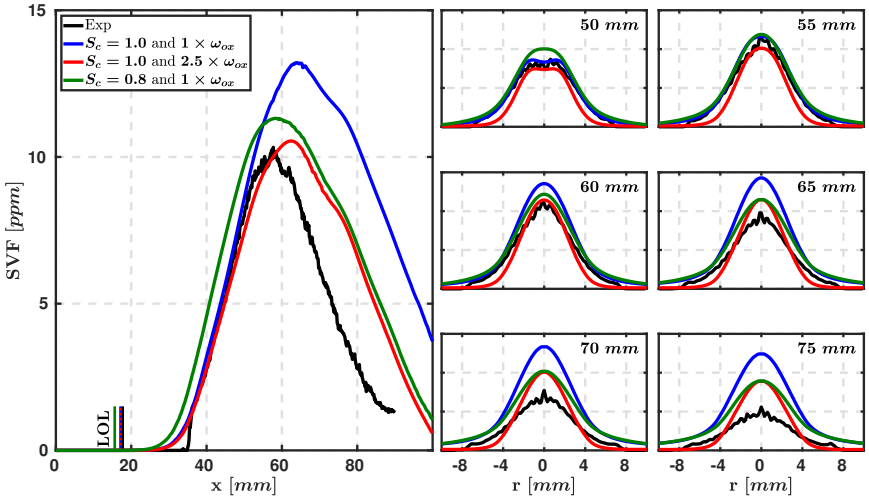

Figure 5.16: *Soot volume fraction axial and radial profiles sensitivity to soot oxidation rate and turbulent Schmidt number for the UFPV model at quasi-steady state. Vertical line marks lift-off length location.*

The second source of uncertainty assessed is the mixing field. Although results for the mixture fraction and its variance were validated under inert conditions in Section 4.1, there is no experimental data available for reacting conditions. Thus, validation of reacting results in terms of mixing is limited to the velocity field as discussed in Section 4.2. However, the flame length derived from experimental natural luminosity data can be used as a qualitative indicator of where the flame front might be located. Figure 5.17 shows that with the default computational setup, the flame front (marked by the furthest location of the stoichiometric surface) has not stabilized by the end of the injection at 5 *ms*. On the contrary, from the experimental data it is inferred that at 4.5 *ms* the flame front is already stabilized. An over-prediction of the flame length as observed in Figure 5.17 is in line with the over-prediction of the furthest location at which soot is found within the flame. Thus, to assess soot results sensitivity to changes in the mixture fraction field, the turbulent Schmidt number[4] (S_c) is decreased from 1.0 (default value used in this work) to 0.8 yielding to a better agreement for the flame length at quasi-steady state despite the under-prediction at earlier times.[5]

The decrease in S_c induces a minor reduction in soot mass and a minor increase in ID (Figure 5.15). Spatially, setting $S_c = 0.8$ slightly shifts the SVF axial profile and LOL location toward the nozzle (Figure 5.16). Such shift is accompanied by a decreased peak value although the good agreement in the ramp-up region is lost and the over-prediction at locations beyond 55 *mm* still remains. Radially, the profiles width doesn't change in comparison to the case with $S_c = 1.0$ consistently with the minor reduction in soot mass observed in Figure 5.15. Based on the results in Figure 5.15 and Figure 5.16 it seems that within the context of RANS simulations, there is limited margin for reasonable adjustment of parameters that might improve the agreement with experimental results. Notwithstanding, it is worth highlighting that results presented in this section point toward the need of an improved description of the mixing process under reacting conditions. Changes in soot results observed for the change in S_c evidences that soot production is sensitive to the residence time[6] thus proving the importance of the treatment

[4]The turbulent Schmidt number allows for the evaluation of changes in the mixture fraction field while not altering the velocity field which has been validated against experimental data.

[5]The flame length under-prediction is consistent with tip penetration results discussed in Section 4.2 in Chapter 4.

[6]Changes in S_c induce a spatial shift in the mixing field while maintaining the velocity field unaltered thus changing the residence time.

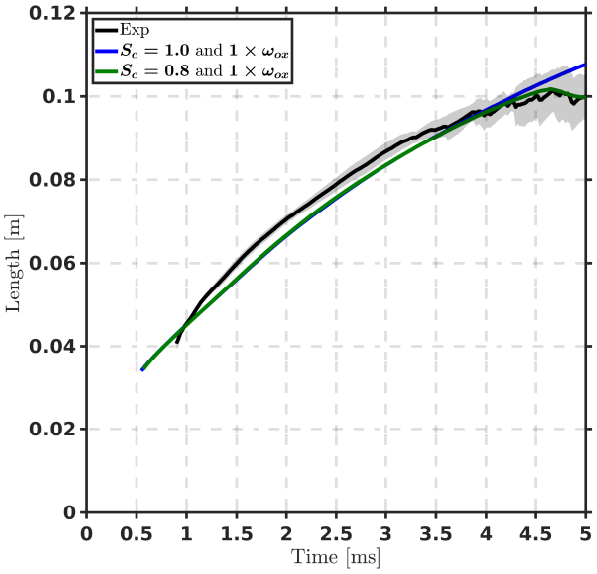

Figure 5.17: *Flame length sensitivity to turbulent Schmidt number for the UFPV model.*

of turbulence, hence mixing. Finer quantitative agreement for soot data needs an improved description of turbulence-mixing interaction for which large eddy simulations (LES) might be suitable. Moreover, sensitivity of soot production to different chemical mechanism might also contribute to the task of improved agreement. However, such task is out of the scope of this work which main focus, as stated in Chapter 1, is placed over the study of soot production and its relationship with variations in spray reactivity and mixing boundary conditions. These are studied in the following sections using the two-way UFPV approach maintaining the default computational setup used for the reference case. Besides good general agreement for combustion global parameters reported in Section 4.2, the use of the UFPV model for the study of boundary condition parametric variations is also supported by lower computational cost compared to the use of the WM model. For instance, the computational cost of running the UFPV model with the Yao or Narayanaswamy mechanism with 12 cores ranges between 39 to 96 *h*. For the WM model the cost of running a case with the Yao mechanism ranges between 83 to 246 *h* with 24 cores and between 991 to 1813 *h* for the Narayanaswamy mechanism with 28 cores.

5.3. Effect of mixture reactivity

The Spray A reference condition is used along this section as the reference case to study soot production sensitivity to changes in the spray reactivity boundary conditions. The acronyms nonEGR and EGR refer to O_2/N_2 and $O_2/N_2/CO_2/H_2O$ ambient compositions, respectively. Besides the nonEGR Spray A reference condition (labeled as "SA Ref"), three additional cases are included namely, a reference condition EGR case ("SA EGR"), a low-oxygen concentration EGR case ("13%X_{O_2}") and a high-temperature nonEGR case ("SA 1000K"). A full description of thermodynamic conditions is reported in Table 5.1.

Table 5.1: *Thermodynamic conditions for the spray reactivity parametric variations.*

	SA 13%X_{O_2}	**SA EGR**	**SA Ref**	**SA 1000K**
Ambient Temperature	900 K	900 K	900 K	1000 K
Ambient composition				
X_{O_2}	0.13	0.15	0.15	0.15
X_{N_2}	0.7709	0.7515	0.85	0.85
X_{CO_2}	0.0626	0.0622	0	0
X_{H_2O}	0.0364	0.0362	0	0

Nozzle No 210370 for the EGR cases and 210675 for the nonEGR cases.

The study of soot production with different ambient compositions (EGR and nonEGR cases) is particularly relevant within the context of the ECN where different experimental facilities are used by several contributors around the world. For instance, experimental data from the reference and higher ambient temperature conditions ("SA Ref" and "SA 1000K") was obtained in a constant pressure vessel with only O_2 and N_2 in the ambient composition [78] as described in Section 5.2. Nonetheless, the same experiments have been carried out at Sandia National Laboratories (SNL) with identical injection and thermodynamic conditions in a constant volume vessel in which CO_2 and H_2O are also part of the ambient composition [28] which is the case for the "13%X_{O_2}" and "SA EGR" conditions. Recently, dedicated experiments have been conducted to study the effect of the addition of CO_2 and/or H_2O on soot showing that either one contributes to a reduction of its production [232].

To start the analysis, Figure 5.18 shows the flame structure for the four cases that compose the study of the effect of mixture reactivity variations. Panels on the left depict color-coded images with mass fraction of CH_2O in blue, OH in red and the soot precursor $A4$ in green normalized with the

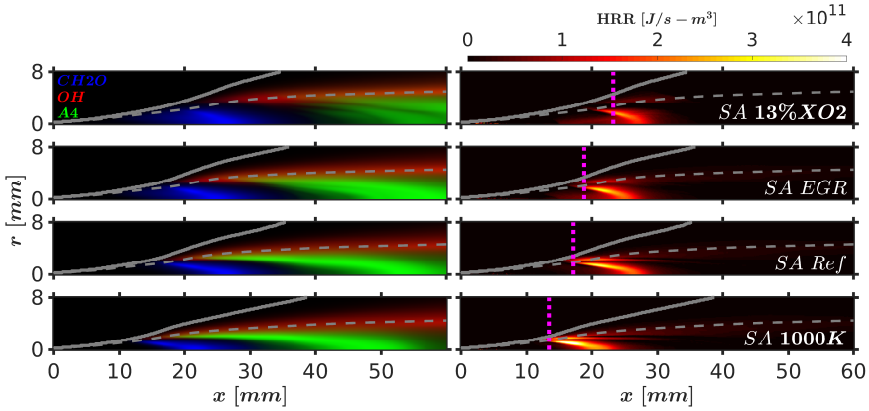

Figure 5.18: *Normalized species mass fraction and local HRR at quasi-steady state for the spray reactivity parametric variations. Solid and dashed gray lines plotted at the spray radius and stoichiometric surface location, respectively. Vertical line marks lift-off length location.*

corresponding maximum concentration. Panels on the right, depict the local heat release rate along with the LOL location (vertical pink line). In both panels, the spray radius (solid gray line) and stoichiometric surface (dashed gray line) are also included. Compared to the results in Chapter 4, the flame structure does not change drastically with the variation in ambient oxygen concentration, composition or temperature. All four cases are characterized by the presence of CH_2O at rich mixtures in the low-temperature heat release zone attached to the base of the flame, OH around the stoichiometric surface where the diffusion flame is sustained and $A4$ at rich mixtures confined within the zone where the previous two species can be found. Locally, the "13%X_{O_2}" (top panels) and "SA 1000K" (bottom panels) conditions exhibit the longest and shortest LOL, respectively, since these two cases correspond to the least and most reactive conditions studied in this section. The latter observation is also confirmed by the local HRR contours showing more intense heat release in the vicinity of the LOL for the high-temperature condition compared to the low-oxygen concentration case. Lastly, in relation to the change in ambient composition, a minor change in the LOL location is observed when comparing the "SA EGR" and "SA Ref" cases with no considerable changes in the HRR contours.

Regarding soot, the transient evolution of the optical thickness field is depicted in Figure 5.19 for the "13%X_{O_2}" case, Figure 5.20 for the "SA EGR" case and in Figure 5.21 for the "SA 1000K" case. Similarly to previous plots of this type, a dashed gray line is used for the stoichiometric surface, a pink

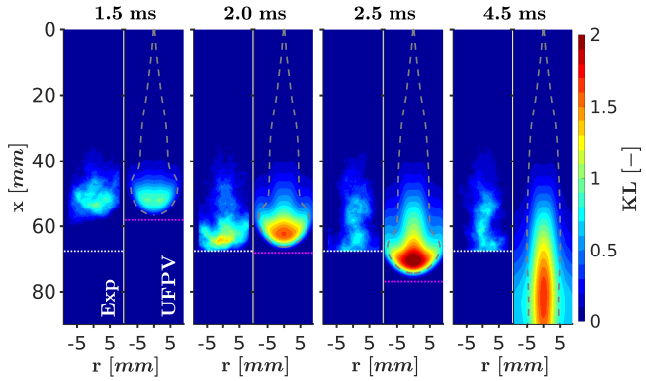

Figure 5.19: "13%X_{O_2}" *case optical thickness. Gray line marks* $\phi = 1$*, pink line marks the spray tip penetration and white line marks the experiment FOV limit.*

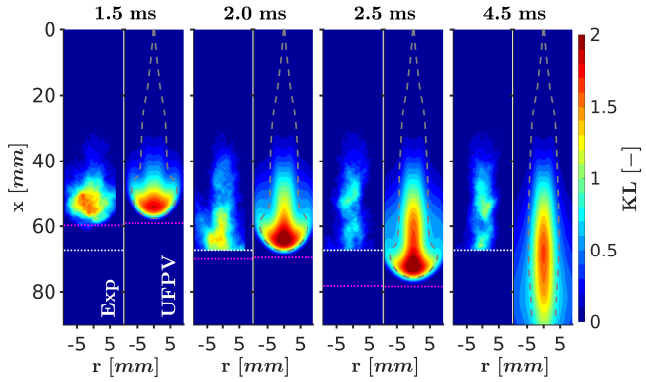

Figure 5.20: "*SA EGR*" *case optical thickness. Gray line marks* $\phi = 1$*, pink line marks the spray tip penetration and white line marks the experiment FOV limit.*

dashed line for the spray tip penetration and a dashed white line for the FOV limit. It should be noted that the color scale maximum level for the "SA 1000K" case doubles the maximum value from the "13%X_{O_2}" and "SA EGR" cases as more soot is expected for the higher temperature case due to enhanced reactivity leading to combustion of richer mixtures. For the EGR cases, lower KL values for the low-oxygen concentration condition are also expected precisely due to the reduced reactivity of the mixture. Besides the difference in maximum KL values, all three cases retain the same dynamics described for the reference condition i.e. an initial mushroom-shaped struc-

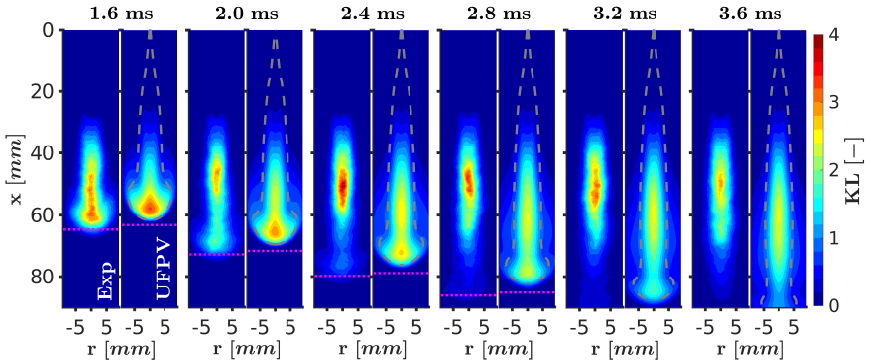

Figure 5.21: *"SA 1000K" case optical thickness. Gray line marks $\phi = 1$ and pink line marks the spray tip penetration.*

ture that transitions into an ellipse-shaped structure at quasi-steady state (last panels in Figure 5.19, Figure 5.20 and Figure 5.21). Similarities also hold true when comparing experimental and CFD results. The aforementioned transition is slower for the CFD cases and although the structure at quasi-steady state is similar, its length is larger compared to the experiment.

Differences in KL results can also be seen in Figure 5.22 (EGR cases) and Figure 5.24 (nonEGR cases) for the integrated soot mass. As mentioned earlier, experiments for the nonEGR conditions were conducted in a constant pressure vessel at CMT-Motores Térmicos [78] while measurements for the EGR conditions were carried out at SNL in a constant volume vessel [28]. The latter experiments have a smaller FOV, thus for the comparison of soot mass results the difference in FOV size from each experimental facility has been taken into account in the CFD simulations. As a result, the pronounce decrease in soot mass seen for the "13%X_{O_2}" and "SA EGR" conditions, a consequence of the spray leaving the FOV at around 2 *ms* (seen in Figure 5.19 and Figure 5.20), is reproduced in the CFD results. Then, it is also worth noting that for the EGR cases in Figure 5.22 the soot mass ramp-up is well captured even though ID is over-predicted for the low-oxygen concentration condition.[7] Nevertheless, both nonEGR cases in Figure 5.24 show a delay in the soot mass ramp-up showing that, although relevant, ID time is not the only factor controlling soot onset time and its consequent temporal evolution. The over-prediction of soot mass at quasi-steady state can be explained in more detail by analyzing the SVF profiles in Figure 5.23 and Figure 5.25 although it can already be inferred that the CFD simulation is

[7]There are two distinctive peaks in the maximum temperature time derivative data. The first peak is marked with a solid vertical line and the second peak with a dotted line.

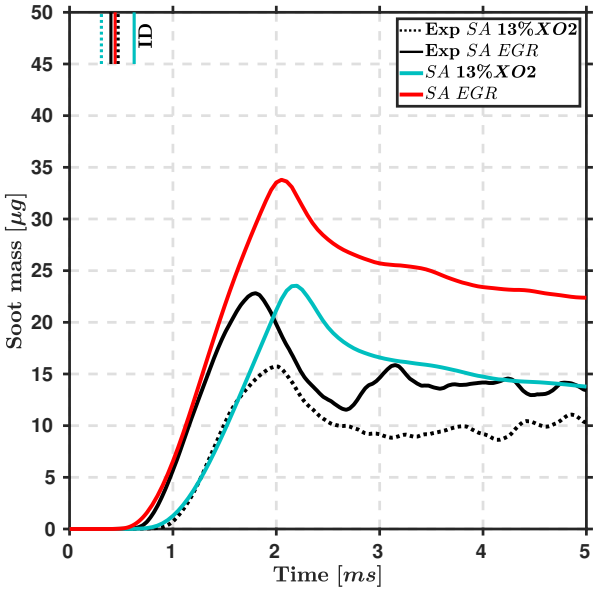

Figure 5.22: *Integrated soot mass for variations in ambient oxygen concentration using the UFPV model. Vertical line marks ignition delay time.*

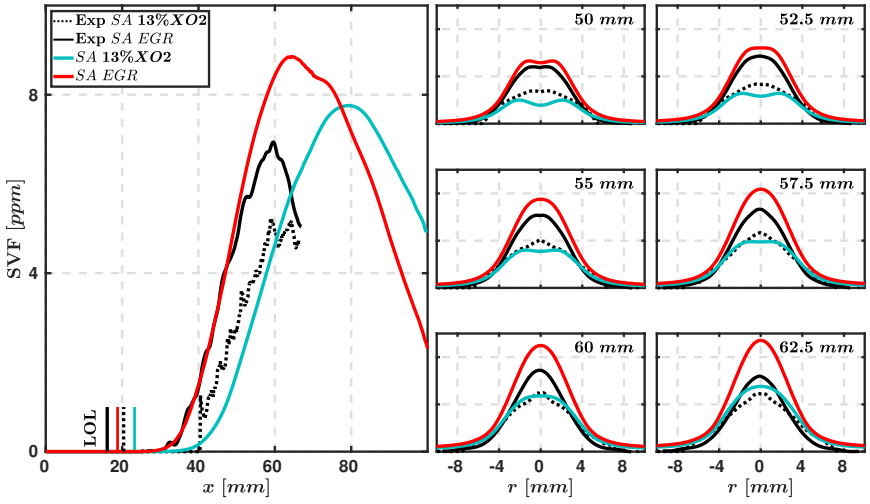

Figure 5.23: *Soot volume fraction axial and radial profiles for variations in ambient oxygen concentration using the UFPV model. Vertical line marks lift-off length location.*

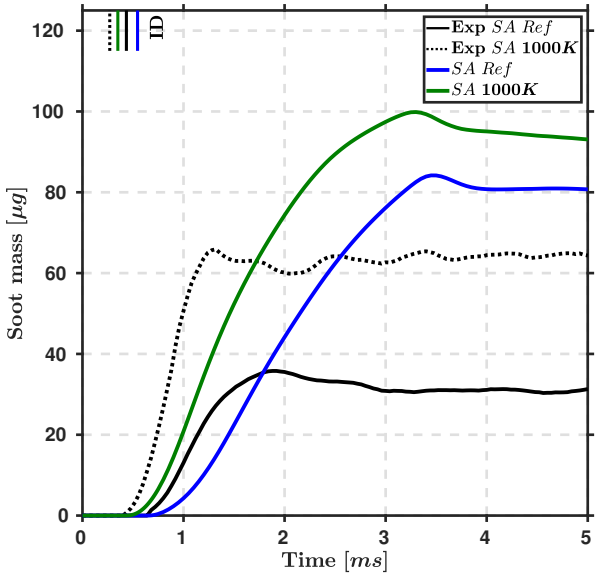

Figure 5.24: *Integrated soot mass for variations in ambient temperature using the UFPV model. Vertical line marks ignition delay time.*

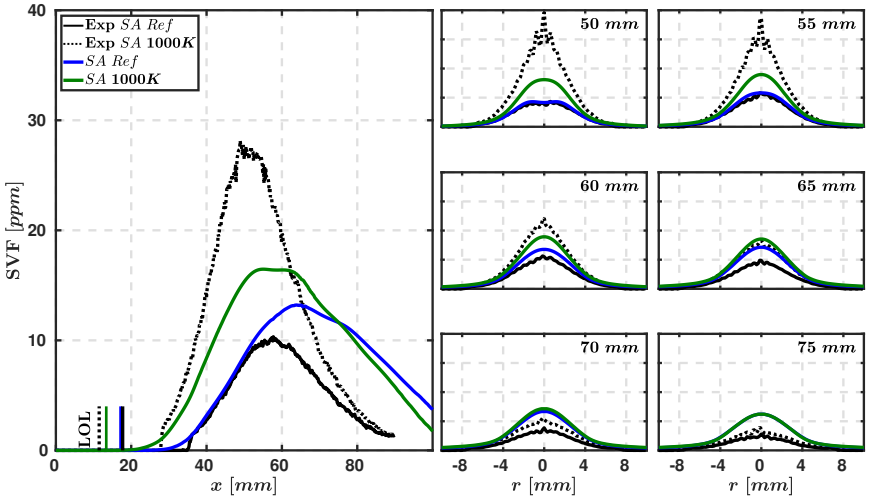

Figure 5.25: *Soot volume fraction axial and radial profiles for variations in ambient temperature using the UFPV model. Vertical line marks lift-off length location.*

less sensitive to the change in temperature compared to the experiment. In fact, while the experiment has an increase factor of 2 ("SA 1000K" case compared to the "SA Ref" case), the CFD data shows an increase factor of just 1.15.

With the decrease in ambient oxygen concentration ("13%X_{O_2}" case) or just the change in ambient composition through the addition of CO_2 and H_2O ("SA Ref" case compared to the "SA EGR" case), there's a reduction in SVF as already seen for the integrated soot mass (Figure 5.22 and Figure 5.24). The reduction in SVF is well captured by the CFD simulation. As in the case of the "SA Ref" condition, the agreement with experiments is limited to the ramp-up region where the radial profiles also show to be in agreement up until 60 *mm* in contrast to further downstream locations where profiles are wider thus causing an over-prediction of the integrated soot mass. The increase in SVF caused by the increase in ambient temperature ("SA 1000K" in Figure 5.25) is also captured by the CFD model, although the soot model seems to be less sensitive than the experiment as previously observed for the soot mass results. Consequently, neither the ramp-up in the axial profiles nor the radial profiles are well reproduced for the high-temperature condition.

It is interesting to note that in comparison to the "SA Ref" condition, the decrease in soot production with the decrease in ambient oxygen concentration or its increase due to higher ambient temperature comes with a consequent change in the LOL location (longer for the "13%X_{O_2}" condition and shorter for the "SA 1000K" condition). Nevertheless, the addition of CO_2 and H_2O within the ambient composition does not affect dramatically the LOL location although it reduces the amount of soot produced. The changes induced in soot production by the change in ambient oxygen concentration, composition and temperature can be better understood by studying relevant variables along a reference mixing trajectory[8] in Figure 5.26.

It is seen that along the reference mixing trajectory, the increase in soot mass fraction (solid lines in the top panel) with the change of ambient oxygen concentration ("13%X_{O_2}" to "SA EGR" condition), composition ("SA EGR" to "SA Ref" condition) and ambient temperature ("SA ref" to "SA 1000K") comes with an increase of the mean particle diameter (dotted line). In regard to the ambient oxygen concentration and composition, temperature profiles (solid line in the middle panel) show barely no change with 13% oxygen concentration or the addition of CO_2 and H_2O to the ambient composition which is not the case for either $A4$ (dotted line) or C_2H_2 (dashed line) mass

[8]Reference mixing trajectory originates at 5% of the spray width at 70% of the spray tip penetration following the same criteria introduced in Chapter 4.

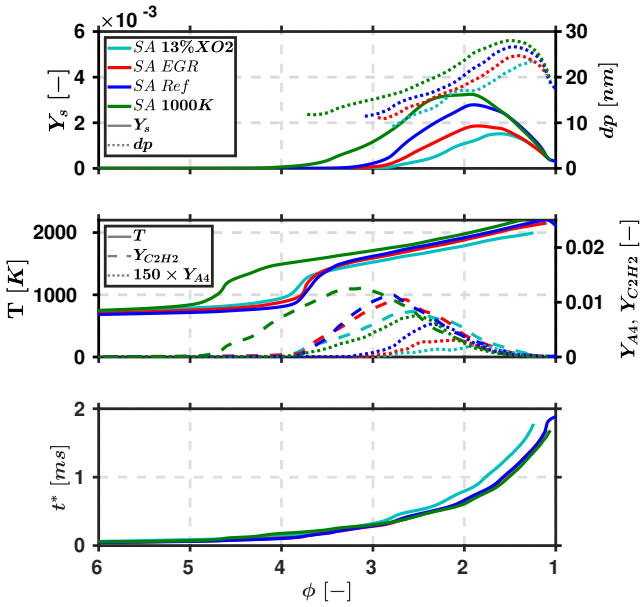

Figure 5.26: *Soot mass fraction, mean particle diameter, temperature, A4 mass fraction, C_2H_2 mass fraction and residence time at quasi-steady state along reference mixing trajectory for the spray reactivity parametric variations.*

fraction. Reduced concentrations of these two species, in particular the soot precursor *A*4, inhibit soot production in comparison to the "SA Ref" condition. The reduction in soot production in the low-oxygen concentration and reference condition with CO_2 and H_2O is seen to be caused by the reduction of the concentration of species relevant for soot nucleation and growth.

In relation to the increase in ambient temperature, the enhanced mixture reactivity ("SA 1000K" case compared to the "SA Ref" case) enables the ignition of richer mixtures (in agreement with a shorter LOL and the flame structure analysis presented in Chapter 4) that contribute to soot production. Differences in *A*4 and C_2H_2 mass fraction are also crucial since the high temperature condition shows the onset point at mixtures as rich as $\phi = 4$ for *A*4 and $\phi = 5$ for C_2H_2 while the reference condition show leaner onset mixtures (around $\phi = 3$ and $\phi = 4$ for the precursor and surface growth species, respectively) as well as lower peak values consistent with decreased soot production.

Lastly, the bottom panel in Figure 5.26 shows the integrated local residence time. With equal fuel injection conditions for all cases, the higher residence time for the "13%X_{O_2}" is the result of the different mixing field introduced

by the lower oxygen concentration. Despite this increase in residence time, the reduction of the concentration of $A4$ and C_2H_2 seems to play a more dominant role in the total amount of soot produced. As for the rest of conditions, and taking into account that there are virtually no changes in the residence time, it is then clear that the changes in soot production are the result of changes in the spray reactivity meaning that the onset equivalence ratio at which the high-temperature region appears and the concentration of soot precursor and surface growth species are the most relevant variables.

5.4. Effect of mixing process

Along this last section, the influence of variations of the spray mixing boundary conditions on soot production is studied. Similarly to the study of spray reactivity boundary condition variations, the nominal ECN Spray A is used as the reference condition to exemplify the influence that the injection pressure and nozzle diameter has on soot production. From the studied cases, the reference condition produces the less amount of soot followed by an intermediate case where the injection pressure is decreased to 100 MPa and finally the Spray D condition leading to the highest amount of soot. Experimental data for the first two conditions comes from experiments in the constant pressure vessel at CMT-Motores Térmicos [78]. For the Spray D condition, experiments were carried out in the constant volume vessel at SNL [28, 91]. Consequently, the Spray D case is an EGR case with CO_2 and H_2O in the ambient composition. Having discussed the implications of nonEGR and EGR ambient composition in the previous section, the study of the Spray D EGR condition in comparison to the Spray A nonEGR condition is still relevant in the context of spray mixing parametric variations. A summary of injection and thermodynamic boundary conditions is comprised in Table 5.2.

Table 5.2: *Fuel injection and thermodynamic conditions for the spray mixing parametric variations.*

	SA Ref	**SA 100MPa**	**SD 150MPa**
Nozzle diameter	89.4 μm	89.4 μm	190.3 μm
Injection pressure	150 MPa	100 MPa	150 MPa
Ambient composition			
X_{O_2}	0.15	0.15	0.15
X_{N_2}	0.85	0.85	0.7515
X_{CO_2}	0	0	0.0622
X_{H_2O}	0	0	0.0362

Nozzle No 210675 and 209135 for Spray A and Spray D, respectively.

The flame structure at quasi-steady state for the nominal Spray A and Spray D has been extensively discussed in Chapter 4. Nonetheless, and as a new Spray A condition is introduced, Figure 5.27 depicts key species and local heat release contours for the reference condition (top), the lower injection pressure Spray A (middle) and the nominal Spray D (bottom). Spatial coordinates have been normalized by the equivalent diameter which implies that for any case the same set of normalized spatial coordinates corresponds to the same equivalence ratio as illustrated in Section 4.2. The color-coded images on the left depicting species mass fraction normalized by the corresponding maximum concentration, show a similar flame structure among conditions with CH_2O (color blue) and OH (color red) at the low-temperature heat release and diffusion flame zones, respectively. In relation to soot, its precursor $A4$ (color green) is found at the spray core. Panels on the right show the local heat release rate field with a vertical line marking the LOL position from which the soot tendency can already be inferred. In this sense, the Spray A with 150 MPa injection pressure (the "SA Ref" condition is the least prone condition to produce soot) shows the longest normalized LOL meaning than the Spray A with 100 MPa (more prone to produce soot) and Spray D have the flame stabilized at richer mixtures. This observation is confirmed in Figure 5.28 where optical thickness CFD results for the lower pressure Spray A are compared to the experimental measurement. While maximum values for the reference Spray A (in Figure 5.5) were in the order of 2.5, its lower pressure case shows values in the order of 4.

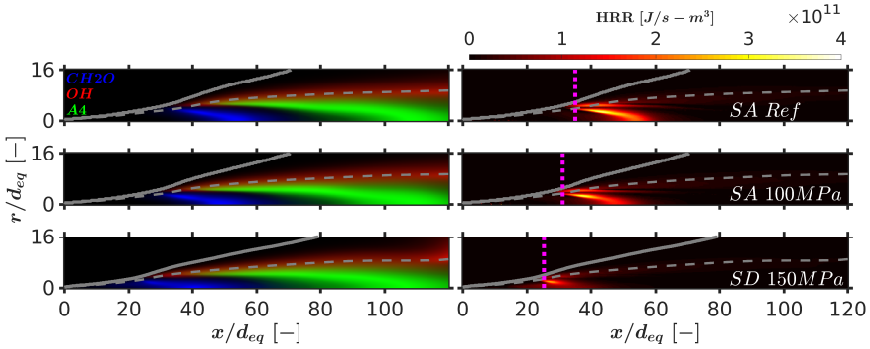

Figure 5.27: *Normalized species mass fraction and local HRR at quasi-steady state for the spray mixing parametric variations. Solid and dashed gray lines plotted at the spray radius and stoichiometric surface location, respectively. Vertical line marks lift-off length location.*

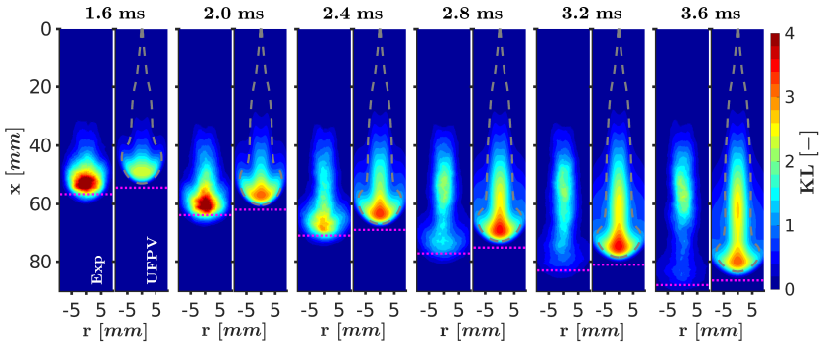

Figure 5.28: *Optical thickness for the 100 MPa case using the UFPV model. Dashed gray line marks the stoichiometric surface and dotted pink line marks the spray tip penetration.*

Regarding KL transient evolution, there are no much differences compared to those seen in Figure 5.5. CFD results are characterized by a faster transition between the initial mushroom-shaped soot structure into the ellipse-shaped structure. So, at 3.6 *ms* the experiment has reached quasi-steady state with the aforementioned ellipse-shaped structure and the CFD case is still transitioning into it. This slower transition is in line with the lag in the integrated soot mass ramp-up observed in Figure 5.29. The top panel shows results for the two Spray A cases (150 MPa and 100 MPa) and the bottom panel show results for the Spray D case. As previously discussed, The Spray A and Spray D experiments were conducted in different experimental facilities and differences in the FOV size have been accounted for in the CFD simulations.

The change in injection pressure (top panel) does not seem to change the soot onset time (consistent with minor differences in ID)[9] as both experimental and CFD results show similar ramp-ups. On the other hand, the injection pressure reduction does in fact change the result at quasi-steady state with an increased value for the lower injection pressure case. For these Spray A conditions, the deviation factor in soot mass at quasi-steady state (comparing CFD in relation to experimental results) remains barely unchanged with a factor of 2.6 for the 150 MPa condition and 2.3 for the 100 MPa condition.

[9]For the Spray D case there are two distinctive peaks in the maximum temperature time derivative data. The first peak is marked with a solid vertical line and the second peak with a dotted line.

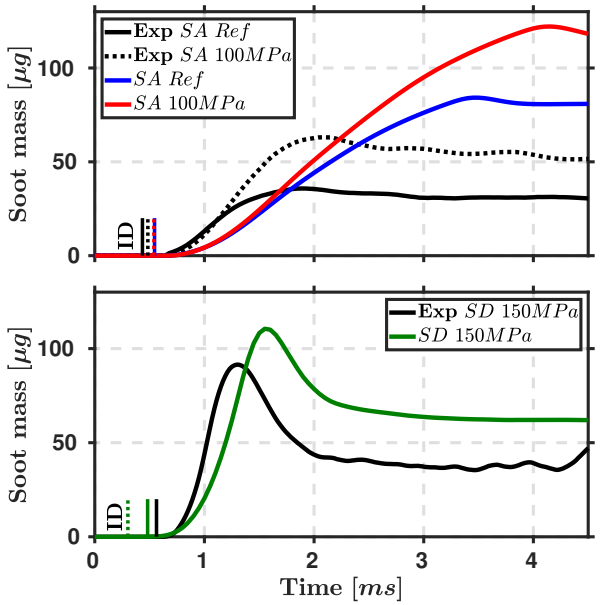

Figure 5.29: *Integrated soot mass for the spray mixing parametric variations using the UFPV model. Top panel includes results for Spray A nonEGR cases while the bottom panel shows results for the Spray D EGR case. Vertical line marks ignition delay time.*

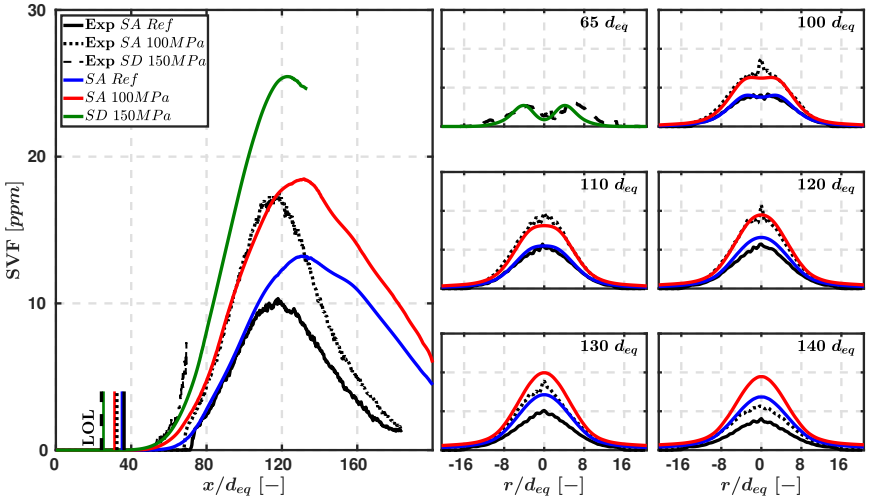

Figure 5.30: *Soot volume fraction axial and radial profiles for the spray mixing parametric variations using the UFPV model. Vertical line marks lift-off length location.*

The change in nozzle orifice diameter (bottom panel) induces a faster ramp-up, a feature captured by the CFD simulation, although it still over-predicts the integrated soot mass at quasi-steady state. As for the other experiment conducted in the combustion vessel at SNL (Spray A "SA EGR" condition in Section 5.3), the spike in the integrated soot mass curve is the result of the spray leaving the FOV. The temporal lag observed in the CFD results is consistent with the slightly lower spray tip penetration reported in Section 4.2 in Chapter 4. With lower tip penetration, compared to the experiment, the spray leaves the FOV later thus delaying the appearance of the soot mass spike. At quasi-steady state, the deviation factor from CFD results compared to experimental data is slightly lower compared to the Spray A condition with a value of 1.7.

Further validations for soot results at quasi-steady state are presented in Figure 5.30 for the SVF field. The 100 MPa Spray A and Spray D CFD results show a similar trend to what was previously observed for the reference Spray A. From the axial profiles, good agreement is seen for the ramp-up up until 120-130 d_{eq}.[10] The good agreement in the ramp-up region is not limited to the spray axis since the radial profiles are also in good agreement with the experimental results up until 120 d_{eq} for the reference Spray A condition and 130 d_{eq} for the lower pressure case. Even if the experimental data for the Spray D condition is limited to a smaller region compared to Spray A data, the radial profile at 65 d_{eq} shows that the good agreement is not just limited to the spray axis. Despite differences in the soot structure size, Figure 5.30 shows how the CFD simulations are able to capture the trend for the LOL location (vertical lines) and soot production with more soot predicted as the injection pressure drops from the Spray A 150 MPa to the 100 MPa and with the increase in nozzle diameter from the small Spray A to the larger Spray D.

Soot tendency can be further analyzed along the spray reference mixing trajectory (same criteria for reference mixing trajectory in Figure 5.26). Results for the soot mass fraction and mean particle diameter are presented in the top panel in Figure 5.31) while temperature, $A4$ mass fraction and C_2H_2 mass fraction results are plotted in the middle panel and lastly the integrated residence time is shown in the bottom panel. As might be already deduced from previous results, the increase in soot production comes with an increase in mean particle diameter (top panel) and a richer soot onset equivalence ratio for any mixing trajectory. Both observations are in line

[10] CFD results for the Spray D are limited to a smaller field of view in comparison to Spray A results.

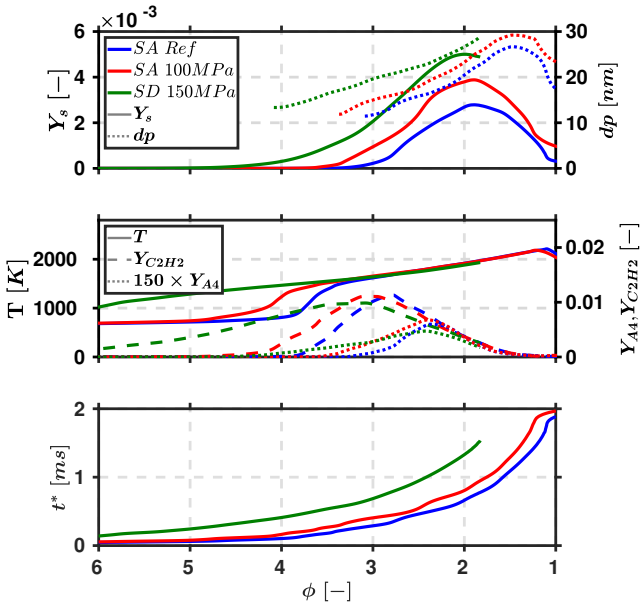

Figure 5.31: *Soot mass fraction, mean particle diameter, temperature, A4 mass fraction, C_2H_2 mass fraction and residence time at quasi-steady state along reference mixing trajectory for the spray mixing parametric variations.*

with temperature and species mass fraction results. For instance, higher temperature are reached at fuel-richer equivalence ratios as the mixing boundary conditions change from reference condition to the lower pressure and the higher nozzle orifice diameter, respectively. Higher residence time (bottom) allows for the ignition or richer mixtures as first discussed in Chapter 4. This richer combustion comes with the presence of $A4$ and C_2H_2 at richer equivalence ratios enhancing soot production. It is interesting to observe that even if the peak values of $A4$ and C_2H_2 for the Spray D are lower compared to the reference condition (lower values induced by the presence of CO_2 and H_2O in the initial ambient composition), the highest soot mass peak value corresponds to this condition. This observation is in line with richer combustion and longer residence time for the Spray D. In this regard, the increase in t^* is characterized by a factor of 2.1 and 1.2 for the increase in nozzle diameter and drop in injection pressure, respectively. Both factors agree with the analytical solution reported by García-Oliver [54] for mixing trajectories in a turbulent gas jet.

5.4.1. Split injection

To conclude the study of spray mixing boundary condition variations, the last case studied corresponds to an Spray A split injection case. To that end, two 500 μs long fuel injections are separated by a 500 μs dwell time with the same reference injection and thermodynamic conditions reported in Table 3.1.

A first remarkable feature in the split injection case is the reproducibility of the autoignition event of the first injection in comparison to the reference single injection case. Figure 5.32 depicts color-coded images for the normalized mass fraction[11] of CH_2O in blue and OH in red (panels on the left) and local HRR contours on the right. At the bottom of the figure, the first injection is seen to reproduce the results for the reference single injection case in terms of the integrated HRR up to 0.7 ms approximately. At that time, the top panels show a flame structure with minor differences in relation to the reference case in Fig. 4.16 with CH_2O in the vicinity of the low-temperature heat release zone and OH around the stoichiometric surface. The minor differences observed at 0.7 ms, zones releasing heat are slightly shifted toward the nozzle, are induced by the end of the first injection and the consequent recession of combustion [233]. Between 0.9-1.0 ms the HRR decreases and the stoichiometric surface is shifted downstream showing that combustion recession is accompanied by a fast transition from fuel-rich to lean mixtures consistent with entrainment waves caused by the end of the first injection [234]. It is worth mentioning that at 1 ms there is no CH_2O left from the first injection and that the CH_2O structure in the second injection is restrained to a smaller region as a result of CH_2O consumption enhanced by the high-temperature remains of the first injection. The latter observations are consistent with experimental observations [91]. Moreover, similarities in the autoignition event have also been reported experimentally with detailed descriptions for the reference single injection case [88] (discussed in Chapter 4) and the split injection case [235]. Just 0.1 ms after the start of the second injection, the spray interacts with the remains of the first injection thus accelerating autoignition as confirmed by the appearance of CH_2O (left panel at 1.1 ms). Beyond that time, there's an inflection in the integrated HRR curve as combustion from the second injection is established.

[11] Species mass fractions have been normalized by its maximum level at the last time in the figure.

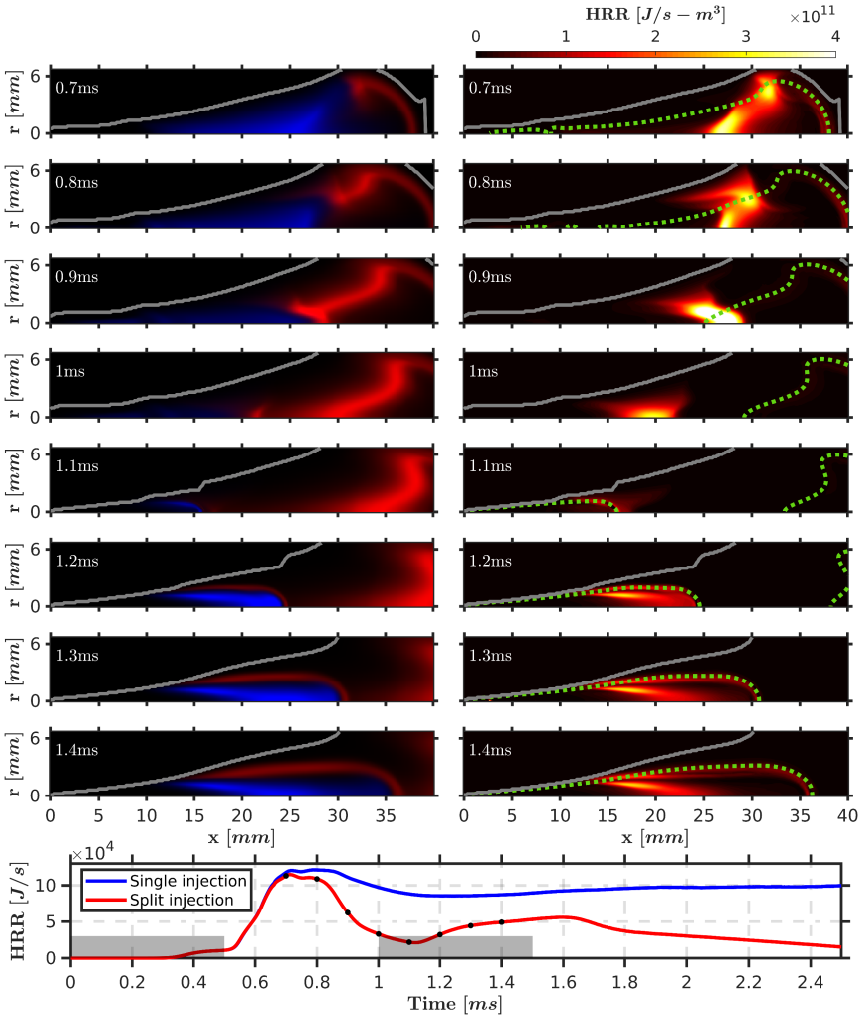

Figure 5.32: *Normalized species mass fraction, time- and spatially resolved local HRR for the Spray A split injection case. Dashed green contour at stoichiometric surface. Integrated HRR (bottom) plotted with markers indicating HRR contours timing. Gray shadow boxes mark the length of the two fuel injection events.*

To further analyze the combustion process in the split injection case, Figure 5.33 shows an extended sequence of the combustion process depicting variables of particular relevance for soot production. At each time instant, the left-hand side of the spray shows a color-coded image for the normalized

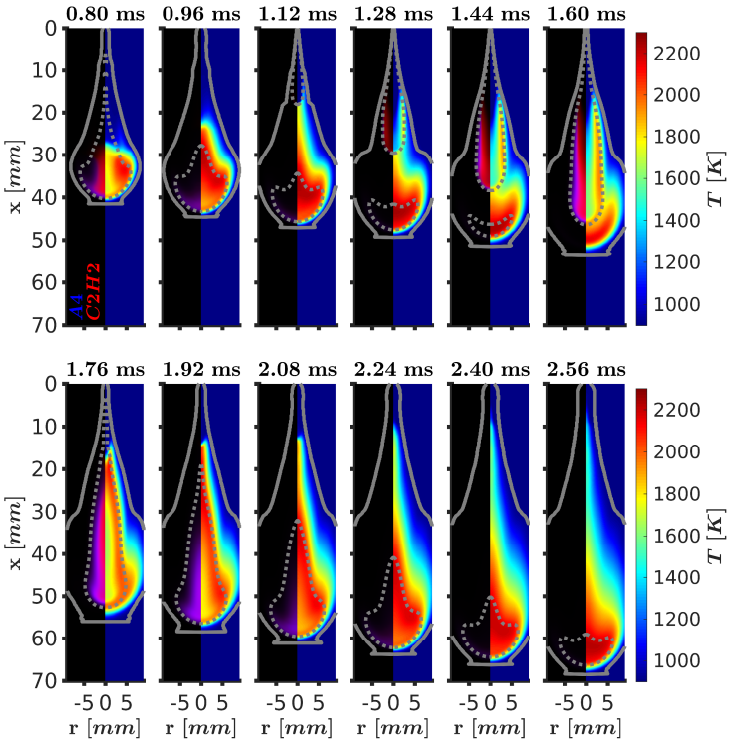

Figure 5.33: *Normalized species mass fraction and temperature contours for the Spray A split injection case. Dashed green contour at stoichiometric surface.*

mass fraction[12] of the soot precursor $A4$ (blue) and soot surface growth species C_2H_2 (red) while the right-hand side of the spray shows the temperature contour. At 0.8 *ms*, C_2H_2 can be observed downstream 30 *mm* close to the spray axis while the purple color results from the overlapping of C_2H_2 (red) and $A4$ (blue) at the spray head. The zone where these species are observed coincides with the fuel-rich core of the spray with lower temperatures compared to the peak values close to the stoichiometric surface. Concentration of $A4$ and C_2H_2 decreases as the spray dilutes and the temperature increase (0.96 *ms*) due to the entrainment waves effect. Between 1.12-1.60 *ms*, the second injection penetrates into the high-temperature remains from the first injection promoting the appearance of C_2H_2 (intense red region at 1.28 *ms*) and later $A4$ (1.44-1.60 *ms*). Similarly to previous observations

[12] Species mass fractions have been normalized by its maximum level between 0.8-2.56 *ms*.

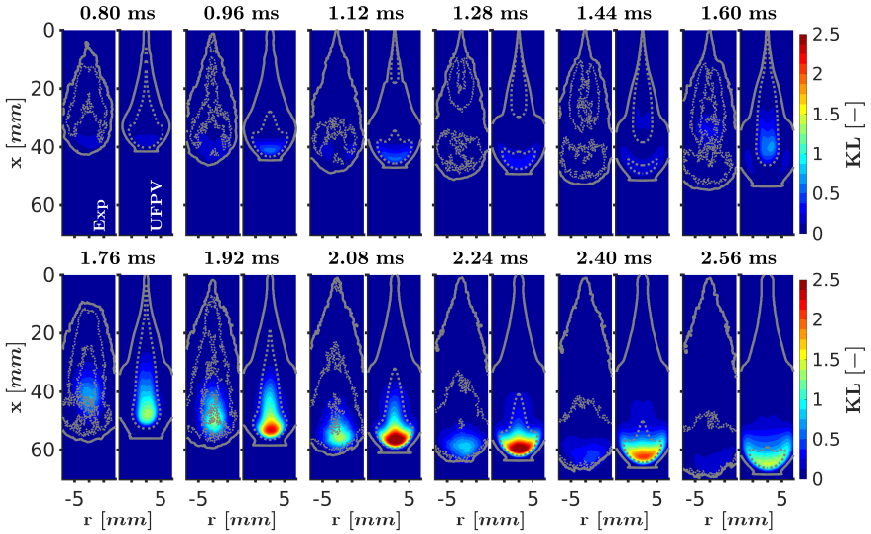

Figure 5.34: *Optical thickness for the split injection case using the UFPV model. The solid gray line marks the schlieren contour from the experiment and spray radius from the simulation while the dashed gray line marks the OH contour from the experiment and the stoichiometric surface from the simulation.*

for the first injection, the end of the second injection comes with a decrease in species concentration, dilution of the mixture across the whole spray and the increase in temperature toward the spray head (1.76-2.56 *ms*).

Having introduced the dynamics of the split injection case in terms of combustion, soot results are shown in Figure 5.34. Besides KL, experimental results for schlieren (solid gray line) and *OH* (dashed gray line) contours are also included [91, 236]. As for the CFD case, the spray radius and the stoichiometric surface are plotted with a solid and a dashed line, respectively. In qualitative terms, the comparison of schlieren and *OH* contours with the CFD predicted spray radius and stoichiometric surface indicate a good agreement for the spray dynamics. at all time instants depicted in Figure 5.34 the furthest distance reached by the spray matches reasonably well although the simulated spray is narrower.

As far as soot is concerned, it is seen from both experimental and numerical results how the first injection barely produces any soot. In fact, the soot onset time occurs after the end of the first injection close to 0.8 *ms*. At this time, similarly to the observation for the single injection case, soot appears at the spray head. This initial soot cloud seems to be fully oxidized in the experiment (no detectable soot around the spray head) while the CFD

results still show some soot remaining from the first injection up until 1.6 *ms*. Around this time, the second injection has reached the high-temperature gases from the first injection and soot is detected again between 30-40 *mm* in the experiment and 30-50 *mm* in the simulation. Later, caused by the end of the second injection, the experimental *OH* and numerical stoichiometric surface detach from the nozzle and continue moving downstream with the soot cloud. From 1.76 *ms* until 2.08 *ms* the KL signal in the experiment increases as soot is concentrated around the spray head. Earlier ignition resulting from the interaction with the remains from the first injection evidenced in Figure 5.32 and Figure 5.33 enhances soot production for the second injection through richer combustion. Beyond 2.08 *ms*, soot continues oxidizing until its barely detectable at 2.56 *ms*. Simulation results on the other hand, show a similar but slower behavior with decreasing high-concentration of soot in the spray head up until 2.56 *ms* where, unlike the experiment, soot can still be seen.

5.5. Summary

Along this chapter, soot modeling results have been presented. After a preliminary assessment of the soot model, a detailed analysis has been carried out for the Spray A reference condition for the one-way WM and the two-way UFPV approaches. The latter has then been the subject to study parametric variation of the spray reactivity and mixing boundary conditions. The most relevant findings lead to the following conclusions:

- The choice of constants for the different subprocesses that are accounted for by the soot model can substantially affect combustion if the gas phase and soot are two-way coupled. High consumption of C_2H_2 thorough surface growth has shown to induce a shift in temperature and key species (OH, CO, CO_2 and H_2O) toward rich mixtures. It has also been shown that soot can be fully oxidized within the fuel-rich core of the spray if the oxidization pre-exponential factor is high-enough. Consequently, soot constants need readjustment not only depending on the combustion model used but also on whether or not soot interacts with the gas phase.

- Soot transient evolution is well captured by the one-way WM and the two-way UFPV approaches but the transition from the initial mushroom-shaped soot structure into the ellipse-shaped structure reached at quasi-steady state is slower. Moreover, the WM model

shows better agreement for the integrated soot mass at quasi-steady state compared to the UFPV model, although the latter shows improved results for soot spatial distribution. It has been shown that even if the total soot mass matches the experimental value, the way in which it is distributed within the spray might be different.

- Soot surface growth is the driving process for soot formation while soot nucleation is key for the onset location at which soot starts forming in the spray. By adjusting the soot surface growth pre-exponential factor for the two-way coupling UFPV approach (Spray A reference condition), a good agreement for the SVF ramp-up region was found. Further downstream, SVF is over-predicted as the ellipse-shaped soot structure length is higher compared to the experimental data. With the default soot constants, the one-way WM approach also predicts a longer soot structure which is shifted downstream consistent with longer LOL.

- Over the two-way coupling UFPV approach variations in the oxidation rate and turbulent Schmidt number were performed to better understand the over-prediction in the soot structure length at quasi-steady state. By increasing the oxidation rate, the integrated soot mass can be targeted (at the cost of narrower SVF radial profiles), but no improvement in the extension of the soot structure is achieved. Similarly, no improvement is achieved by shifting the mixing field through the turbulent Schmidt number. Since validation under reacting conditions is not feasible at this time due to the lack of experimental data, the turbulent Schmidt number is a way to modify the mixing field without modifying the velocity field which, in contrast, is validated against experimental data. By decreasing the turbulent Schmidt number, the mixing field is shifted toward the nozzle but no improvement is achieved regarding the soot structure extension. In light of these findings, the need for a better description of turbulence and fuel-air mixing gains more relevance.

- The soot trend for the change in the spray reactivity boundary conditions is well reproduced. In comparison to the reference 900 K nonEGR Spray A, a 1000 K nonEGR case, a 900 K EGR case and a 13% ambient oxygen concentration case were analyzed. The two-way coupling UFPV approach shows that, with similar integrated residence time, the onset equivalence ratio for high-temperature and species concentration are crucial for soot production. The addition of CO_2

and H_2O to the ambient composition barely changes the LOL location or temperature profile along the reference mixing trajectory while decreasing the concentration of $A4$ and C_2H_2 thus inhibiting soot production in comparison to the nonEGR case. The higher temperature case on the other hand, exhibits shorter LOL hence richer combustion favoring the production of soot.

- CFD results also show a good agreement in terms of soot trend for the change in the spray mixing boundary conditions. In contrast to results for the spray reactivity boundary condition variations, the integrated residence time is proven to be determinant. The 100 MPa Spray A and the nominal Spray D with longer residence time produce more soot compared to the reference Spray A. The increase in residence time along the reference mixing trajectory enhances soot production through richer combustion. It is interesting to note that even if $A4$ and C_2H_2 peak values along the reference mixing trajectory for the Spray A cases were higher compared to the Spray D case, the latter produces more soot favored by longer residence times.

- The two-way coupling UFPV approach proved suitable for the study of a split injection Spray A case. The combustion process agrees well with the experimental description from the literature. In this regard, the autoignition sequence of the first injection shows remarkable similarities with the single injection reference case with the exception of the pre-mixed HRR peak which is affected by the end-of-injection characteristic phenomena. The recession of combustion promotes the complete consumption of CH_2O from the first injection while restraining the extension of this species coming from the second injection. As for soot, the first injection barely produces it but the high-temperature remains accelerate the autoignition of the second injection thus favoring richer combustion and soot production. The model is seen to be able to qualitatively reproduced the soot production transient evolution for the optical thickness, spray and OH contours.

CHAPTER 6

Conclusions and future works

This last chapter offers a summary of the research work reported throughout the thesis. The summary is accompanied by the conclusions from the several tasks carried out to fulfill the thesis main objective. At the end of the chapter, some future works are discussed to outline possible new research studies that could potentially contribute to the improvement of the understanding of soot production with the ultimate goal of reducing it within the context of the internal combustion engine.

6.1. Conclusions

Back in Chapter 1, the thesis main objective was set *to simulate soot production in Diesel sprays under engine-like conditions using CFD*. The fulfillment of this objective was framed in the context of CI engines for which the single-hole nozzle spray was chosen as the main subject of study. More concretely, target sprays for the Engine Combustion Network were chosen since a vast experimental database is available for the validation of combustion and soot modeling results. Computationally, the thesis was conducted within a RANS framework for the treatment of turbulence, a well-mixed and a flamelet based combustion modeling approaches and a two-equation soot model for the study of soot production.

From the literature review on combustion and soot production in Diesel-like sprays reported in Chapter 2, soot modeling was proved to be a challenging endeavor. With soot production at the end of a long chain of highly non-linear, multi-phase and multi-scale phenomena, the thesis soot modeling approach was focused on the use of a two-equation model on the basis of

a good compromise between accuracy and computational cost in order to assess the whole chain of events from the inert spray to soot production and the effects of mixture reactivity and mixing boundary condition variations.

The thesis main objective was fulfilled through the completion of three main tasks comprising the key processes in the chain of events leading to soot production. These tasks and the most relevant findings derived from their completion are summarized below.

- **Validation of the computational setup under inert conditions.**

  In Chapter 3, the full modeling approach including the spray description through a RANS Lagrangian parcel, Eulerian fluid approach was outlined. The computational setup was validated against experimental data from the ECN Spray A and Spray D in Chapter 4. Spray global and local quantities namely, spray tip penetration, liquid length, local mixture fraction, mixture fraction variance and axial velocity allowed for the validation of results relevant to the spray dynamics and mixing field. In this way the computational setup used, proved suitable for the proper simulation of the first stages in the chain of events (described in Chapter 2) leading to the combustion of a Diesel-like spray namely, liquid spray atomization, evaporation and fuel-air mixing.

- **Assessment of sub-grid flame structure and TCI influence on combustion.**

  Results for the assessment of the WM and flamelet concepts for the sub-grid flame assumption and TCI were reported in Chapter 4. The ECN spray A and Spray D under the same operating condition were used as modeling targets to allow for the assessment of the nozzle orifice diameter on spray combustion. The most relevant contributions and findings are:

  - The introduction of the mixing trajectory concept to quantify local residence time and to bridge a link between spray spatial coordinates and the more combustion-relevant $\phi - T$ coordinates.
  - The zone where autoignition occurs has been shown to be related to zones with high local residence time. In this regard, both the WM and the UFPV models predict autoignition around the spray radial periphery where a "gas particle" meets a sufficiently diluted state of mixing faster compared to a "gas particle" close to the spray axis.

- The WM and UFPV models predict a similar autoignition sequence. The main difference resides on the spatial width of the main ignition zone. Results from the WM model show a narrow ignition zone around the most reactive mixture fraction for a closed homogeneous reactor in contrast to the broader range of mixtures observed in UFPV results.
- The flame structure at quasi-steady state from WM and UFPV results show deeper differences compared to the autoignition sequence. The scalar dissipation rate accounted for by the UFPV model plays a key role. The high scalar dissipation rate in the near-nozzle region seems to shift the low-temperature heat release zone further downstream. As for LOL, the scalar dissipation rate seems to contribute to its stabilization closer to the nozzle in comparison to WM results.
- The smaller nozzle diameter in Spray A promotes faster mixing characterized by shorter residence time per unit of ϕ leading to an earlier ignitable mixing state in relation to the larger Spray D nozzle. As for the ignition location, higher scalar dissipation rate and a slower spray development in the Spray A causes this event to take place closer to the spray head while lower scalar dissipation rate and faster spray tip development in the Spray D allows ignition to take place closer to the spray radial periphery and further upstream from the spray head.

- **Study of reactivity and mixing boundary condition variations effect on combustion and soot production.**

  Soot production results were comprised in Chapter 5. The two-equation Gokul model in conjunction with the WM and UFPV modes was used to study soot production. A preliminary assessment of the soot model with default constants was carried out for the reference Spray A, followed by the analysis of spray reactivity and mixing boundary condition variation results. The most relevant contributions and findings are:

  - With a two-way coupling between soot and the gas-phase, the choice of soot subprocess constants can significantly affect the latter. It was shown that default constants for the Gokul soot model induced a shift in temperature, OH and combustion major species (CO, CO_2 and H_2O) toward rich mixtures at flamelet level

that was later reproduced in the CFD results. C_2H_2 consumption through surface growth was identified as the major contributor to the aforementioned shift.

- WM and UFPV results for the reference Spray A show that both modeling approaches are able to capture the soot transient evolution characterized by an initial mushroom-shaped soot structure that transitions into an ellipse-shaped structure at quasi-steady state. This transient evolution has been shown to be slower in the CFD cases and to be accompanied by a longer quasi-steady soot structure compared to the experimental data.
- Changes in the soot oxidation rate and the turbulent Schmidt number show limited to no room for the improvement of the quantitative agreement for the soot structure size at quasi-steady state. Results suggest that for better agreement a more detailed description of the mixing and turbulence interaction might be needed.
- The residence time integrated over a mixing trajectory does not significantly change with different ambient compositions (nonEGR and EGR cases) or with the increase in ambient temperature. Under variations of spray reactivity boundary conditions, the onset equivalence ratio for high-temperature and the appearance of the soot precursor $A4$ and species concentration are the key elements controlling soot production. This observation also holds true for the low-oxygen concentration case which exhibited a slightly higher residence time.
- In comparison to the reference Spray A condition with N_2 and O_2 ambient composition (nonEGR case), the presence of CO_2 and H_2O (EGR case) promotes a reduction in soot production primarily due to a decreased concentration of $A4$ and C_2H_2. The decrease in soot production with the addition of CO_2 and H_2O is in line with experimental observations reported within the ECN community.
- For variations of the spray mixing boundary conditions the residence time integrated over a mixing trajectory gains relevance not only for combustion but also for the soot production process. A decrease in the injection pressure or the increase in nozzle diameter promotes longer residence time along mixing trajectories thus enhancing soot production trough richer combustion.

- The modeling approach assessed in this work has been proven to be suitable for the qualitative description of the soot production process in a split fuel injection case. Results capture the dynamics between the two injection events. Even if the first injection barely produces any soot, its high-temperature remains enhances the production of soot in the second injection favoring a faster autoignition process, compared to the first injection, and richer combustion.

In light of these findings it is clear that soot production in a Diesel-like spray cannot be studied as an isolated process. On the contrary, a comprehensive view covering as many links as possible in the chain of events leading to combustion and soot production is required. Soot tendencies cannot be fully understood without analyzing combustion which cannot be fully studied without the study of spray mixing phenomena that in many cases are better understood under inert conditions. The mixing trajectory concept proved to be a powerful tool to analyze the combustion and soot production processes in Diesel-like sprays. Through this concept, it was clearly shown that the effect of the mixture reactivity on soot production was driven by the onset equivalence ratio at which combustion is established i.e. how fuel-rich the combustion is. As for the effect of the mixing process, conceptualizing the spray as a set of mixers defined by mixing trajectories allowed to assess the importance of not only the onset equivalence ratio but also of the equally relevant residence time.

6.2. Future works

Without a doubt there's still room, and more importantly the need, for improvement in soot modeling as it is a valuable tool to gain knowledge on soot production and how to mitigate it in the context of the ICE. To continue closing the knowledge gap, the following proposals might be relevant to that end:

- The assessment of additional chemical mechanisms, including PAH chemistry, might be advantageous. Under the operating conditions studied in Chapter 5, the Narayanaswamy mechanism showed a general over-prediction tendency for the ignition delay time, so a different chemical mechanism yielding improved ID results might contribute to a better qualitative description of soot production.

- Although there's no currently experimental data to validate the mixing field under reacting conditions, soot results suggest that a RANS approach might not be sufficiently accurate in describing the mixing and turbulence interaction. The extension of this work using LES might also help in shedding light on current quantitative discrepancies with experimental data. Such an extension should comprise a full evaluation of the LES approach from the inert and reacting spray to soot production.

- The ultimate goal behind the study of soot production in Diesel-like sprays is the assessment of this process in the combustion chamber of an ICE. Thus, the study of soot production in that scenario is unquestionably of high relevance. It'd be interesting to study the performance of the soot modeling approach used in this thesis under a variable pressure, non-quiescent environment. Additionally, the analysis of spray-spray interactions and wall impingement on combustion and soot production gains relevance. Lastly, in the context of ICEs the study of NO_x emissions, especially for CI engines, would be of much interest.

- The relevance of soot production extends beyond Diesel-like sprays. On one hand, the study of the production of soot from other fuel sources such as low-carbon fuels is needed to assess the feasibility of these to contribute to cleaner operation of ICEs. On the other hand, apart from the applicability to ICEs the soot modeling approach used throughout this work can potentially be extended for the study of soot production in gas turbines as the emission of this pollutant is also detrimental in this type of devices.

- Detailed soot models, although more computationally expensive, offer the ability to analyze the soot particle size distribution function. With stricter particle matter legislation, the implementation of a detailed soot model in the UFPV model framework might also be an exiting and beneficial challenge to further study soot production.

Bibliography

[1] I. E. Agency. *World Energy Outlook 2019*. https://www.iea.org/weo2019/. 2019 (cited in pp. 1, 2).

[2] *International Energy Outlook 2019*. https://www.eia.gov/outlooks/ieo/ (cited in p. 1).

[3] P. Senecal and F. Leach. "Diversity in Transportation: Why a Mix of Propulsion Technologies Is the Way Forward for the Future Fleet". *Results in Engineering* 4, 2019, p. 100060 (cited in p. 1).

[4] J. R. Serrano, R. Novella, and P. Piqueras. "Why the Development of Internal Combustion Engines Is Still Necessary to Fight against Global Climate Change from the Perspective of Transportation". *Applied Sciences* 9 (21), 2019, p. 4597 (cited in p. 1).

[5] M. M. Thackeray, C. Wolverton, and E. D. Isaacs. "Electrical Energy Storage for Transportation—Approaching the Limits of, and Going beyond, Lithium-Ion Batteries". *Energy & Environmental Science* 5 (7), 2012, p. 7854 (cited in p. 1).

[6] X. Shen, H. Liu, X.-B. Cheng, C. Yan, and J.-Q. Huang. "Beyond Lithium Ion Batteries: Higher Energy Density Battery Systems Based on Lithium Metal Anodes". *Energy Storage Materials* 12, 2018, pp. 161–175 (cited in p. 2).

[7] K. Turcheniuk, D. Bondarev, V. Singhal, and G. Yushin. "Ten Years Left to Redesign Lithium-Ion Batteries". *Nature* 559 (7715), 2018, pp. 467–470 (cited in p. 2).

[8] M. O. Andreae, C. D. Jones, and P. M. Cox. "Strong Present-Day Aerosol Cooling Implies a Hot Future". *Nature* 435 (7046), 2005, pp. 1187–1190 (cited in p. 2).

[9] M. Andreae and D. Rosenfeld. "Aerosol–Cloud–Precipitation Interactions. Part 1. The Nature and Sources of Cloud-Active Aerosols". *Earth-Science Reviews* 89 (1-2), 2008, pp. 13–41 (cited in p. 2).

[10] M. Z. Jacobson. "Short-Term Effects of Controlling Fossil-Fuel Soot, Biofuel Soot and Gases, and Methane on Climate, Arctic Ice, and Air Pollution Health". *Journal of Geophysical Research* 115 (D14), 2010 (cited in pp. 2, 7).

[11] J. Hansen and L. Nazarenko. "Soot Climate Forcing via Snow and Ice Albedos". *Proceedings of the National Academy of Sciences* 101 (2), 2004, pp. 423–428 (cited in p. 2).

[12] O. L. Hadley and T. W. Kirchstetter. "Black-Carbon Reduction of Snow Albedo". *Nature Climate Change* 2 (6), 2012, pp. 437–440 (cited in p. 2).

[13] I. M. Kennedy. "The Health Effects of Combustion-Generated Aerosols". *Proceedings of the Combustion Institute* 31 (2), 2007, pp. 2757–2770 (cited in pp. 2, 7).

[14] K. S. Hougaard, K. A. Jensen, P. Nordly, C. Taxvig, et al. "Effects of Prenatal Exposure to Diesel Exhaust Particles on Postnatal Development, Behavior, Genotoxicity and Inflammation in Mice". *Particle and Fibre Toxicology* 5 (1), 2008, p. 3 (cited in pp. 2, 7).

[15] I. N. Krivoshto, J. R. Richards, T. E. Albertson, and R. W. Derlet. "The Toxicity of Diesel Exhaust: Implications for Primary Care". *The Journal of the American Board of Family Medicine* 21 (1), 2008, pp. 55–62 (cited in pp. 2, 7).

[16] M. Shiraiwa, K. Selzle, and U. Pöschl. "Hazardous Components and Health Effects of Atmospheric Aerosol Particles: Reactive Oxygen Species, Soot, Polycyclic Aromatic Compounds and Allergenic Proteins". *Free Radical Research* 46 (8), 2012, pp. 927–939 (cited in pp. 2, 7).

[17] *Regulation (EC) No 764/2008 of the European Parliament and of the Council*. 2015 (cited in pp. 2, 7).

[18] K. C. Vora, K. E. Gurnule, and S. Venkatesh. "Diesel Particulate Filter". In: *Design and Development of Heavy Duty Diesel Engines: A Handbook*. Ed. by P. A. Lakshminarayanan and A. K. Agarwal. Singapore: Springer Singapore, 2020, pp. 313–339 (cited in p. 2).

[19] C. K. Lambert. "Current State of the Art and Future Needs for Automotive Exhaust Catalysis". *Nature Catalysis* 2 (7), 2019, pp. 554–557 (cited in p. 3).

[20] A. K. Agarwal, A. P. Singh, and R. K. Maurya. "Evolution, Challenges and Path Forward for Low Temperature Combustion Engines". *Progress in Energy and Combustion Science* 61, 2017, pp. 1–56 (cited in p. 3).

[21] X. Li, H. Zhou, L. M. Zhao, L. Su, H. Xu, and F. Liu. "Effect of Split Injections Coupled with Swirl on Combustion Performance in DI Diesel Engines". *Energy Conversion and Management* 129, 2016, pp. 180–188 (cited in p. 3).

[22] A. Yousefi, H. Guo, and M. Birouk. "An Experimental and Numerical Study on Diesel Injection Split of a Natural Gas/Diesel Dual-Fuel Engine at a Low Engine Load". *Fuel* 212, 2018, pp. 332–346 (cited in p. 3).

[23] T. Mendiara, F. García-Labiano, A. Abad, P. Gayán, et al. "Negative CO2 Emissions through the Use of Biofuels in Chemical Looping Technology: A Review". *Applied Energy* 232, 2018, pp. 657–684 (cited in p. 3).

[24] T. Larsson, O. Stenlaas, and A. Erlandsson. "Future Fuels for DISI Engines: A Review on Oxygenated, Liquid Biofuels". In: *International Powertrains, Fuels & Lubricants Meeting*. 2019 (cited in p. 3).

[25] S. Verhelst, J. W. Turner, L. Sileghem, and J. Vancoillie. "Methanol as a Fuel for Internal Combustion Engines". *Progress in Energy and Combustion Science* 70, 2019, pp. 43–88 (cited in p. 3).

[26] R. S. G. Baert, P. J. M. Frijters, B. Somers, C. C. M. Luijten, and W. de Boer. "Design and Operation of a High Pressure, High Temperature Cell for HD Diesel Spray Diagnostics: Guidelines and Results". In: *SAE World Congress & Exhibition*. 2009 (cited in p. 3).

[27] L. M. Pickett, C. L. Genzale, G. Bruneaux, L.-M. Malbec, et al. "Comparison of Diesel Spray Combustion in Different High-Temperature, High-Pressure Facilities". *SAE International Journal of Engines* 3 (2), 2010, pp. 156–181 (cited in p. 3).

[28] *Engine Combustion Network*. https://ecn.sandia.gov/ (cited in pp. 3, 37, 56, 91, 109, 112, 117).

[29] J. Warnatz, U. Maas, and R. W. Dibble. *Combustion*. Vol. 4. Berlin: Springer, 2006 (cited in pp. 7, 18–20, 23).

[30] N. Peters. *Turbulent Combustion*. Cambridge Monographs on Mechanics. Cambridge: Cambridge University Press, 2000 (cited in pp. 7, 13, 41).

[31] Y. Sun, Z. Guan, and K. Hooman. "Cavitation in Diesel Fuel Injector Nozzles and Its Influence on Atomization and Spray". *Chemical Engineering & Technology* 42 (1), 2019, pp. 6–29 (cited in p. 8).

[32] R. Payri, J. P. Viera, V. Gopalakrishnan, and P. G. Szymkowicz. "The Effect of Nozzle Geometry over Internal Flow and Spray Formation for Three Different Fuels". *Fuel* 183, 2016, pp. 20–33 (cited in pp. 8, 11).

[33] A. Tekawade, P. Mitra, B. A. Sforzo, K. E. Matusik, et al. "A Comparison between CFD and 3D X-Ray Diagnostics of Internal Flow in a Cavitating Diesel Injector Nozzle", p. 9 (cited in p. 8).

[34] F. Salvador, J. De la Morena, J. Martínez-López, and D. Jaramillo. "Assessment of Compressibility Effects on Internal Nozzle Flow in Diesel Injectors at Very High Injection Pressures". *Energy Conversion and Management* 132, 2017, pp. 221–230 (cited in p. 8).

[35] R. Reitz and F. Bracco. "Mechanisms of Breakup of Round Liquid Jets, The Encyclopedia of Fluid Mechanics". *Ed. N. Cheremisnoff* 3, 1986, pp. 233–49 (cited in p. 9).

[36] F. Payri, J. Desantes, and J. Arrègle. "Characterization of DI Diesel Sprays in High Density Conditions". *SAE transactions*, 1996, pp. 1085–1094 (cited in p. 9).

[37] R. Payri, G. Bracho, P. Marti-Aldaravi, and A. Viera. "NEAR FIELD VISUALIZATION OF DIESEL SPRAY FOR DIFFERENT NOZZLE INCLINATION ANGLES IN NON-VAPORIZING CONDITIONS". *Atomization and Sprays* 27 (3), 2017, pp. 251–267 (cited in p. 9).

[38] C. Baumgarten. *Mixture Formation in Internal Combustion Engines*. en. Heat and Mass Transfer. Berlin ; New York: Springer, 2006 (cited in pp. 9, 10).

[39] G. M. Magnotti and C. L. Genzale. "Recent Progress in Primary Atomization Model Development for Diesel Engine Simulations". In: *Two-Phase Flow for Automotive and Power Generation Sectors*. Ed. by K. Saha, A. Kumar Agarwal, K. Ghosh, and S. Som. Singapore: Springer Singapore, 2019, pp. 63–107 (cited in p. 9).

[40] R. D. Reitz. "Atomization and Other Breakup Regimes of a Liquid Jet". PhD thesis. Princeton: Princeton University, 1978 (cited in p. 9).

[41] R. D. Reitz. "Mechanism of Atomization of a Liquid Jet". *Physics of Fluids* 25 (10), 1982, p. 1730 (cited in p. 9).

[42] P.-K. Wu and G. M. Faeth. "Aerodynamic Effects on Primary Breakup of Turbulent Liquids". *Atomization and Sprays* 3 (3), 1993, pp. 265–289 (cited in p. 9).

[43] C. Crua, M. R. Heikal, and M. R. Gold. "Microscopic Imaging of the Initial Stage of Diesel Spray Formation". *Fuel* 157, 2015, pp. 140–150 (cited in p. 9).

[44] A. Kastengren and C. F. Powell. "Synchrotron X-Ray Techniques for Fluid Dynamics". *Experiments in Fluids* 55 (3), 2014 (cited in p. 10).

[45] A. Kastengren, C. F. Powell, D. Arms, E. M. Dufresne, H. Gibson, and J. Wang. "The 7BM Beamline at the APS: A Facility for Time-Resolved Fluid Dynamics Measurements". *Journal of Synchrotron Radiation* 19 (4), 2012, pp. 654–657 (cited in p. 10).

[46] C. F. Powell, D. Duke, A. L. Kastengren, and J. Ilavsky. "Measurements of Diesel Spray Droplet Size with Ultra-Small Angle X-Ray Scattering". In: *ILASS Americas, 25th Annual Conference on Liquid Atomization and Spray Systems*. Pittsburgh, 2013, p. 7 (cited in p. 10).

[47] A. Kastengren, J. Ilavsky, J. P. Viera, R. Payri, et al. "Measurements of Droplet Size in Shear-Driven Atomization Using Ultra-Small Angle x-Ray Scattering". *International Journal of Multiphase Flow* 92, 2017, pp. 131–139 (cited in p. 10).

[48] A. Pandal Blanco. "Implementation and Development of an Eulerian Spray Model for CFD Simulations of Diesel Sprays". PhD thesis. Valencia: Universitat Politècnica de València, 2016 (cited in pp. 10, 39).

[49] G. Magnotti and C. Genzale. "Detailed Assessment of Diesel Spray Atomization Models Using Visible and X-Ray Extinction Measurements". *International Journal of Multiphase Flow* 97, 2017, pp. 33–45 (cited in p. 10).

[50] G. M. Magnotti. "Modeling the Influence of Nozzle-Generated Turbulence on Diesel Sprays". PhD thesis. Atlanta: Georgia Institute of Technology, 2017 (cited in p. 10).

[51] S. Kim, G. Magnotti, G. Martinez, B. Yraguen, et al. "Validation of a New Turbulence-Induced Lagrangian Primary Breakup Model for Diesel Spray Atomization". In: *14th International Conference on Liquid Atomization and Spray Systems (ICLASS)(Chicago, IL)*. 2018 (cited in p. 10).

[52] A. Wierzba. "Deformation and Breakup of Liquid Drops in a Gas Stream at Nearly Critical Weber Numbers". *Experiments in Fluids* 9 (1-2), 1990, pp. 59–64 (cited in p. 10).

[53] C. Micó Reche. "Development of Measurement and Visualization Techniques for Characterization of Mixing and Combustion Processes with Surrogate Fuels". PhD thesis. Valencia: Universitat Politècnica de València, 2015 (cited in p. 11).

[54] J. M. García Oliver. "Aportaciones al Estudio Del Proceso de Combustión Turbulenta de Chorros En Motores Diesel Del Inyección Directa". PhD thesis. Valencia: Universitat Politècnica de València, 2004 (cited in pp. 11, 12, 63, 122).

[55] D. L. Siebers. "Liquid-Phase Fuel Penetration in Diesel Sprays". In: *International Congress & Exposition*. 1998 (cited in p. 11).

[56] D. L. Siebers. "Scaling Liquid-Phase Fuel Penetration in Diesel Sprays Based on Mixing-Limited Vaporization". In: *International Congress & Exposition*. 1999 (cited in p. 11).

[57] J. Gimeno. "Desarrollo y Aplicación de La Medida Del Flujo de Cantidad de Movimiento de Un Chorro Diesel". PhD thesis. Valencia: Universitat Politècnica de València, 2008 (cited in p. 11).

[58] J. B. Heywood. *Internal Combustion Engine Fundamentals*. McGraw-Hill, Inc, 1988 (cited in pp. 11, 16, 18).

[59] B. S. Higgins, C. J. Mueller, and D. L. Siebers. "Measurements of Fuel Effects on Liquid-Phase Penetration in DI Sprays". In: *SAE Technical Paper*. 1999 (cited in p. 11).

[60] J. V. Pastor, J. M. Garcia-Oliver, V. Bermudez, and C. Micó. "Spray Characterization for Pure Fuel and Binary Blends under Non-Reacting Conditions". In: *SAE Technical Paper*. 2014 (cited in p. 11).

[61] C. Espey and J. E. Dec. "The Effect of TDC Temperature and Density on the Liquid-Phase Fuel Penetration in a D. I. Diesel Engine". In: *SAE Technical Paper*. 1995 (cited in p. 11).

[62] R. Payri, J. Gimeno, M. Bardi, and A. H. Plazas. "Study Liquid Length Penetration Results Obtained with a Direct Acting Piezo Electric Injector". *Applied Energy* 106, 2013, pp. 152–162 (cited in p. 11).

[63] R. Payri, J. Gimeno, G. Bracho, and D. Vaquerizo. "Study of Liquid and Vapor Phase Behavior on Diesel Sprays for Heavy Duty Engine Nozzles". *Applied Thermal Engineering* 107, 2016, pp. 365–378 (cited in p. 11).

[64] S. M. Martínez. "Desarrollo de Una Instalación Experimental Para El Estudio de Chorros Diesel Evaporados En Atmósfera Inerte y Reactiva". PhD thesis. Universidad Politécnica de Valencia, 2003 (cited in p. 11).

[65] V. S. Alberto. "Effect of Multiple Injection Strategies on the Diesel Spray Formation and Combustion Using Optical Diagnostics". PhD thesis. Valencia: Universitat Politècnica de València, 2019 (cited in p. 12).

[66] L. M. Pickett, J. Manin, C. L. Genzale, D. L. Siebers, M. P. B. Musculus, and C. A. Idicheria. "Relationship Between Diesel Fuel Spray Vapor Penetration/Dispersion and Local Fuel Mixture Fraction". *SAE International Journal of Engines* 4 (1), 2011, pp. 764–799 (cited in pp. 12, 37).

[67] V. Macian, R. Payri, A. Garcia, and M. Bardi. "Experimental Evaluation of the Best Approach for Diesel Spray Images Segmentation". *Experimental Techniques* 36 (6), 2012, pp. 26–34 (cited in p. 12).

[68] T. D. Fansler and S. E. Parrish. "Spray Measurement Technology: A Review". *Measurement Science and Technology* 26 (1), 2015, p. 012002 (cited in p. 12).

[69] G. Bruneaux. "Liquid and Vapor Spray Structure in High-Pressure Common Rail Diesel Injection". *Atomization and Sprays* 11 (5), 2001 (cited in p. 12).

[70] J. V. Pastor, R. Payri, J. M. Garcia-Oliver, and F. J. Briceño. "ANALYSIS OF TRANSIENT LIQUID AND VAPOR PHASE PENETRATION FOR DIESEL SPRAYS UNDER VARIABLE INJECTION CONDITIONS". *Atomization and Sprays* 21 (6), 2011, pp. 503–520 (cited in p. 12).

[71] J. V. Pastor, R. Payri, J. M. Garcia-Oliver, and J.-G. Nerva. "Schlieren Measurements of the ECN-Spray A Penetration under Inert and Reacting Conditions". In: *SAE 2012 World Congress & Exhibition*. 2012 (cited in pp. 12, 37).

[72] F. Payri, R. Payri, M. Bardi, and M. Carreres. "Engine Combustion Network: Influence of the Gas Properties on the Spray Penetration and Spreading Angle". *Experimental Thermal and Fluid Science* 53, 2014, pp. 236–243 (cited in p. 12).

[73] H. Hiroyasu and M. Arai. "Structures of Fuel Sprays in Diesel Engines". In: *SAE Technical Paper*. Detroit, 1990 (cited in p. 12).

[74] F. Payri, V. Bermúdez, R. Payri, and F. Salvador. "The Influence of Cavitation on the Internal Flow and the Spray Characteristics in Diesel Injection Nozzles". *Fuel* 83 (4-5), 2004, pp. 419–431 (cited in p. 12).

[75] J. Desantes, R. Payri, F. Salvador, and A. Gil. "Development and Validation of a Theoretical Model for Diesel Spray Penetration". *Fuel* 85 (7-8), 2006, pp. 910–917 (cited in p. 12).

[76] J. Pastor, J. Javierlopez, J. Garcia, and J. Pastor. "A 1D Model for the Description of Mixing-Controlled Inert Diesel Sprays". *Fuel* 87 (13-14), 2008, pp. 2871–2885 (cited in p. 12).

[77] S. Kook and L. M. Pickett. "Liquid Length and Vapor Penetration of Conventional, Fischer–Tropsch, Coal-Derived, and Surrogate Fuel Sprays at High-Temperature and High-Pressure Ambient Conditions". *Fuel* 93, 2012, pp. 539–548 (cited in p. 12).

[78] T. Xuan. "Optical Investigations on Diesel Spray Dynamics and In-Flame Soot Formation". PhD thesis. Valencia: Universitat Politècnica de València, 2017 (cited in pp. 12–14, 96, 109, 112, 117).

[79] R. Bilger. "The Structure of Turbulent Nonpremixed Flames". *Symposium (International) on Combustion* 22 (1), 1989, pp. 475–488 (cited in p. 13).

[80] R. W. Bilger. "A Mixture Fraction Framework for the Theory and Modeling of Droplets and Sprays". *Combustion and Flame* 158 (2), 2011, pp. 191–202 (cited in p. 13).

[81] B. Franzelli, A. Vié, and M. Ihme. "On the Generalisation of the Mixture Fraction to a Monotonic Mixing-Describing Variable for the Flamelet Formulation of Spray Flames". *Combustion Theory and Modelling* 19 (6), 2015, pp. 773–806 (cited in p. 13).

[82] L. Gomet, V. Robin, and A. Mura. "A Multiple-Inlet Mixture Fraction Model for Nonpremixed Combustion". *Combustion and Flame* 162 (3), 2015, pp. 668–687 (cited in p. 14).

[83] D. L. Pintor. "Theoretical and Experimental Study on the Autoignition Phenomena of Homogeneous Reactive Mixtures". PhD thesis. Valencia: Universitat Politècnica de València, 2017 (cited in pp. 14, 15).

[84] X.-C. Lü, W. Chen, and Z. Huang. "A Fundamental Study on the Control of the HCCI Combustion and Emissions by Fuel Design Concept Combined with Controllable EGR. Part 1. The Basic Characteristics of HCCI Combustion". *Fuel* 84 (9), 2005, pp. 1074–1083 (cited in p. 15).

[85] K. Kumar, G. Mittal, and C.-J. Sung. "Autoignition of N-Decane under Elevated Pressure and Low-to-Intermediate Temperature Conditions". *Combustion and Flame* 156 (6), 2009, pp. 1278–1288 (cited in p. 15).

[86] B. Higgins, D. L. Siebers, and A. Aradi. "Diesel-Spray Ignition and Premixed-Burn Behavior". In: *SAE Technical Paper*. 2000 (cited in p. 15).

[87] C. Westbrook, H. Curran, W. Pitz, J. Griffiths, C. Mohamed, and S. Wo. "The Effects of Pressure, Temperature, and Concentration on the Reactivity of Alkanes: Experiments and Modeling in a Rapid Compression Machine". *Symposium (International) on Combustion* 27 (1), 1998, pp. 371–378 (cited in p. 16).

[88] R. N. Dahms, G. A. Paczko, S. A. Skeen, and L. M. Pickett. "Understanding the Ignition Mechanism of High-Pressure Spray Flames". *Proceedings of the Combustion Institute* 36 (2), 2017, pp. 2615–2623 (cited in pp. 16, 64, 71, 123).

[89] J. E. Dec. "A Conceptual Model of DI Diesel Combustion Based on Laser-Sheet Imaging". In: *SAE Technical Paper*. 1997 (cited in p. 16).

[90] E. J. Pérez Sánchez. "Application of a Flamelet-Based Combustion Model to Diesel-like Reacting Sprays". PhD thesis. Valencia: Universitat Politècnica de València, 2018 (cited in pp. 17, 39–41, 44).

[91] N. Maes. "The Life of a Spray". PhD thesis. Eindhoven: Technische Universiteit Eindhoven, 2019 (cited in pp. 17, 117, 123, 126).

[92] F. Tagliante-Saracino. "Combined Study by Direct Numerical Simulation and Optical Diagnostics of the Flame Stabilization in a Diesel Spray". PhD thesis. Paris: Université Paris-Saclay, 2019 (cited in p. 17).

[93] L. M. Pickett and D. L. Siebers. "Soot in Diesel Fuel Jets: Effects of Ambient Temperature, Ambient Density, and Injection Pressure". *Combustion and Flame* 138 (1-2), 2004, pp. 114–135 (cited in p. 17).

[94] L. M. Pickett, D. L. Siebers, and C. A. Idicheria. "Relationship Between Ignition Processes and the Lift-Off Length of Diesel Fuel Jets". In: *Powertrain & Fluid Systems Conference & Exhibition*. 2005 (cited in p. 17).

[95] L. M. Pickett, S. Kook, H. Persson, and Ö. Andersson. "Diesel Fuel Jet Lift-off Stabilization in the Presence of Laser-Induced Plasma Ignition". *Proceedings of the Combustion Institute* 32 (2), 2009, pp. 2793–2800 (cited in p. 17).

[96] Bockhorn. *Soot Formation in Combustion. Mechanisms and Models*. Vol. 59. Chemical Physics CHEMICAL. Berlin Heidelberg: Springer- Verlag, 1994 (cited in pp. 18, 19).

[97] D. Carbonell Sánchez. "Numerical Studies of Diffusion Flames. Special Emphasis on Flamelet Concept and Soot Formation". PhD thesis. Terrassa: Universitat Politècnica de Catalunya, 2008 (cited in pp. 18, 49, 50).

[98] C. Marchal. "Modelisation de La Formation et de l'oxydation Des Suies Dans Un Moteur Automobile". PhD thesis. Orléans: Université d'Orléans, 2008 (cited in pp. 18, 21, 23).

[99] I. Glassman and R. A. Yetter. "Chapter 8 - Environmental Combustion Considerations". In: *Combustion (Fourth Edition)*. Ed. by I. Glassman and R. A. Yetter. Fourth Edition. Burlington: Academic Press, 2008, pp. 409–494 (cited in pp. 18, 21).

[100] I. Sarkar, R. Raman, K. Jayanth, A. Jain, and K. C. Vora. "Characterization of Soot Microstructure for Diesel and Biodiesel Using Diesel Particulate Filter". In: *Innovative Design, Analysis and Development Practices in Aerospace and Automotive Engineering (I-DAD 2018)*. Ed. by U. Chandrasekhar, L.-J. Yang, and S. Gowthaman. Singapore: Springer Singapore, 2019, pp. 153–161 (cited in p. 18).

[101] V. Sharma, D. Uy, A. Gangopadhyay, A. O'Neill, et al. "Structure and Chemistry of Crankcase and Exhaust Soot Extracted from Diesel Engines". *Carbon* 103, 2016, pp. 327–338 (cited in p. 18).

[102] J. Olfert and S. Rogak. "Universal Relations between Soot Effective Density and Primary Particle Size for Common Combustion Sources". *Aerosol Science and Technology* 53 (5), 2019, pp. 485–492 (cited in pp. 18, 19).

[103] X. Wang, Y. Wang, Y. Bai, P. Wang, and Y. Zhao. "An Overview of Physical and Chemical Features of Diesel Exhaust Particles". *Journal of the Energy Institute*, 2018 (cited in p. 18).

[104] D. Aubagnac-Karkar. "Sectional Soot Modeling for Diesel RANS Simulations". PhD thesis. Châtenay-Malabry: École Centrale Paris, 2014 (cited in pp. 19, 35).

[105] J. D. Bittner and J. B. Howard. "Pre-Particle Chemistry in Soot Formation". In: *Particulate Carbon: Formation during Combustion*. Ed. by D. C. Siegla and G. W. Smith. Boston, MA: Springer US, 1981, pp. 109–142 (cited in p. 20).

[106] M. Frenklach, D. W. Clary, W. C. Gardiner, and S. E. Stein. "Detailed Kinetic Modeling of Soot Formation in Shock-Tube Pyrolysis of Acetylene". *Symposium (International) on Combustion* 20 (1), 1985. Twentieth Symposium (International) on Combustion, pp. 887–901 (cited in p. 20).

[107] M. Frenklach and H. Wang. "Detailed Modeling of Soot Particle Nucleation and Growth". *Symposium (International) on Combustion* 23 (1), 1991, pp. 1559–1566 (cited in pp. 20–22, 33).

[108] M. Frenklach. "Reaction Mechanism of Soot Formation in Flames". *Physical Chemistry Chemical Physics* 4 (11), 2002, pp. 2028–2037 (cited in pp. 20, 22).

[109] H. Wang. "Formation of Nascent Soot and Other Condensed-Phase Materials in Flames". *Proceedings of the Combustion Institute* 33 (1), 2011, pp. 41–67 (cited in pp. 21, 22).

[110] Y. Wang and S. H. Chung. "Soot Formation in Laminar Counterflow Flames". *Progress in Energy and Combustion Science* 74, 2019, pp. 152–238 (cited in pp. 21, 22).

[111] A. Violi, A. F. Sarofim, and G. A. Voth. "KINETIC MONTE CARLO–MOLECULAR DYNAMICS APPROACH TO MODEL SOOT INCEPTION". *Combustion Science and Technology* 176 (5-6), 2004, pp. 991–1005 (cited in p. 21).

[112] A. D'Anna. "Combustion-Formed Nanoparticles". *Proceedings of the Combustion Institute* 32 (1), 2009, pp. 593–613 (cited in p. 21).

[113] C. A. Schuetz and M. Frenklach. "Nucleation of Soot: Molecular Dynamics Simulations of Pyrene Dimerization". *Proceedings of the Combustion Institute* 29 (2), 2002, pp. 2307–2314 (cited in p. 21).

[114] D. Aubagnac-Karkar, A. El Bakali, and P. Desgroux. "Soot Particles Inception and PAH Condensation Modelling Applied in a Soot Model Utilizing a Sectional Method". *Combustion and Flame* 189, 2018, pp. 190–206 (cited in pp. 21, 34).

[115] H. Wang, Y. Li, Z. Iqbal, Y. Wang, C. Ma, and M. Yao. "A Comparison Study on the Combustion and Sooting Characteristics of Base Engine Oil and N-Dodecane in Laminar Diffusion Flames". *Applied Thermal Engineering* 158, 2019, p. 113812 (cited in p. 21).

[116] T. Mitra, T. Zhang, A. D. Sediako, and M. J. Thomson. "Understanding the Formation and Growth of Polycyclic Aromatic Hydrocarbons (PAHs) and Young Soot from n-Dodecane in a Sooting Laminar Coflow Diffusion Flame". *Combustion and Flame* 202, 2019, pp. 33–42 (cited in p. 21).

[117] K. Siegmann, K. Sattler, and H. Siegmann. "Clustering at High Temperatures: Carbon Formation in Combustion". *Journal of Electron Spectroscopy and Related Phenomena* 126 (1-3), 2002, pp. 191–202 (cited in p. 21).

[118] N. Eaves, S. Dworkin, and M. Thomson. "The Importance of Reversibility in Modeling Soot Nucleation and Condensation Processes". *Proceedings of the Combustion Institute* 35 (2), 2015, pp. 1787–1794 (cited in p. 21).

[119] A. Veshkini, N. A. Eaves, S. B. Dworkin, and M. J. Thomson. "Application of PAH-Condensation Reversibility in Modeling Soot Growth in Laminar Premixed and Nonpremixed Flames". *Combustion and Flame* 167, 2016, pp. 335–352 (cited in p. 21).

[120] N. A. Eaves, S. B. Dworkin, and M. J. Thomson. "Assessing Relative Contributions of PAHs to Soot Mass by Reversible Heterogeneous Nucleation and Condensation". *Proceedings of the Combustion Institute* 36 (1), 2017, pp. 935–945 (cited in p. 21).

[121] B. Haynes and H. Wagner. "Soot Formation". *Progress in Energy and Combustion Science* 7 (4), 1981, pp. 229–273 (cited in p. 22).

[122] H. Calcote. "Mechanisms of Soot Nucleation in Flames—A Critical Review". *Combustion and Flame* 42, 1981, pp. 215–242 (cited in p. 22).

[123] S. J. Harris and A. M. Weiner. "Surface Growth of Soot Particles in Premixed Ethylene/Air Flames". *Combustion Science and Technology* 31 (3-4), 1983, pp. 155–167 (cited in p. 22).

[124] P. Sunderland and G. Faeth. "Soot Formation in Hydrocarbon/Air Laminar Jet Diffusion Flames". *Combustion and Flame* 105 (1), 1996, pp. 132–146 (cited in p. 22).

[125] M. Frenklach and K. E. Spear. "Growth Mechanism of Vapor-Deposited Diamond". *Journal of Materials Research* 3 (1), 1988, pp. 133–140 (cited in p. 22).

[126] S. J. HARRIS and ANITA M. WEINER. "Determination of the Rate Constant for Soot Surface Growth". *Combustion Science and Technology* 32 (5-6), 1983, pp. 267–275. eprint: https://doi.org/10.1080/00102208308923661 (cited in p. 22).

[127] K. Homann and H. Wagner. "Some New Aspects of the Mechanism of Carbon Formation in Premixed Flames". *Symposium (International) on Combustion* 11 (1), 1967, pp. 371–379 (cited in p. 22).

[128] I. M. Kennedy. "The Evolution of a Soot Aerosol in a Counterflow Diffusion Flame". *Combustion and Flame* 68 (1), 1987, pp. 1–16 (cited in p. 22).

[129] S. J. Harris, A. M. Weiner, and C. C. Ashcraft. "Soot Particle Inception Kinetics in a Premixed Ethylene Flame". *Combustion and Flame* 64 (1), 1986, pp. 65–81 (cited in pp. 22, 24).

[130] F. Mauss, B. Trilken, H. Breitbach, and N. Peters. "Soot Formation in Partially Premixed Diffusion Flames at Atmospheric Pressure". en. In: *Soot Formation in Combustion: Mechanisms and Models*. Ed. by H. Bockhorn. Springer Series in Chemical Physics. Berlin, Heidelberg: Springer Berlin Heidelberg, 1994, pp. 325–349 (cited in p. 22).

[131] A. Cavaliere, R. Barbella, A. Ciajolo, A. D'anna, and R. Ragucci. "Fuel and Soot Oxidation in Diesel-like Conditions". *Symposium (International) on Combustion* 25 (1), 1994. Twenty-Fifth Symposium (International) on Combustion, pp. 167–174 (cited in p. 23).

[132] B. Stanmore, J. Brilhac, and P. Gilot. "The Oxidation of Soot: A Review of Experiments, Mechanisms and Models". *Carbon* 39 (15), 2001, pp. 2247–2268 (cited in p. 23).

[133] M. Frenklach, Z. Liu, R. I. Singh, G. R. Galimova, V. N. Azyazov, and A. M. Mebel. "Detailed, Sterically-Resolved Modeling of Soot Oxidation: Role of O Atoms, Interplay with Particle Nanostructure, and Emergence of Inner Particle Burning". *Combustion and Flame* 188, 2018, pp. 284–306 (cited in pp. 23, 48).

[134] I. M. Kennedy. "Models of Soot Formation and Oxidation". *Progress in Energy and Combustion Science* 23 (2), 1997, pp. 95–132 (cited in p. 23).

[135] H. Calcote and D. Manos. "Effect of Molecular Structure on Incipient Soot Formation". *Combustion and Flame* 49 (1), 1983, pp. 289–304 (cited in p. 24).

[136] D. Olson, J. Pickens, and R. Gill. "The Effects of Molecular Structure on Soot Formation II. Diffusion Flames". *Combustion and Flame* 62 (1), 1985, pp. 43–60 (cited in p. 24).

[137] A. Mensch, R. J. Santoro, T. A. Litzinger, and S.-Y. Lee. "Sooting Characteristics of Surrogates for Jet Fuels". *Combustion and Flame* 157 (6), 2010, pp. 1097–1105 (cited in p. 24).

[138] P. H. Joo, Y. Wang, A. Raj, and S. H. Chung. "Sooting Limit in Counterflow Diffusion Flames of Ethylene/Propane Fuels and Implication to Threshold Soot Index". *Proceedings of the Combustion Institute* 34 (1), 2013, pp. 1803–1809 (cited in p. 24).

[139] A. Llamas, M. Lapuerta, A.-M. Al-Lal, and L. Canoira. "Oxygen Extended Sooting Index of FAME Blends with Aviation Kerosene". *Energy & Fuels* 27 (11), 2013, pp. 6815–6822 (cited in p. 24).

[140] F. TAKAHASHI and I. GLASSMAN. "Sooting Correlations for Premixed Flames". *Combustion Science and Technology* 37 (1-2), 1984, pp. 1–19. eprint: https://doi.org/10.1080/00102208408923743 (cited in p. 24).

[141] I. Khan, G. Greeves, and D. Probert. "Air Pollution Control in Transport Engines". *Institution of Mechanical Engineers* 205, 1971 (cited in p. 24).

[142] P. S. Mehta and S. Das. "A Correlation for Soot Concentration in Diesel Exhaust Based on Fuel-Air Mixing Parameters". *Fuel* 71 (6), 1992, pp. 689–692 (cited in p. 24).

[143] H. HIROYASU, T. KADOTA, and M. ARAI. "Development and Use of a Spray Combustion Modeling to Predict Diesel Engine Efficiency and Pollutant Emissions : Part 1 Combustion Modeling". *Bulletin of JSME* 26 (214), 1983, pp. 569–575 (cited in p. 24).

[144] K. Nishida and H. Hiroyasu. "Simplified Three-Dimensional Modeling of Mixture Formation and Combustion in a D.I. Diesel Engine". *SAE Transactions* 98, 1989, pp. 276–293 (cited in p. 25).

[145] P. Belardini, C. Bertoli, A. Ciajolo, A. D'Anna, and N. Del Giacomo. "Three Dimensional Calculations of DI Diesel Engine Combustion and Comparison Whit In Cylinder Sampling Valve Data". In: *International Fuels & Lubricants Meeting & Exposition*. 1992 (cited in p. 25).

[146] H. Ogawa, Y. Matsui, S. Kimura, and J. Kawashima. "Three-Dimensional Computation of the Effects of the Swirl Ratio in Direct-Injection Diesel Engines on NOx and Soot Emissions". In: *International Fuels & Lubricants Meeting & Exposition*. 1996 (cited in p. 25).

[147] J. Nagle and R. F. Strickland-Constable. "Oxidation of Carbon between 1000-2000°C". In: *Proceedings of the Fifth Carbon Conference*. Vol. 1. London: Pergamon Press, 1962, p. 154 (cited in pp. 25, 29, 30).

[148] M. A. Patterson, S.-C. Kong, G. J. Hampson, and R. D. Reitz. "Modeling the Effects of Fuel Injection Characteristics on Diesel Engine Soot and NOx Emissions". In: *International Congress & Exposition*. 1994 (cited in p. 26).

[149] G. J. Micklow and W. Gong. "A Multistage Combustion Model and Soot Formation Model for Direct-Injection Diesel Engines". *Proceedings of the Institution of Mechanical Engineers, Part D: Journal of Automobile Engineering* 216 (6), 2002, pp. 495–504 (cited in p. 26).

[150] A. B. Dempsey, P. Seiler, K. Svensson, and Y. Qi. "A Comprehensive Evaluation of Diesel Engine CFD Modeling Predictions Using a Semi-Empirical Soot Model over a Broad Range of Combustion Systems". *SAE International Journal of Engines* 11 (6), 2018 (cited in p. 26).

[151] A. A. Moiz, M. M. Ameen, S.-Y. Lee, and S. Som. "Study of Soot Production for Double Injections of N-Dodecane in CI Engine-like Conditions". *Combustion and Flame* 173, 2016, pp. 123–131 (cited in p. 26).

[152] C. W. Lautenberger, J. L. de Ris, N. A. Dembsey, J. R. Barnett, and H. R. Baum. "A Simplified Model for Soot Formation and Oxidation in CFD Simulation of Non-Premixed Hydrocarbon Flames". *Fire Safety Journal* 40 (2), 2005, pp. 141–176 (cited in p. 26).

[153] O. Kaario, E. Antila, and M. Larmi. "Applying Soot Phi-T Maps for Engineering CFD Applications in Diesel Engines". In: *Powertrain & Fluid Systems Conference & Exhibition*. 2005 (cited in p. 26).

[154] M. Grill, M. Bargende, D. Rether, and A. Schmid. "Quasi-Dimensional and Empirical Modeling of Compression-Ignition Engine Combustion and Emissions". In: *SAE 2010 World Congress & Exhibition*. 2010 (cited in p. 26).

[155] P. Tesner, T. Smegiriova, and V. Knorre. "Kinetics of Dispersed Carbon Formation". *Combustion and Flame* 17 (2), 1971, pp. 253–260 (cited in p. 27).

[156] J. Moss, C. Stewart, and K. Syed. "Flowfield Modelling of Soot Formation at Elevated Pressure". *Symposium (International) on Combustion* 22 (1), 1989, pp. 413–423 (cited in pp. 27, 33).

[157] J. Moss, C. Stewart, and K. Young. "Modeling Soot Formation and Burnout in a High Temperature Laminar Diffusion Flame Burning under Oxygen-Enriched Conditions". *Combustion and Flame* 101 (4), 1995, pp. 491–500 (cited in p. 27).

[158] K. Leung, R. Lindstedt, and W. Jones. "A Simplified Reaction Mechanism for Soot Formation in Nonpremixed Flames". *Combustion and Flame* 87 (3), 1991, pp. 289–305 (cited in pp. 27–30).

[159] K. Lee, M. Thring, and J. Beér. "On the Rate of Combustion of Soot in a Laminar Soot Flame". *Combustion and Flame* 6, 1962, pp. 137–145 (cited in pp. 28–30).

[160] A. Kronenburg, R. Bilger, and J. Kent. "Modeling Soot Formation in Turbulent Methane–Air Jet Diffusion Flames". *Combustion and Flame* 121 (1-2), 2000, pp. 24–40 (cited in p. 30).

[161] D. Bradley, G. Dixon-Lewis, S. E.-d. Habik, and E. Mushi. "The Oxidation of Graphite Powder in Flame Reaction Zones". *Symposium (International) on Combustion* 20 (1), 1985. Twentieth Symposium (International) on Combustion, pp. 931–940 (cited in pp. 29, 30).

[162] F. Liu, H. Guo, G. Smallwood, and o. Gulder. "Numerical Modelling of Soot Formation and Oxidation in Laminar Coflow Non-Smoking and Smoking Ethylene Diffusion Flames". *Combustion Theory and Modelling* 7 (2), 2003, pp. 301–315 (cited in p. 30).

[163] C. P. Fenimore and G. W. Jones. "Oxidation of Soot by Hydroxyl Radicals". *The Journal of physical chemistry* 71 (3), 1967, pp. 593–597 (cited in pp. 29–32, 48).

[164] H. Guo, F. Liu, and G. J. Smallwood. "Soot and NO Formation in Counterflow Ethylene/Oxygen/Nitrogen Diffusion Flames". *Combustion Theory and Modelling* 8 (3), 2004, pp. 475–489 (cited in pp. 30, 48).

[165] K. G. Neoh, J. B. Howard, and A. F. Sarofim. "Soot Oxidation in Flames". In: *Particulate Carbon: Formation During Combustion*. Ed. by D. C. Siegla and G. W. Smith. Boston, MA: Springer US, 1981, pp. 261–282 (cited in pp. 29, 30).

[166] H. Watanabe, R. Kurose, S. Komori, and H. Pitsch. "Effects of Radiation on Spray Flame Characteristics and Soot Formation". *Combustion and Flame* 152 (1-2), 2008, pp. 2–13 (cited in p. 30).

[167] D. Carbonell, A. Oliva, and C. Perez-Segarra. "Implementation of Two-Equation Soot Flamelet Models for Laminar Diffusion Flames". *Combustion and Flame* 156 (3), 2009, pp. 621–632 (cited in p. 30).

[168] G. Vishwanathan and R. D. Reitz. "Development of a Practical Soot Modeling Approach and Its Application to Low-Temperature Diesel Combustion". *Combustion Science and Technology* 182 (8), 2010, pp. 1050–1082 (cited in pp. 29–31, 33, 91).

[169] L.-H. Dorey, N. Bertier, L. Tessé, and F. Dupoirieux. "Soot and Radiation Modeling in Laminar Ethylene Flames with Tabulated Detailed Chemistry". *Comptes Rendus Mécanique* 339 (12), 2011, pp. 756–769 (cited in pp. 29, 30, 44).

[170] M. Bolla, D. Farrace, Y. M. Wright, K. Boulouchos, and E. Mastorakos. "Influence of Turbulence–Chemistry Interaction for n-Heptane Spray Combustion under Diesel Engine Conditions with Emphasis on Soot Formation and Oxidation". *Combustion Theory and Modelling* 18 (2), 2014, pp. 330–360 (cited in p. 30).

[171] T. Kim and Y. Kim. "Interactive Transient Flamelet Modeling for Soot Formation and Oxidation Processes in Laminar Non-Premixed Jet Flames". *Combustion and Flame* 162 (5), 2015, pp. 1660–1678 (cited in p. 30).

[172] K. M. Pang, M. Jangi, X.-S. Bai, and J. Schramm. "Evaluation and Optimisation of Phenomenological Multi-Step Soot Model for Spray Combustion under Diesel Engine-like Operating Conditions". *Combustion Theory and Modelling* 19 (3), 2015, pp. 279–308 (cited in p. 30).

[173] L. Zimmer, F. M. Pereira, J. A. van Oijen, and L. P. H. de Goey. "Investigation of Mass and Energy Coupling between Soot Particles and Gas Species in Modelling Ethylene Counterflow Diffusion Flames". *Combustion Theory and Modelling* 21 (2), 2016, pp. 358–379 (cited in pp. 29, 30).

[174] H. Yigit Akargun, B. Akkurt, N. G. Deen, and L. Somers. "Extending the Flamelet Generated Manifold for Soot and NOx Modeling in Diesel Spray Combustion". *The Proceedings of the International symposium on diagnostics and modeling of combustion in internal combustion engines* 2017.9 (0), 2017, A105 (cited in p. 30).

[175] S. S. Pandurangi, M. Bolla, Y. M. Wright, K. Boulouchos, et al. "Onset and Progression of Soot in High-Pressure n-Dodecane Sprays under Diesel Engine Conditions". *International Journal of Engine Research* 18 (5-6), 2017, pp. 436–452 (cited in p. 30).

[176] S. F. Fernandez, C. Paul, A. Sircar, A. Imren, et al. "Soot and Spectral Radiation Modeling for High-Pressure Turbulent Spray Flames". *Combustion and Flame* 190, 2018, pp. 402–415 (cited in p. 30).

[177] M. A. Chishty, M. Bolla, E. R. Hawkes, Y. Pei, and S. Kook. "Soot Formation Modelling for N-Dodecane Sprays Using the Transported PDF Model". *Combustion and Flame* 192, 2018, pp. 101–119 (cited in p. 30).

[178] N. Ladommatos, H. Song, and H. Zhao. "Measurements and Predictions of Diesel Soot Oxidation Rates". *Proceedings of the Institution of Mechanical Engineers, Part D: Journal of Automobile Engineering* 216 (8), 2002, pp. 677–689 (cited in p. 31).

[179] F. Tao, S. Srinivas, R. D. Reitz, and D. E. Foster. "Comparison of Three Soot Models Applied to Multi-Dimensional Diesel Combustion Simulations". *JSME International Journal Series B* 48 (4), 2005, pp. 671–678 (cited in p. 32).

[180] G. Vishwanathan and R. D. Reitz. "Numerical Predictions of Diesel Flame Lift-off Length and Soot Distributions under Low Temperature Combustion Conditions". In: *SAE World Congress & Exhibition*. 2008 (cited in p. 32).

[181] S. A. Skeen, J. Manin, L. M. Pickett, E. Cenker, et al. "A Progress Review on Soot Experiments and Modeling in the Engine Combustion Network (ECN)". *SAE International Journal of Engines* 9 (2), 2016, pp. 883–898 (cited in p. 33).

[182] M. Frenklach and S. J. Harris. "Aerosol Dynamics Modeling Using the Method of Moments". *Journal of Colloid and Interface Science* 118 (1), 1987, pp. 252–261 (cited in p. 33).

[183] Y. Xuan and G. Blanquart. "Effects of Aromatic Chemistry-Turbulence Interactions on Soot Formation in a Turbulent Non-Premixed Flame". *Proceedings of the Combustion Institute* 35 (2), 2015, pp. 1911–1919 (cited in p. 34).

[184] A. Attili, F. Bisetti, M. E. Mueller, and H. Pitsch. "Damköhler Number Effects on Soot Formation and Growth in Turbulent Nonpremixed Flames". *Proceedings of the Combustion Institute* 35 (2), 2015, pp. 1215–1223 (cited in p. 34).

[185] M. Balthasar and M. Frenklach. "Detailed Kinetic Modeling of Soot Aggregate Formation in Laminar Premixed Flames". *Combustion and Flame* 140 (1-2), 2005, pp. 130–145 (cited in p. 34).

[186] F. Bisetti, G. Blanquart, M. E. Mueller, and H. Pitsch. "On the Formation and Early Evolution of Soot in Turbulent Nonpremixed Flames". *Combustion and Flame* 159 (1), 2012, pp. 317–335 (cited in p. 34).

[187] R. Mehta, D. Haworth, and M. Modest. "An Assessment of Gas-Phase Reaction Mechanisms and Soot Models for Laminar Atmospheric-Pressure Ethylene–Air Flames". *Proceedings of the Combustion Institute* 32 (1), 2009, pp. 1327–1334 (cited in p. 34).

[188] P. Donde, V. Raman, M. E. Mueller, and H. Pitsch. "LES/PDF Based Modeling of Soot–Turbulence Interactions in Turbulent Flames". *Proceedings of the Combustion Institute* 34 (1), 2013, pp. 1183–1192 (cited in p. 34).

[189] A. Hatzipanagiotou, P. Wenzel, C. Krueger, R. Payri, et al. "Soot Model Calibration Based on Laser Extinction Measurements". In: *SAE 2016 World Congress and Exhibition*. 2016 (cited in p. 34).

[190] P. Priesching, R. Tatschl, F. Mauss, F. Saric, et al. "Soot Particle Size Distribution~A Joint Work for Kinetic Modelling and Experimental Investigations". In: *7th International Conference on Engines for Automobile*. 2005 (cited in p. 34).

[191] S. Hong, M. Wooldridge, H. Im, D. Assanis, and H. Pitsch. "Development and Application of a Comprehensive Soot Model for 3D CFD Reacting Flow Studies in a Diesel Engine". *Combustion and Flame* 143 (1-2), 2005, pp. 11–26 (cited in p. 34).

[192] G. Nakov, F. Mauss, P. Wenzel, R. Steiner, et al. "Soot Simulation under Diesel Engine Conditions Using a Flamelet Approach". *SAE International Journal of Engines* 2 (2), 2009, pp. 89–104 (cited in p. 34).

[193] Á. L. Bodor. "Numerical Modeling of Soot Formation and Evolution in Laminar Flames with Detailed Kinetics". PhD thesis. Milano: Policecnico di Milano, 2019 (cited in pp. 34, 35).

[194] M. Sirignano, A. Ciajolo, A. D'Anna, and C. Russo. "Particle Formation in Premixed Ethylene-Benzene Flames: An Experimental and Modeling Study". *Combustion and Flame* 200, 2019, pp. 23–31 (cited in p. 34).

[195] A. L. Bodor, B. Franzelli, T. Faravelli, and A. Cuoci. "A Post Processing Technique to Predict Primary Particle Size of Sooting Flames Based on a Chemical Discrete Sectional Model: Application to Diluted Coflow Flames". *Combustion and Flame* 208, 2019, pp. 122–138 (cited in p. 34).

[196] W. Pejpichestakul, A. Frassoldati, A. Parente, and T. Faravelli. "Soot Modeling of Ethylene Counterflow Diffusion Flames". *Combustion Science and Technology* 191 (9), 2019, pp. 1473–1483 (cited in p. 34).

[197] F. Cepeda, A. Jerez, R. Demarco, F. Liu, and A. Fuentes. "Influence of Water-Vapor in Oxidizer Stream on the Sooting Behavior for Laminar Coflow Ethylene Diffusion Flames". *Combustion and Flame* 210, 2019, pp. 114–125 (cited in p. 34).

[198] C. A. Hoerlle and F. M. Pereira. "Effects of CO2 Addition on Soot Formation of Ethylene Non-Premixed Flames under Oxygen Enriched Atmospheres". *Combustion and Flame* 203, 2019, pp. 407–423 (cited in p. 34).

[199] P. Rodrigues, B. Franzelli, R. Vicquelin, O. Gicquel, and N. Darabiha. "Coupling an LES Approach and a Soot Sectional Model for the Study of Sooting Turbulent Non-Premixed Flames". *Combustion and Flame* 190, 2018, pp. 477–499 (cited in p. 34).

[200] S. Gkantonas, M. Sirignano, A. Giusti, A. D'Anna, and E. Mastorakos. "COMPREHENSIVE SOOT PARTICLE SIZE DISTRIBUTION MODELLING OF A MODEL RICH-QUENCH-LEAN BURNER". In: *11th Mediterranean Combustion Symposium*. Tenerife Spain, 2019 (cited in p. 34).

[201] D. Aubagnac-Karkar, J.-B. Michel, O. Colin, and N. Darabiha. "Combustion and Soot Modelling of a High-Pressure and High-Temperature Dodecane Spray". *International Journal of Engine Research* 19 (4), 2018, pp. 434–448 (cited in p. 34).

[202] D. Aubagnac-Karkar, J.-B. Michel, O. Colin, P. E. Vervisch-Kljakic, and N. Darabiha. "Sectional Soot Model Coupled to Tabulated Chemistry for Diesel RANS Simulations". *Combustion and Flame* 162 (8), 2015, pp. 3081–3099 (cited in p. 35).

[203] P. P. Duvvuri, S. Sukumaran, R. K. Shrivastava, and S. Sreedhara. "Modeling Soot Particle Size Distribution in Diesel Engines". *Fuel* 243, 2019, pp. 70–78 (cited in p. 35).

[204] F. Ibrahim, W. M. F. Wan Mahmood, S. Abdullah, and M. R. A. Mansor. "Comparison of Simple and Detailed Soot Models in the Study of Soot Formation in a Compression Ignition Diesel Engine". In: *WCX™ 17: SAE World Congress Experience*. 2017 (cited in p. 35).

[205] R. Payri, J. M. García-Oliver, M. Bardi, and J. Manin. "Fuel Temperature Influence on Diesel Sprays in Inert and Reacting Conditions". en. *Applied Thermal Engineering* 35, 2012, pp. 185–195 (cited in p. 37).

[206] J. V. Pastor, J. M. Garcia-Oliver, A. Garcia, and A. Morales López. "An Experimental Investigation on Spray Mixing and Combustion Characteristics for Spray C/D Nozzles in a Constant Pressure Vessel". In: *International Powertrains, Fuels & Lubricants Meeting*. 2018-01-1783. 2018 (cited in pp. 37, 79).

[207] J. M. García-Oliver, L.-M. Malbec, H. B. Toda, and G. Bruneaux. "A Study on the Interaction between Local Flow and Flame Structure for Mixing-Controlled Diesel Sprays". *Combustion and Flame* 179, 2017, pp. 157–171 (cited in pp. 38, 55, 74, 75).

[208] *CONVERGE CFD Software*. https://convergecfd.com (cited in p. 38).

[209] *CONVERGE Manual*. Tech. rep. Convergent Science, 2016 (cited in p. 39).

[210] S. B. POPE. "An Explanation of the Turbulent Round-Jet/Plane-Jet Anomaly". *AIAA Journal* 16 (3), 1978, pp. 279–281 (cited in p. 39).

[211] R. Novella, A. García, J. Pastor, and V. Domenech. "The Role of Detailed Chemical Kinetics on CFD Diesel Spray Ignition and Combustion Modelling". *Mathematical and Computer Modelling* 54 (7-8), 2011, pp. 1706–1719 (cited in p. 39).

[212] M. D. J. Chavez Cobo. "Modelado CFD Euleriano-Lagrangiano Del Chorro Diesel y Evaluación de Su Combinación Con Modelos Fenomenológicos y Unidimensionales". PhD thesis. Valencia: Universitat Politècnica de València, 2013 (cited in p. 39).

[213] P. K. Senecal, E. Pomraning, K. J. Richards, T. E. Briggs, et al. "Multi-Dimensional Modeling of Direct-Injection Diesel Spray Liquid Length and Flam Lift-off Length Using CFD an Parallel Detailed Chemistry". In: *SAE Technical Paper*. 2003, pp. 1331–1351 (cited in pp. 39, 40).

[214] J. F. Winklinger. "Implementation of a Combustion Model Based on the Flamelet Concept and Its Application to Turbulent Reactive Sprays". PhD thesis. Valencia: Universitat Politècnica de València, 2014 (cited in pp. 39, 41, 44).

[215] T. Yao, Y. Pei, B.-J. Zhong, S. Som, T. Lu, and K. H. Luo. "A Compact Skeletal Mechanism for n -Dodecane with Optimized Semi-Global Low-Temperature Chemistry for Diesel Engine Simulations". *Fuel* 191, 2017, pp. 339–349 (cited in pp. 39, 52).

[216] K. Narayanaswamy, P. Pepiot, and H. Pitsch. "A Chemical Mechanism for Low to High Temperature Oxidation of N-Dodecane as a Component of Transportation Fuel Surrogates". *Combustion and Flame* 161 (4), 2014, pp. 866–884 (cited in pp. 40, 52, 91).

[217] F. A. Williams. "Recent Advances in Theoretical Descriptions of Turbulent Diffusion Flames". In: *Turbulent Mixing in Nonreactive and Reactive Flows*. Ed. by S. N. B. Murthy. Boston, MA: Springer New York, 1975, pp. 189–208 (cited in p. 41).

[218] B. Naud, R. Novella, J. M. Pastor, and J. F. Winklinger. "RANS Modelling of a Lifted H 2 /N 2 Flame Using an Unsteady Flamelet Progress Variable Approach with Presumed PDF". *Combustion and Flame* 162 (4), 2015, pp. 893–906 (cited in pp. 42, 53).

[219] P. Kundu, M. M. Ameen, C. Xu, U. Unnikrishnan, T. Lu, and S. Som. "Implementation of Detailed Chemistry Mechanisms in Engine Simulations". *Journal of Engineering for Gas Turbines and Power* 141 (1), 2018 (cited in pp. 42, 53, 91).

[220] T. Poinsot and D. Veynante. *Theoretical and Numerical Combustion*. RT Edwards, Inc., 2005 (cited in p. 42).

[221] B. Fiorina, O. Gicquel, L. Vervisch, S. Carpentier, and N. Darabiha. "Approximating the Chemical Structure of Partially Premixed and Diffusion Counterflow Flames Using FPI Flamelet Tabulation". en. *Combustion and Flame* 140 (3), 2005, pp. 147–160 (cited in p. 44).

[222] J. M. Desantes, J. M. Garcia-Oliver, R. Novella, and L. Pachano. "A Numerical Study of the Effect of Nozzle Diameter on Diesel Combustion Ignition and Flame Stabilization". *International Journal of Engine Research* 21 (1), 2020, pp. 101–121 (cited in p. 53).

[223] J. Benajes, R. Payri, M. Bardi, and P. Martí-Aldaraví. "Experimental Characterization of Diesel Ignition and Lift-off Length Using a Single-Hole ECN Injector". en. *Applied Thermal Engineering* 58 (1-2), 2013, pp. 554–563 (cited in p. 56).

[224] R. Payri, J. M. García-Oliver, T. Xuan, and M. Bardi. "A Study on Diesel Spray Tip Penetration and Radial Expansion under Reacting Conditions". *Applied Thermal Engineering* 90, 2015, pp. 619–629 (cited in p. 58).

[225] H. Kahila, A. Wehrfritz, O. Kaario, M. Ghaderi Masouleh, et al. "Large-Eddy Simulation on the Influence of Injection Pressure in Reacting Spray A". *Combustion and Flame* 191, 2018, pp. 142–159 (cited in p. 64).

[226] K. M. Pang, M. Jangi, X.-S. Bai, J. Schramm, J. H. Walther, and P. Glarborg. "Effects of Ambient Pressure on Ignition and Flame Characteristics in Diesel Spray Combustion". *Fuel* 237, 2019, pp. 676–685 (cited in p. 69).

[227] F. Tagliante, T. Poinsot, L. M. Pickett, P. Pepiot, G. Bruneaux, and C. Angelberger. "A Conceptual Model of the Flame Stabilization Mechanisms for a Lifted Diesel-Type Flame Based on Direct Numerical Simulation and Experiments". *Combustion and Flame* 201, 2019, pp. 65–77 (cited in p. 79).

[228] J. M. Desantes, J. M. Garcia-Oliver, J. M. Pastor, and A. Pandal. "A Comparison of Diesel Sprays CFD Modeling Approaches: DDM versus Σ-Y Eulerian Atomization Model". *Atomization and Sprays* 26 (7), 2016, pp. 713–737 (cited in p. 85).

[229] P. K. Senecal, E. Pomraning, K. J. Richards, and S. Som. "Grid-Convergent Spray Models for Internal Combustion Engine CFD Simulations". In: *ICEF2012*. ASME 2012 Internal Combustion Engine Division Fall Technical Conference, 2012, pp. 697–710 (cited in p. 85).

[230] T. Lucchini, G. D'Errico, and D. Ettorre. "Numerical Investigation of the Spray–Mesh–Turbulence Interactions for High-Pressure, Evaporating Sprays at Engine Conditions". en. *International Journal of Heat and Fluid Flow* 32 (1), 2011, pp. 285–297 (cited in p. 85).

[231] K. Kuo. *Principles of Combustion*. New York: John Wiley & Sons, Inc, 1986 (cited in p. 87).

[232] C. Patel, C. Mounaïm-Rousselle, F. Foucher, C. Hespel, and B. Moreau. "Effect of Residual Gases on Soot Production of SPRAY A Conditions". In: *https://ecn.sandia.gov/workshop/ECN7/ECN6.8.mp4*. 2019 (cited in p. 109).

[233] B. W. Knox, C. L. Genzale, L. M. Pickett, J. M. Garcia-Oliver, and W. Vera-Tudela. "Combustion Recession after End of Injection in Diesel Sprays". *SAE International Journal of Engines* 8 (2), 2015, pp. 679–695 (cited in p. 123).

[234] M. P. B. Musculus and K. Kattke. "Entrainment Waves in Diesel Jets". *SAE International Journal of Engines* 2 (1), 2009, pp. 1170–1193 (cited in p. 123).

[235] S. Skeen, J. Manin, and L. M. Pickett. "Visualization of Ignition Processes in High-Pressure Sprays with Multiple Injections of n-Dodecane". *SAE International Journal of Engines* 8 (2), 2015, pp. 696–715 (cited in p. 123).

[236] T. Xuan, N. Maes, J. M. Garcia-Oliver, and Z. He. "Soot Characteristics of Diesel Sprays with Different Split-Injection Strategies". In: *38th International Symposium on Combustion*. 2021 (cited in p. 126).

UNIVERSITAT POLITÈCNICA DE VALÈNCIA

DOCTORAL THESIS

CFD MODELING OF COMBUSTION AND SOOT PRODUCTION IN DIESEL SPRAYS

PRESENTED BY:
Leonardo Manuel Pachano Prieto

April 2020
DEPARTAMENTO DE MÁQUINAS Y MOTORES TÉRMICOS